MODELING HARMONIC GENERATION FROM NANOSTRUCTURED SURFACES

JESSE THOMPSON

Thesis submitted to the University of Ottawa in partial fulfillment of
the requirements for the Master of Science degree in Physics

Ottawa-Carleton Institute of Physics
Department of Physics
Faculty of Science
University of Ottawa, Ottawa, Canada

Summary

In this thesis, I develop a novel time-domain approach for nonlinear scattering theory (NLST), a previously frequency domain method for estimating the nonlinear generation from a nanostructure. Due to a gap in literature, I then perform a full comparison of this novel time domain approach to the existing one in the frequency domain. Using the example scenario of third harmonic generation from various media in 1D and 3D, I compare – quantitatively – the NLST estimated nonlinear spectra to two types of direct nonlinear simulations: one using an experimental value for the nonlinear optical susceptibility, and, for plasmonic systems, another using a hydrodynamics model for the nonlinear plasmonic response. Through testing differing NLST approaches on these systems, I demonstrate the effectiveness of the novel time-domain NLST and assess the use cases for this method as well as the pre-existing ones. Lastly, I discuss the applicability of NLST in future works involving the inverse design process, and high-order harmonic generation.

Statement of Originality

I hereby certify that all work presented in this thesis is my own – excluding this sentence, of course, which likely has been given by a great deal many more than myself.

Preliminary scripts used for electrodynamic simulations in 1-dimension were developed by myself, along with all the necessary pre- and post-processing scripts used to calculate and visualize the results. I expanded these scripts to be made compatible with a pre-existing in-house electrodynamic solver that is a shared collaboration between our research group and one at the Leibniz Universität Hannover in Germany. Though this in-house solver, along with the nonlinear models being used for validation were developed by other members of these research groups, I have contributed to the software in a lead development role, while also performing necessary fixes and adding any additional required features for this thesis. The written content present in this thesis, from introductions to analysis, is original work that was written and compiled entirely my me, aside from much appreciated edits provided by my thesis supervisor, Dr. Lora Ramunno.

Acknowledgments

Without the help of others, this thesis would truly have never made it to anyone's desk. I would like to first thank Dr. Lora Ramunno for being an excellent thesis supervisor, with much patience for my ability to derail meetings with tangential chit-chat. She has provided me with great feedback and greatly facilitated my growth as a computational physicist. I would also like to thank our close collaborator, Dr. Antonio Cala Lesina for his help in learning the finite-difference time-domain method, understanding the in-house 3D-FDTD software (which he authored a great deal of), as well as making changes to it. I commend his ability to cope with my many outward thoughts and questions.

Here at the University of Ottawa, I have met a great deal of fellow researchers, both in my group, and outside, who have helped me settle into Ottawa and grow as a scientist in the midst of a global pandemic. Though there are too many to name directly, I cannot go without naming the man with many stories to keep one entertained, Daniel Trotter. Of course, I would like to thank my family and friends, that however often I fail to visit them, continue to encourage and support my studies while reminding me to take time to relax and have fun.

Most importantly, I would like to thank my partner Brandon, who despite knowing nothing of what I do, goes out of his way to provide me with any assistance he possibly can.

Contents

1 Introduction **1**

1.1 Nonlinear Nanophotonics 1

1.2 Motivations and Nonlinear Scattering Theory 4

2 Background Information **7**

2.1 Material Response 7

2.1.1 Perturbative Nonlinear Material Response 8

2.1.2 Instantaneous Material Response from Polychromatic Sources 9

2.1.3 A Hydrodynamic Response for Gold 11

2.2 Lorentz Reciprocity 12

2.2.1 Formulation in the Frequency Domain 13

2.2.2 Formulation in the Time Domain 15

3 Nonlinear Scattering Theory **19**

3.1 The Problem Setup for NLST 20

3.2 Extending NLST into the Time Domain 25

3.3 Numerical Recipes for NLST 28

3.3.1 Numerical Recipe for NLST in the Frequency Domain 28

3.3.2 Numerical Recipe for NLST in the Time Domain 29

3.4 Different Approaches for the Nonlinear Current 31

3.4.1 Frequency Method 31

3.4.2 Hybrid Method 32

3.4.3 Time Method 32

4 Results and Discussion **34**

4.1 1D FDTD for a Thin Film of Fused Silica 35

4.2 1D FDTD for a Thin Film of Gold 43

4.3 3D FDTD for a Thin Film of Gold 47

4.4 3D FDTD for a Nanosphere of Gold 54

5 Conclusions and Future Outlooks **62**

5.1 Effectiveness of the Novel Time Domain Approach 62

5.2 Limitations in Nonlinear Modeling 63

5.3 A Review of Use Cases and Viability for NLST 64

5.4 Future Extensions to High Harmonic Generation 66

5.4.1 Preliminary HHG Investigations 66

A Simulating Nonlinear Media Using FDTD Methods **68**

A.1 Base Update Equations 68

A.2 Simulating a Dispersionless Nonlinear Material 69

A.3 Simulating a Dispersive Nonlinear Material 70

B Far-Field Electric Field From a Sphere of Uniform Current **73**

References **76**

List of Figures

3.1 **The NLST Region** 20
3.2 **The Driving Field for NLST** 21
3.3 **The Nonlinear Generation Propagates Toward the Detector Field** . 21
3.4 **A Fictitious Current Source at the Detector** 23
3.5 **Plane Wave Approximation of the Fictitious Current Source** 23
4.1 **NLST Reflected Spectra – 25nm Silica Film and 25fs Pulse** 37
4.2 **NLST Transmitted Spectra – 25nm Silica Film and 25fs Pulse** . . . 37
4.3 **NLST Reflected Spectra – 355nm Silica Film and 25fs Pulse** 39
4.4 **NLST Transmitted Spectra – 355nm Silica Film and 25fs Pulse** . . 39
4.5 **NLST Reflected Spectra – 25nm Silica Film and 100fs Pulse** 40
4.6 **Noise-Corrected Frequency Method NLST Reflected Spectra – 25nm Silica Film and 100fs Pulse** 41
4.7 **NLST Reflected Spectra – 25nm Silica Film and 100fs Pulse** 42
4.8 **NLST Transmitted Spectra – 25nm Silica Film and 100fs Pulse** . . 42
4.9 **NLST Reflected Spectra – 50nm Gold Film and 25fs Pulse** 45
4.10 **NLST Transmitted Spectra – 50nm Gold Film and 25fs Pulse** . . . 45
4.11 **NLST Transmitted Spectra – 355nm Gold Film and 25fs Pulse** . . . 46
4.12 **NLST Reflected Spectra – 50nm Gold Film and 100fs Pulse** 48
4.13 **NLST Transmitted Spectra – 50nm Gold Film and 100fs Pulse** . . . 48
4.14 **NLST Reflected Spectra – 50nm Gold Film and 25fs Pulse** 50
4.15 **NLST Reflected Spectra – 50nm Gold Film and 100fs Pulse** 52
4.16 **NLST Reflected Spectra – 355nm Gold Film and 100fs Pulse** 53
4.17 **NLST Transmitted Spectra – 25nm Radius Gold Nanosphere and 25fs Pulse** 55
4.18 **Tensor and Hydrodynamic Third Harmonic Field Profiles for 25fs Pulse Incident Gold** 56
4.19 **High-Resolution Hydrodynamic Third Harmonic Field Profiles for 25fs Pulse Incident on a Gold Sphere with 25nm Radius** 57
4.20 **NLST Transmitted Spectra From a 25nm Radius Gold Nanosphere Illuminated by a 100fs Pulse** 58
4.21 **NLST Transmitted Spectra From a 50nm Radius Gold Nanosphere Illuminated by a 25fs Pulse** 60
4.22 **Tensor and Hydrodynamic Third Harmonic Cross-Section for 25fs Pulse Incident Gold Nanosphere of 50nm Radius** 60

5.1 **Reflected HHG from a Thin Film of ZnO** 67

List of Tables

4.1 **1D FDTD Simulation and Material Parameters for THG in a Thin Silica Film** 36
4.2 **1D FDTD Simulation and Material Parameters for THG in a Thin Gold Film** 44
4.3 **3D FDTD Simulation and Material Parameters for THG in a Thin Gold Film** 49
4.4 **3D FDTD Simulation and Material Parameters for THG in a Gold Nanosphere** 55

Chapter 1

Introduction

1.1 Nonlinear Nanophotonics

The essence of nonlinear nanophotonics can be summarized into one clear and concise statement: interesting phenomena occurs when high intensity light interacts with objects sub-wavelength in size. The two key ingredients outlined in this statement are that of "high intensity light", which provides the "nonlinear", and "sub-wavelength structures", which provides the "nanophotonics". Though each of these are vast fields of their own, their intersection is truly a groundbreaking regime.

At its core, the idea of sub-wavelength objects affecting the light that passes by and through it is not new in the field of physics. Artificially, these effects have been observed for over a millennia. A famous example of this would be the Lycurgus cup – a Roman chalice that has been dated to be approximately 1600 years old – which can change colour depending on whether it is illuminated from the inside or outside, due to the Romans doping the glass with round silver and gold nanoparticles as small as 50 nanometers[1]. If one chooses to expand beyond the limitation of artificial origins, it does not require looking far to see these effects in nature. For millions of years, the effect of nanostructuring has been demonstrated in nature, in particular by insects, who are internationally known for exhibiting fascinating optical effects such as butterflies with "ultra-black" wings[2], scarab beetles with glossy white bodies[3], or the interesting coloring and optical effects of a peacock's feathers[4], all of which are due to orderly and disorderly structuring present on the nanoscale.

The physical study of artificial nanostructures began in the year 1785[5]. In the first publication by David Rittenhouse[6], the motivations were noted to be due to a letter received from the author and poet Francis Hopkinson, where he noted observations of what he believed to be a magnifying effect on the silk threads of his handkerchief when he held it up to a lamp post in the distance. David Rittenhouse believed the observation to instead be something much deeper, exploring it in detail. He published the first paper on the topic, which clearly

outlines the creation of the first diffraction grating using nails and hairs[6], and documents the observation of diffracted light from a candle, clearly noting the angles and prismatic-like separation of colours. This publication clearly marks the beginning to a field that over time has grown immensely.

In more recent times, advancements in nanofabrication technology has fueled a great deal of research in artificial structuring, leading to excited growth in research on metamaterials[7] and metasurfaces[8, 9]. Each are composed of their building blocks, the meta-atom[10], that are arranged in 2-dimensional and 3-dimensional arrays to produce specific individual and ensemble effects [11]. Metasurfaces and metamaterials are each artificial variations on their naturally occurring counterparts that have been engineered to display specific functional properties, one such example being a negative permittivity [12, 13].

In the linear regime, meta-surfaces exist in varying forms and are used in a plethora of optical projects as they provide unprecedented control over phase, amplitude, and polarization, all while being effectively 2- dimensional[14, 15]. With the ability to tailor the properties of media in varying dimensionalities, there have been several realized applications in compact optics including imaging using metalenses[16, 17], spectroscopy[18], beam shaping[19], polarization splitting[20], and holography[21, 22, 15], to name a few. Given their immense usability and flexibility, it was only a matter of time before their applications in the field of nonlinear optics would be explored as well.

The field of nonlinear optics, as previously mentioned, relates directly to the involvement of "high energy light". This dependence makes its emergence in the history of physical studies to be much more recent in comparison to sub-wavelength physics in the late 1700s. Nonlinear effects are inherently weaker than linear effects, making them highly dependent on the intensity of the stimulating field to observe[23]. For this reason, they were not able to be studied until a high enough intensity (and low enough noise floor) could be achieved – a feat not attained until the invention of lasers in 1960[24]. The first nonlinear effects to be studied were that of second harmonic generation, discovered and published in 1961 by Franken et al. [25]. The publication even begins by directly attributing the ability to prove such an effect to the then newly invented ruby lasers.

Being discovered soon after each other, many of these lower orders of nonlinear optical phenomena have been studied nearly as long as lasers themselves. For example, we look to harmonic generation, which is a form of sum-frequency generation. In this nonlinear optical process, the response of nonlinear media to high intensity light at a fundamental frequency causes the material to partially up-convert the photon energy given to it via the source to a higher energy photons at harmonics (i.e. integer multiples of the pump frequency)[23]. This nonlinear optical process has established itself in both microscopy[26, 27, 28], and

spectroscopy[29, 30]. Many of these current applications branch into biomedical sensing and diagnosis, utilising the non-centrosymmetric structure of collagen to detect diseases like cancer and fibrosis[31].

A few decades ago, high harmonic generation (HHG) was observed[32], where photons several factors higher in energy are produced via a non-perturbative nonlinear optical process (i.e. "extreme" nonlinear optics), unlike perturbative low-order harmonic generation described above. Within a decade of its discovery, the order of the harmonics observed had tripled from the 11th up to the 33rd[33], and a strong interest in HHG was rapidly growing as a table-top source of short pulses covering broad spectral ranges, stretching into the extreme ultra-violet (XUV)[34] and reaching down into attosecond time scales. Serving as a foundation for the field of attosecond science[35, 36, 37] these pulses have countless applications, such as probing and imaging molecules [38, 39] and ultra-high resolution imaging far below the diffraction limit of visible light[40]. Many original investigations use HHG created from intense irradiation of gases. More recently, however, HHG was observed from intense irradiation of solids[41, 37], which offers many promises over their gaseous alternative, including a promise of achieving higher conversion efficiencies, an issue that critically affects both the gas and solid state HHG[42].

At the intersection of sub-wavelength and nonlinear optics lies the field of nonlinear nanophotonics, which studies the nonlinear optical processes that can occur alongside subwavelength structures both directly, or through enhancements. Alongside these increased efficiencies through enhancements, the subwavelength structures further give vectorial control over the phase and amplitude of the light[43]. Continuing the focus on harmonic generation, we see complexities in the conventional bulk approach that persist to the present day despite years of advancements. For example, there is complexity in the phase-matching requirement to nonlinear generation in bulk media often requiring the use of birefringent or periodically poled crystals to obtain suitable quantities of nonlinear generation without incurring damages[23].

With the current focus on compact optical elements for functionalities being integrated into chip design, there is increasing attention being paid to the relationship between metamaterials, metasurfaces, and the nonlinear optics that play a critical role in the implementations[44]. This moves the focus of recent works in nonlinear nanophotonics on each of these nanostructures and how their precise features can be engineered to address known problems and difficulties in conventional bulk nonlinear optics[45]. As the nonlinear setup becomes more compact and subwavelength in size, there are some issues which are present in the bulk approach that are directly combated, for example, notably relaxed phase matching conditions[45]. However, with a smaller amount of nonlinear media

present for the light to travel through, there can be a decreased yield[45]. Ultimately, this leads to the use of nanostructured surfaces and metamaterials that exhibit enhanced nonlinearities, allowing them to yield greater amounts of harmonic generation more efficiently. Strong nonlinear enhancements have been demonstrated in many works using various types of structuring using both metallic/plasmonic[46, 47, 48, 49, 5, 50, 45], and all-dielectric materials[5, 51, 45]. Recently, metasurfaces for enhancing high harmonic generation have also been demonstrated[52, 14].

The number of possible designs for any metasurface, including nonlinear ones, is seemingly infinite as their principles allow for a flexible applicability which is highly sought after. With this increased need for new and innovative designs from a large space of possibilities, a key question is raised: *how can we find the designs we need?*

1.2 Motivations and Nonlinear Scattering Theory

To facilitate these new applications, refine their use cases, and improve upon their efficiencies, the design process is pivotal in nonlinear nanophotonics. Within this design process lies the nonlinear simulation process, which plays a crucial role[53]. However, these nonlinear simulations can be a costly endeavor for several reasons.

Direct nonlinear simulation is expensive in terms of the time cost of designing, implementing, optimizing, and performing the simulation. To simulate the nonlinear media accurately, a suitable model is required, which then must be transformed into a numerical recipe that can successfully be integrated into some self-consistent solver. For researchers on the cutting edge of development and design, the models being explored for approaches being used are not always available in commercial solvers. As well, independent of whether the software is closed-source[54, 55] or open-source [56], the ability to implement the model oneself simply is not possible.

This leads often to the sole option of directly implementing a model of interest into an in-house solver, which can be an extremely difficult task, especially with the more limited resources a research team may have in comparison to an established software with a large body maintaining and developing it. Differences between models may make them inherently incompatible with any code which previously exists as well, for example, if the order of solving differential equations is required to be different between two approaches. This leads to an inability to easily implement a new model into any existing code available to a researcher, triggering massive projects in refactoring and restructuring large bodies of code, which is only worth the immense time and effort if there is plausible payoff. Not to mention, to implement a model stably into a large piece of software takes a certain amount of numerical

expertise that is not always in a researcher's tool belt if it is not their specialized area.

Lastly, nonlinear simulations can require excessive amounts of computational resources to perform, an amount that can vary greatly depending on the model required. Full nonlinear simulations typically require more resources than linear ones, with more demand on memory and simulation time coming from the added calculation steps and values to keep track of.

All of these are indicative of two key requirements that are not being met: the need for simpler models to facilitate inverse design methods, as well as less costly approaches to, at a minimum, give the researcher the ability to gain some level of accurate information about what result to expect without the need of a full nonlinear simulation and all that it costs.

As the inverse design process is one that relies on a great deal of simulation work to fully realize, it is imperative that the models being used are as simple and efficient as they can be without sacrificing their accuracy. However, since nonlinear models are inherently more complex to simulate, estimative approaches can partially alleviate the number of times the whole nonlinear simulation is performed by providing a rough solution prior to the full optimization. One such estimative method that shows promise for this is Nonlinear Scattering Theory, or NLST in short.

Nonlinear Scattering Theory is a frequency domain method for estimating the nonlinear scattered signal from an arbitrary structure using solely linear simulations, which was developed by Roke et al. in 2004[57]. This method, based on the Lorentz Reciprocity Theorem, is very flexible in terms of applications, and can directly address each of these drawbacks of the full nonlinear simulation approach. A key caveat to NLST being that it fails to be fully self-consistent, limiting its application to the undepleted pump approximation (for reasons demonstrated in Section 3.1). The undepleted pump approximation is a decent approximation in the regime being explored, as it does well for nanophotonic devices with a small interaction volume.

This approach has been used for a qualitative prediction of the relative nonlinear susceptibility of metamaterials by O'Brien et al. in 2015[58] with great success. In that paper, they determine an optimal geometry for a particular nanostructure which maximizes the second harmonic output using Miller's Rule, NLST, and experiment, with NLST proving to yield a result much more in line with experimental results. Despite the normalized, arbitrary units used in this approach, the inclusion of necessary scaling and unit factors in the full derivation imply that quantitative results are indeed also possible to obtain.

Despite being a powerful estimative method with quantitative capabilities, there was no thorough breakdown or validation against a full nonlinear simulation to the best of our knowledge in literature. As well, we noted a distinct lack of a time domain approach, despite some models not being well represented in the frequency domain, especially complex models

like those put forward for HHG[59, 60].

In this thesis, I develop a time domain approach for NLST, as well as perform a comparison of this novel time domain approach to two methodologies in the frequency domain, using the example scenario of Third Harmonic Generation. I then compare the results of nonlinear scattering theory with two types of direct nonlinear simulations, (i) one using an experimental value for the nonlinear optical susceptibility to test the accuracy of the estimative method, and, (ii) for plasmonic systems, a hydrodynamics model for the nonlinear plasmonic response to benchmark the physical performance and examine the accuracy of the results. The purpose for this being to assess the performance of NLST, while outlining and expanding upon its use cases versus direct nonlinear simulations. Further, I assess the possibility of the application of NSLT, particularly our new time domain version, to optimization problems in inverse design. I also consider extensions to more complex nonlinear material responses in the time domain, such as high-order harmonic generation, which is one of our future goals.

Chapter 2

Background Information

To fully understand both the physics and the numerical calculations being performed within Nonlinear Scattering Theory (NLST) and its applications, I will introduce in this chapter the background information regarding how the material response will be calculated for use in NLST. In addition to this, I will introduce Lorentz Reciprocity Theorem in both the frequency domain, where it is most frequently used, as well as the time domain, where the theorem is lesser known.

Note that for this project, the following definitions of the Fourier transform and inverse Fourier transform were used:

$$\vec{P}\left(\vec{r},\omega\right) = \int_{-\infty}^{\infty} \vec{P}\left(\vec{r},t\right) e^{i\omega t} dt \tag{2.1}$$

$$\vec{P}\left(\vec{r},t\right) = \frac{1}{2\pi} \int_{-\infty}^{\infty} \vec{P}\left(\vec{r},\omega\right) e^{-i\omega t} d\omega \tag{2.2}$$

2.1 Material Response

We begin with Maxwell's curl equations for the electric ($\vec{E}$) and magnetic ($\vec{H}$) fields under the assumption of a non-magnetic material, given by:

$$\nabla \times \vec{H}\left(\vec{r},t\right) = \epsilon_0 \frac{d\vec{E}\left(\vec{r},t\right)}{dt} + \frac{d\vec{P}\left(\vec{r},t\right)}{dt} \tag{2.3}$$

$$= \epsilon_0 \frac{d\vec{E}\left(\vec{r},t\right)}{dt} + \vec{J}\left(\vec{r},t\right)$$

$$\nabla \times \vec{E}\left(\vec{r},t\right) = \mu_0 \frac{d\vec{H}\left(\vec{r},t\right)}{dt} \tag{2.4}$$

Where the optical response of the material is described by a polarization ($\vec{P}$) and/or current density ($\vec{J}$), ϵ_0 and μ_0 are the vacuum electric permittivity and permeability, respectively. This material response is what must be characterized for a simulation. Both the linear and nonlinear response of a material to a given field can be encapsulated within this current or polarization term, allowing the current to act (in the case of nonlinear generation) as a nonlinear source current.

In the field of optics there are many ways to describe these responses of a material to various light sources under differing regimes (such as wavelength range and intensity), and understanding how to incorporate these different responses is pivotal to making use of NLST in both the time and frequency domain. How this response is defined and isolated ultimately defines the problem in NLST, hence in this section we will discuss the material responses used in this project and how they originate.

2.1.1 Perturbative Nonlinear Material Response

A perturbative nonlinear material response is used throughout the testing in this project, an approach that views the nonlinear response as a minor perturbation to the linear. Under the regimes where a perturbative response works well, such as low order harmonic generation, the material response can be broken apart into pieces of varying nonlinear orders. That is, to say, we can write the polarization as:

$$\vec{P}_{Tot}\left(\vec{r},t\right)=\vec{P}_{Lin}\left(\vec{r},t\right)+\vec{P}_{NL}\left(\vec{r},t\right)=P_{Lin}\left(\vec{r},t\right)+P^{(2)}\left(\vec{r},t\right)+P^{(3)}\left(\vec{r},t\right)... \tag{2.5}$$

Generally speaking, when dealing with centro-symmetric materials, the even orders tend to vanish within the material due to the symmetry, leaving the second order nonlinearities to the surface boundary only [23]. When dealing with sufficiently small nanostructures, this surface nonlinearity becomes more notably prominent. For testing the NLST approach we focus only on the third order harmonic process, despite the second order processes still being possible to model.

There are many models for the linear response, $\vec{P}_{Lin}\left(\vec{r},t\right)$, that have been developed. Some examples would include the Drude model introduced in 1900[61] to describe the optical response of free electrons in metals, or the Lorentz model introduced in 1909[62] to describe the optical response of bound electrons, such as in dielectrics, along with the variations thereof that followed[63]. Both of these models have been used to describe the linear responses in specific regimes for metallic and dielectric media respectively, and have been studied and characterized in detail. With regard to simulation work, these models have been

fitted for many common materials and are often readily available in solvers or have well documented resources for how to do so[64, 65, 66].

The nonlinear response is independent from the linear model in the perturbative approach, using an expansion which separates many nonlinearities into their corresponding orders. Nonlinear Scattering Theory does not directly depend on whether the nonlinear response can be written out into its various order components, however, it is dependent on the ability of the total polarization to be written as the sum of the linear response and nonlinear pieces, as will be demonstrated with explanation in Section 3. With this assumption, we must define the nonlinear material response.

2.1.2 Instantaneous Material Response from Polychromatic Sources

Looking to the third order nonlinear polarization, as few assumptions will be made to make a model for $\vec{P}^{(3)}(\vec{r},t)$ that can be readily implemented. Beginning with the general third-order nonlinear polarization in a detailed form as a convolution in time and space, we have[67]:

$$\begin{aligned} P_i^{(3)}(\vec{r},t) = \epsilon_0 \int_V \int_{-\infty}^{\infty} \chi_{ijkl}^{(3)}(\vec{r}-\vec{r}_1, \vec{r}-\vec{r}_2, \vec{r}-\vec{r}_3, t-t_1, t-t_2, t-t_3) \\ E_j(\vec{r}_1,t_1)\, E_k(\vec{r}_2,t_2)\, E_l(\vec{r}_3,t_3)\, dt_1 dt_2 dt_3 d\vec{r}_1 d\vec{r}_2 d\vec{r}_3 \end{aligned} \tag{2.6}$$

This specific representation is rather complex, however the assumptions being made can safely simplify its form into something more palatable. The first assumption would be that there are no non-local effects. This removes the influence of nearby fields on this nonlinear polarization, and makes it depend only on the fields at its own point in space. This effectively introduces three spatial delta functions into our $\overleftrightarrow{\chi}^{(3)}$. This assumption simplifies the nonlinear response by eliminating the spatial convolution

$$\overleftrightarrow{\chi}^{(3)} = \overleftrightarrow{\chi}^{(3)}(t-t_1, t-t_2, t-t_3)\, \delta(\vec{r}-\vec{r}_1)\delta(\vec{r}-\vec{r}_2)\delta(\vec{r}-\vec{r}_3), \tag{2.7}$$

giving,

$$\vec{P}^{(3)}(\vec{r},t) = \epsilon_0 \int_{-\infty}^{\infty} \overleftrightarrow{\chi}^{(3)}(\vec{r}, t-t_1, t-t_2, t-t_3)\, \vec{E}(\vec{r},t_1)\, \vec{E}(\vec{r},t_2)\, \vec{E}(\vec{r},t_3)\, dt_1 dt_2 dt_3. \tag{2.8}$$

The next assumption is that the response is instantaneous, performing a similar simplification on the formula for the nonlinear response. By eliminating the time convolution, the $\overleftrightarrow{\chi}^{(3)}$ becomes dependent only on the fields that are currently at that point in time, unaware of the fields that were present prior. That is, we have:

$$\overleftrightarrow{\chi}^{(3)}(\vec{r},t) = \overleftrightarrow{\chi}^{(3)}\delta(\vec{r}-\vec{r}_1)\delta(\vec{r}-\vec{r}_2)\delta(\vec{r}-\vec{r}_3)\delta(t-t_1)\delta(t-t_2)\delta(t-t_3), \tag{2.9}$$

giving,

$$\vec{P}^{(3)}(\vec{r},t) = \epsilon_0 \overleftrightarrow{\chi}(\vec{r})\,\vec{E}(\vec{r},t)\,\vec{E}(\vec{r},t)\,\vec{E}(\vec{r},t)\,. \tag{2.10}$$

Lastly, the assumption is made that there is no variation in time or space for the value of $\overleftrightarrow{\chi}^{(3)}(\vec{r},t)$ within the medium. This would make our nonlinear susceptibility a constant value for values of $\vec{r}$ which lie within the medium, and assumed to be 0 outside, ultimately yielding a drastically simplified formula for the third order nonlinear response within the nonlinear material:

$$\boxed{\vec{P}^{(3)}(\vec{r},t) = \epsilon_0 \overleftrightarrow{\chi}^{(3)}(\vec{r})\,\vec{E}(\vec{r},t)\,\vec{E}(\vec{r},t)\,\vec{E}(\vec{r},t)} \tag{2.11}$$

For comparisons between time and frequency domain NLST discussed in the next chapter, we must transform this polarization into the frequency domain to be used in the original frequency domain NLST method. To do this generally, making no assumptions on the spectral profile of the pump, we apply convolution theorem twice. This yields a nested relationship like such:

$$\mathcal{F}\{f(t)\,g(t)\,h(t)\} = F(\omega) * [G(\omega) * H(\omega)] \tag{2.12}$$

Applying this rule to our formula for the time domain polarization in Equation 2.11, we re-introduce convolutions to the formula for the nonlinear polarization when in the frequency domain.

$$\boxed{\vec{P}(\vec{r},\omega) = \epsilon_0 \overleftrightarrow{\chi}^{(3)}(\vec{r}) \int_{-\infty}^{\infty}\int_{-\infty}^{\infty} \vec{E}(\vec{r},\omega')\,\vec{E}(\vec{r},\omega'')\,\vec{E}(\vec{r},\omega-\omega'-\omega'')\,d\omega' d\omega''} \tag{2.13}$$

This response is applicable to both polychromatic as well as monochromatic fields. For a monochromatic source we see that the convolutions will collapse into a simple cube of the electric fields, which is a form commonly seen in nonlinear optics, given by:

$$\vec{P}(\vec{r},3\omega) = \epsilon_0 \overleftrightarrow{\chi}^{(3)}(\vec{r})\,\vec{E}(\vec{r},\omega)\,\vec{E}(\vec{r},\omega)\,\vec{E}(\vec{r},\omega) \tag{2.14}$$

Often times the $\overleftrightarrow{\chi}^{(3)}$ tensor will exhibit certain symmetries which show a relationship between the varying elements within. This can drastically simplify the appearance of the tensor, or reveal that the number of independent elements is much fewer than there are

indices in the tensor. For example, an isotropic material has a $\overleftrightarrow{\chi}^{(3)}$ tensor with diagonal components that are all equal, with no-off diagonal components. This is used for the one-dimensional test cases in this project.

Many of these symmetries have been given names to assist in the classification of materials. For gold, the nonlinear medium being used in the test cases of this project, the symmetry class is labeled "*m3m*", where diagonal elements are all equal, and the few off-diagonal components are related to these through division by 3.

2.1.3 A Hydrodynamic Response for Gold

Another way to model gold is to use a hydrodynamic model[68], which can be used to capture both non-local and nonlinear effects. Within the scope of this project, this model is not used for bench-marking NLST per se, but rather as a validation for the instantaneous third order nonlinear optical response model described in Section 2.1.2 above to a more complex model that can demonstrate the physical effects overlooked in the previous assumptions. It was implemented in our in-house electrodynamic solver previous to this project by another member of our group[69, 70].

This model is one that attempts to describe the behaviour of the free electrons in a material when in the presence of an electric field, and consists of a Newtonian-like force equation:

$$m\frac{\partial \mathbf{v}}{\partial t} = -e(\vec{E} + \vec{v} \times \vec{B}) - m\vec{v} \cdot \nabla\vec{v} - m\gamma\vec{v} - \nabla\frac{\delta G[n]}{\delta n} \tag{2.15}$$

On the right-hand side of Equation 2.15 we see (from left to right) Lorentz, convection, damping, and pressure functional forces. The pressure term in this model is given by:

$$\frac{\delta G}{\delta n} = \frac{\hbar^2}{2m}\left(3\pi^2\right)^{2/3} n^{2/3} \tag{2.16}$$

Where n is the electron density, m is the effective mass of conduction electrons, and $\hbar$ is the reduced Planck constant. As a formula for the nonlinear polarization or current is required for simulation, a substitution of $\vec{J} = -en\vec{v}$ is used to obtain:

$$\frac{\partial \vec{J}}{\partial t} = \frac{\vec{J}}{ne}\nabla \cdot \vec{J} + \frac{1}{ne}(\vec{J} \cdot \nabla)\vec{J} - \frac{\vec{J}}{en^2}(\vec{J} \cdot \nabla)n + \frac{e^2 n}{m}\left(\vec{E} - \frac{\vec{J}}{ne} \times \vec{B}\right) - \gamma\vec{J} + \frac{e\hbar^2}{3m^2}\left(3\pi^2 n\right)^{2/3}\nabla n \tag{2.17}$$

Where $\vec{J}$ is the material response current, n is the electron density, m is the effective mass of conduction electrons, e is the elementary charge constant, and $\hbar$ is the reduced Planck

constant. A more exhaustive explanation on the model, a numerical linear implementation, and the most recent numerical nonlinear implementation can be found in references [68, 70, 69] respectively.

2.2 Lorentz Reciprocity

Nonlinear Scattering Theory (NLST) is based around the concept of Lorentz Reciprocity in the Frequency Domain. This theorem is an identity in electromagnetism that outlines a symmetry in how fields will behave within the same linear system in the same volume of space. Often, in engineering fields, reciprocity theorem is used to demonstrate the ability to swap detector and emitters in a system [71], meaning that an antenna can act as both a detector through the electric field inducing a current, and as an emitter when the opposite is true. The Lorentz reciprocity theorem is:

$$\int \vec{J}_1(\vec{r},\omega)\cdot\vec{E}_2(\vec{r},\omega)\,dV = \int \vec{J}_2(\vec{r},\omega)\cdot\vec{E}_1(\vec{r},\omega)\,dV \tag{2.18}$$

In the setup for the formula, the currents $\vec{J}_1$ and $\vec{J}_2$ are source currents that give rise to the electric fields $\vec{E}_1$ and $\vec{E}_2$ respectively. The Lorentz reciprocity theorem requires two sets of sources and fields for the relationship to be fully realized. Using information on the fields caused by one current source in a closed system, you can determine the output fields of that same system for any other current source, making it a very powerful theorem. This will be further explained in Section 2.2.1.

This theorem acts as the foundation for Nonlinear Scattering Theory, where this relationship is used to estimate the nonlinear generation and effectively propagate the field to some detector point. It is derived directly from the following vector identity for the divergence of a cross product. This is then combined with Maxwell's curl equations in the frequency domain:

$$\vec{\nabla}\times\vec{E}(\vec{r},\omega) = i\omega\mu\vec{H}(\vec{r},\omega), \tag{2.19}$$

$$\vec{\nabla}\times\vec{H}(\vec{r},\omega) = \vec{J}_{src}(\vec{r},\omega) - \epsilon i\omega\vec{E}(\vec{r},\omega), \tag{2.20}$$

$$\vec{\nabla}\cdot(\vec{A}\times\vec{B}) = (\vec{\nabla}\times\vec{A})\cdot\vec{B} - \vec{A}\cdot(\vec{\nabla}\times\vec{B}), \tag{2.21}$$

where $\vec{J}_{src}$ is a source current, which will later be replaced by $\vec{J}_1$ and $\vec{J}_2$. It is important to note that this is a set of *linear* equations, where the material response is embedded in ϵ and

μ. Given that NLST depends heavily on Lorentz Reciprocity theorem, I will introduce the standard formulation of Lorentz Reciprocity in both the Frequency Domain, as well as in the Time domain, the latter of which I will use to develop a time domain version of NLST in the next chapter.

2.2.1 Formulation in the Frequency Domain

To arrive at Equation 2.18, first one looks to Maxwell's curl equations shown in Equations 2.19 and 2.20. Here, we have a source current, $\vec{J}_{src}(\vec{r},\omega)$, which is generating the electromagnetic fields. Now consider the same physical system under two different sources, $\vec{J}_{src} = \vec{J}_1, \vec{J}_2$, completely contained within a volume V. These sources will generate electromagnetic fields $\vec{E}_1, \vec{H}_1$ and $\vec{E}_2, \vec{H}_2$ within V. If there are two source currents which are active in the region, then there will be two sets of these equations for each of the fields. These fields will from here onward be labeled as $\vec{E}_i, \vec{H}_i, \vec{J}_i$ where $i = 1, 2$. Each of these sets of fields will satisfy a Maxwell curl equation for the respective source current, that is,

$$\begin{aligned}\vec{\nabla} \times \vec{E}_1(\vec{r},\omega) &= i\omega\mu\vec{H}_1(\vec{r},\omega), \\ \vec{\nabla} \times \vec{H}_1(\vec{r},\omega) &= \vec{J}_1(\vec{r},\omega) - \epsilon i\omega\vec{E}_1(\vec{r},\omega),\end{aligned}$$

and

$$\begin{aligned}\vec{\nabla} \times \vec{E}_2(\vec{r},\omega) &= i\omega\mu\vec{H}_2(\vec{r},\omega), \\ \vec{\nabla} \times \vec{H}_2(\vec{r},\omega) &= \vec{J}_2(\vec{r},\omega) - \epsilon i\omega\vec{E}_2(\vec{r},\omega).\end{aligned}$$

By taking the divergence of the cross product between these alternating $\vec{E}$ and $\vec{H}$ fields (i.e. $\vec{\nabla} \cdot (\vec{E}_1 \times \vec{H}_2)$, and $\vec{\nabla} \cdot (\vec{E}_2 \times \vec{H}_1)$), then we can apply the general identity given in Equation 2.21 for the divergence of a cross product. By performing the alternating cross products, and applying this identity, we obtain

$$\vec{\nabla} \cdot (\vec{E}_1 \times \vec{H}_2) = (\vec{\nabla} \times \vec{E}_1) \cdot \vec{H}_2 - \vec{E}_1 \cdot (\vec{\nabla} \times \vec{H}_2), \tag{2.22}$$

$$\vec{\nabla} \cdot (\vec{E}_2 \times \vec{H}_1) = (\vec{\nabla} \times \vec{E}_2) \cdot \vec{H}_1 - \vec{E}_2 \cdot (\vec{\nabla} \times \vec{H}_1). \tag{2.23}$$

Note that for future steps the explicit space and frequency dependence will be dropped in the notation for ease of reading, however, these quantities are still functions of both position

and frequency.

In Equations 2.22 and 2.23, the curl of an $\vec{E}$ and $\vec{H}$ field, are replaced with Maxwell's equations (Equations 2.19 and 2.20). From here, the difference between Equations 2.22 and 2.23 is taken to get

$$\vec{\nabla}\cdot(\vec{E}_1\times\vec{H}_2-\vec{E}_2\times\vec{H}_1) = i\omega(\vec{H}_1\cdot\mu\vec{H}_2-\vec{H}_2\cdot\mu\vec{H}_1)-i\omega(\vec{E}_1\cdot\epsilon\vec{E}_2-\vec{E}_2\cdot\epsilon\vec{E}_1)-\vec{E}_1\cdot\vec{J}_2+\vec{E}_2\cdot\vec{J}_1. \quad (2.24)$$

In the case where with the permeability (μ) and permittivity (ϵ) tensors are symmetric, then it can be shown that $i\omega(\vec{H}_1\cdot\mu\vec{H}_2-\vec{H}_2\cdot\mu\vec{H}_1)$ and $i\omega(\vec{E}_1\cdot\epsilon\vec{E}_2-\vec{E}_2\cdot\epsilon\vec{E}_1)$ will vanish. Equation 2.24 then becomes

$$\vec{\nabla}\cdot(\vec{E}_1\times\vec{H}_2-\vec{E}_2\times\vec{H}_1) = \vec{E}_2\cdot\vec{J}_1-\vec{E}_1\cdot\vec{J}_2. \quad (2.25)$$

To show that the left side of this equation will vanish, the divergence theorem is applied. Let the volume V be a solid region having a boundary surface S with positive orientation and normal unit vector $\vec{n}$. If $\vec{F}$ is a vector field whose components have continuous first order derivatives, then the divergence theorem is written as (as it appears in reference [72])

$$\int_V \vec{\nabla}\cdot\vec{F}dV = \oint_S \vec{F}\cdot\vec{n}dS \quad (2.26)$$

If we apply a closed volume integral to both sides of 2.25, then we can take advantage of the divergence theorem to re-write the left side of the equality, giving

$$\oint_S(\vec{E}_1\times\vec{H}_2-\vec{E}_2\times\vec{H}_1)\cdot\vec{n}dS = \int_V \vec{E}_2\cdot\vec{J}_1-\vec{E}_1\cdot\vec{J}_2dV. \quad (2.27)$$

Both current sources $\vec{J}_1$ and $\vec{J}_2$ are located within the volume bounded by the surface S. If we consider the complementary region of volume $V_c = V_{allspace} - V$, then it gives a region bound by the same surface with only a differing sign on the normal vector, i.e. $\vec{n}\to-\vec{n}$. If we consider 2.27 in this complimentary region of space, we get

$$\oint_S(\vec{E}_1\times\vec{H}_2-\vec{E}_2\times\vec{H}_1)\cdot(-\vec{n})dS = \int_{V_c}\left[\vec{E}_2\cdot\vec{J}_1-\vec{E}_1\cdot\vec{J}_2\right]dV. \quad (2.28)$$

Noting that there are no current sources in this complimentary volume, it is trivial to see that the right side would vanish. Seeing as the left side differs only by a global minus sign from the situation involving our original region V, one can conclude that

$$\oint_S (\vec{E}_1 \times \vec{H}_2 - \vec{E}_2 \times \vec{H}_1) \cdot \vec{n} dS = -\oint_S (\vec{E}_1 \times \vec{H}_2 - \vec{E}_2 \times \vec{H}_1) \cdot (-\vec{n}) dS = 0. \tag{2.29}$$

There is another conceptual way to show the disappearance of the term on the left-hand side of Equation 2.27. Assuming that the fields can be encapsulated within a bounding surface, they must decay as they propagate outward. This implies that there is some surface large enough where the fields have decayed to negligible levels. As the surface expands to infinity, the current sources on the right-hand side will remain fixed, whereas the fields on the left must approach zero. Thus, the term on the left-hand side of Equation 2.27 must vanish.

Moving the remaining current terms to each side of the equality, we rearrange to ultimately yield Lorentz Reciprocity Theorem:

$$\boxed{\int_V \vec{J}_2(\vec{r},\omega) \cdot \vec{E}(\vec{r},\omega)\, dV = \int_V \vec{J}_1(\vec{r},\omega) \cdot \vec{E}_2(\vec{r},\omega)\, dV} \tag{2.30}$$

With only minor constraints, Equation 2.30 allows for the detection of the output fields for an enclosed system for nearly any current source. It is important that all fields exist at the frequency for which reciprocity is being evaluated, otherwise the relationship can give no information.

There is one constraint applied in the derivation of Equation 2.16 that may not always hold true in nanophotonic simulations, specifically the one used for the elimination of the left-hand side of Equation 2.27. Under the situation of periodic boundary conditions in the simulation domain, or a case where fields do not decay as they propagate (e.g. one dimensional cases), then no surface can be drawn that encompasses the entirety of the fields. However, in the one-dimensional situations evaluated in this project, it was always found to be more than enough orders of magnitude smaller than the right-hand side of Equation 2.27 to be treated as negligible.

2.2.2 Formulation in the Time Domain

A similar equation for Lorentz Reciprocity can be formulated entirely in the time domain. The derivation follows a similar pathway to that in the frequency domain examined previously, beginning with Maxwell's curl equations in the time domain, but now making use of the $\vec{B}$ and $\vec{D}$ fields to account for a time response function of μ and ϵ , respectively,

$$\vec{\nabla} \times \vec{E}(t) = -\frac{\partial \vec{B}(t)}{\partial t}, \tag{2.31}$$

$$\vec{\nabla} \times \vec{H}(t) = \vec{J}(t) + \frac{\partial \vec{D}(t)}{\partial t}, \tag{2.32}$$

where we assume there is a set of (linear) constitutive relations that relates $\vec{D}$ to $\vec{E}$ and $\vec{H}$ to $\vec{B}$.

Suppose two set of fields, $\vec{D}_i, \vec{E}_i, \vec{H}_i, \vec{B}_i$ where $i = 1, 2$, are solutions to Equations 2.31 and 2.32, for distinct source currents $\vec{J}_i$. We begin by applying a time reversal to the first set of fields. This time reversal transforms all $i = 1$ fields like $\vec{D_1}(t) \to \vec{D_1}(\tau - t)$, for an arbitrary time τ.

Continuing, the derivation will follow that in the frequency domain, where we apply Equation 2.21, combined with Equations 2.31 and 2.32 to obtain

$$\begin{aligned}\vec{\nabla} \cdot \left[\vec{E}_1(\tau - t) \times \vec{H}_2(t) - \vec{E}_2(t) \times \vec{H}_1(\tau - t)\right] = \vec{H}_2(t) \cdot \frac{\partial \vec{B}_1(\tau - t)}{\partial t} + \vec{H}_1(\tau - t) \cdot \frac{\partial \vec{B}_2(t)}{\partial t} \\ - \vec{E}_1(\tau - t) \cdot \vec{J}_2(t) + \vec{E}_2(t) \cdot \vec{J}_1(\tau - t) \\ - \vec{E}_2(t) \cdot \frac{\partial \vec{D}_1(\tau - t)}{\partial t} - \vec{E}_1(t) \cdot \frac{\partial \vec{D}_2(t)}{\partial t}.\end{aligned} \tag{2.33}$$

Next, an integration is performed over all time, which will lead to the vanishing of the terms containing $\vec{B}_i$ and $\vec{D}_i$. This only needs to be argued for one of the two, as analogous steps are performed for each. To show this, I will use the electric and displacement field pairs, $\vec{E}_i$ and $\vec{D}_i$, which we assume are related through the constitutive relation

$$\vec{E}_2(t) \cdot \frac{\partial \vec{D}_1(\tau - t)}{\partial t} + \vec{E}_1(\tau - t) \cdot \frac{\partial \vec{D}_2(t)}{\partial t}, \tag{2.34}$$

$$\vec{D}(t) = \int_{-\infty}^{\infty} \overleftrightarrow{\epsilon}(t') \vec{E}(t - t') dt' \tag{2.35}$$

To maintain causality, we have that $\vec{E}(t) = 0 \; \forall \; t < t_0$, and thus $t' < t - t_0$. Furthermore, if we assume that the current densities $\vec{J}_i$ are zero before some specific time (taken to be, say, $t = 0$) , then the response function $\overleftrightarrow{\epsilon}(t) = 0 \; \forall \; t < 0$. Thus the integration in Equation 2.35 ultimately takes place over the finite range

$$D(t) = \int_{0}^{t - t_0} \overleftrightarrow{\epsilon}(t') \vec{E}(t - t') dt'. \tag{2.36}$$

With these new finite integration bounds, we substitute Equation 2.36 for the $\frac{\partial \vec{D}_i(t)}{\partial t}$

terms in Equation 2.33, giving

$$\int_{-\infty}^{\infty} \vec{E}_2(t) \cdot \frac{\partial \vec{D}_1(\tau - t)}{\partial t} + \vec{E}_1(\tau - t) \cdot \frac{\partial \vec{D}_2(t)}{\partial t} dt = \int_{-\infty}^{\infty} \vec{E}_2(t) \cdot \frac{\partial}{\partial t}\Big[\int_0^{t-t_0} \overleftrightarrow{\epsilon}(t')\vec{E}_1(\tau - t - t')dt'\Big] + \vec{E}_1(\tau - t) \cdot \frac{\partial}{\partial t}\Big[\int_0^{t-t_0} \overleftrightarrow{\epsilon}(t')\vec{E}_2(t - t')dt'\Big]dt. \tag{2.37}$$

For the next few steps we define the left-hand side of Equation 2.37 to be the variable I for readability. That is,

$$I = \int_{-\infty}^{\infty} \vec{E}_2(t) \cdot \frac{\partial \vec{D}_1(\tau - t)}{\partial t} + \vec{E}_1(\tau - t) \cdot \frac{\partial \vec{D}_2(t)}{\partial t} dt.$$

Next, the integration over t is focused upon, gathering all terms dependent, giving us

$$I = \int_0^{t-t_0} \overleftrightarrow{\epsilon}(t')\Big[\int_{-\infty}^{\infty} \vec{E}_2(t) \cdot \frac{\partial}{\partial t}\vec{E}_1(\tau - t - t')dt + \int_{-\infty}^{\infty} \vec{E}_1(\tau - t) \cdot \frac{\partial}{\partial t}\vec{E}_2(t - t')dt\Big]dt'. \tag{2.38}$$

Since our values of t' are in actuality finite, we can shift the integrand functions by t' without affecting their value. Meaning for the integral below, we can substitute $t'' = t + t'$, giving us

$$\int_{-\infty}^{\infty} \vec{E}_2(t) \cdot \frac{\partial}{\partial t}\vec{E}_1(\tau - t - t')dt' = \int_{-\infty}^{\infty} \vec{E}_2(t'' - t') \cdot \frac{\partial}{\partial t'}\vec{E}_1(\tau - t'')dt''. \tag{2.39}$$

Given that t'' is simply a dummy variable for integration, we can drop the double prime and return it back to just t for the next step. By substituting this back into Equation 2.38, we are left with

$$I = \int_0^{t-t_0} \overleftrightarrow{\epsilon}(t') \left[\int_{-\infty}^{\infty} \vec{E}_2(t - t') \cdot \frac{\partial}{\partial t}\vec{E}_1(\tau - t)dt + \int_{-\infty}^{\infty} \vec{E}_1(\tau - t) \cdot \frac{\partial}{\partial t}\vec{E}_2(t - t')dt\right] dt', \tag{2.40}$$

where the right-hand side of the is clearly the result of the product rule of derivatives, allowing for our next step. We rearrange to obtain

$$\begin{aligned}
&\int_{-\infty}^{\infty} \vec{E}_2(t') \cdot \frac{\partial \vec{D}_1(\tau - t)}{\partial t} + \vec{E}_1(\tau - t') \cdot \frac{\partial \vec{D}_2(t)}{\partial t} dt' \\
&= \int_0^{t-t_0} \overleftrightarrow{\epsilon}(\lambda) \Big[\int_{-\infty}^{\infty} \frac{\partial}{\partial t} [\vec{E}_2(t' - \lambda) \cdot \vec{E}_1(\tau - t')] dt' \Big] d\lambda \qquad (2.41) \\
&= \int_0^{t-t_0} \overleftrightarrow{\epsilon}(\lambda) \Big[\vec{E}_2(t' - \lambda) \cdot \vec{E}_1(\tau - t') \Big] \Big|_{t'=-\infty}^{\infty} d\lambda.
\end{aligned}$$

Since $\vec{E}_i(-\infty) = \vec{E}_i(\infty) = 0$ by our constraints, it is clear that this term vanishes. Identical arguments can be made for the $\vec{B}_i$ terms. Thus, Equation 2.33 becomes

$$\int_{-\infty}^{\infty} \vec{\nabla} \cdot \Big[\vec{E}_1(\tau - t) \times \vec{H}_2(t) - \vec{E}_2(t) \times \vec{H}_1(\tau - t) \Big] dt = \qquad (2.42)$$

$$\int_{-\infty}^{\infty} \Big[\vec{E}_2(t) \cdot \vec{J}_1(\tau - t) - \vec{E}_1(\tau - t) \cdot \vec{J}_2(t) \Big] dt. \qquad (2.43)$$

Similar to the Frequency domain formulation, performing a volume integration, and applying the divergence theorem to the left-hand side will show that the curl terms will vanish. This leaves us in the time domain with:

$$\boxed{\int_{-\infty}^{\infty} \int_V \vec{J}_2(\vec{r}, t) \cdot \vec{E}_1(\vec{r}, \tau - t) \, dV dt = \int_{-\infty}^{\infty} \int_V \vec{J}_1(\vec{r}, \tau - t) \cdot \vec{E}_2(\vec{r}, t) \, dV dt} \qquad (2.44)$$

Analogous to the frequency domain, Equation 2.30 allows for the detection of the output fields for an enclosed system for nearly any current source, with only minor constraints. Non-monochromatic sources were a key assumption in the derivation, where the fields only exist within some finite time window. However, there is no constraint on how large that time window be, meaning that it is still applicable to very narrow-band fields which can yield results similar to the monochromatic case.

As for the frequency domain formulation, there remains here the constraint that the surface integral term does not vanish in the case of periodic boundary conditions or non-decaying fields. Ultimately, as Lorentz reciprocity is defined as being a theorem applicable to closed systems, both approaches still require that a closed surface can be drawn that encloses the entirety of the fields.

Chapter 3

Nonlinear Scattering Theory

To understand how Lorentz Reciprocity theorem is used to estimate nonlinear generation via NSLT, first each term within the theorem must be clearly defined. Below, we have our frequency and time domain Lorentz Reciprocity theorems:

$$\boxed{\int_V \vec{J}_2(\vec{r},\omega)\cdot\vec{E}_1(\vec{r},\omega)\,dV = \int_V \vec{J}_1(\vec{r},\omega)\cdot\vec{E}_2(\vec{r},\omega)\,dV} \tag{3.1}$$

$$\boxed{\int_{-\infty}^{\infty}\int_V \vec{J}_2(\vec{r},t)\cdot\vec{E}_1(\vec{r},\tau-t)\,dV\,dt = \int_{-\infty}^{\infty}\int_V \vec{J}_1(\vec{r},\tau-t)\cdot\vec{E}_2(\vec{r},t)\,dV\,dt} \tag{3.2}$$

As per the formulation, the currents in these formulas, $\vec{J}_1$ and $\vec{J}_2$, are *source* currents, leading to the generation of the electric fields $\vec{E}_1$ and $\vec{E}_2$ respectively. If we establish our source currents in a particular way to suit our end goal, we can then use this relationship to determine an unknown field. With this, we can now begin painting a picture of the theoretical setup for an NLST calculation.

To outline the setup for Nonlinear Scattering Theory, I will use an example case of third harmonic generation from an arbitrarily shaped non-magnetic nanostructure that exhibits an instantaneous local third order nonlinear response described by Equation 2.11 in Section 2.1.2. For the sake of ease of understanding the method, all formulas will appear in the frequency domain where they appear simpler.

In this chapter, I begin by introducing the system setup in Section 3.1, followed by my derivation for NLST in the time domain through Maxwell's equations in Section 3.2. The essence of NLST is to determine a nonlinear generated signal via the use of two *linear* simulations: one with a source that generates the nonlinear polarization within a nonlinear medium, and a second with a fictitious source at a location in the far field at which we would like to determine the nonlinear signal. We will now go through how to set up these

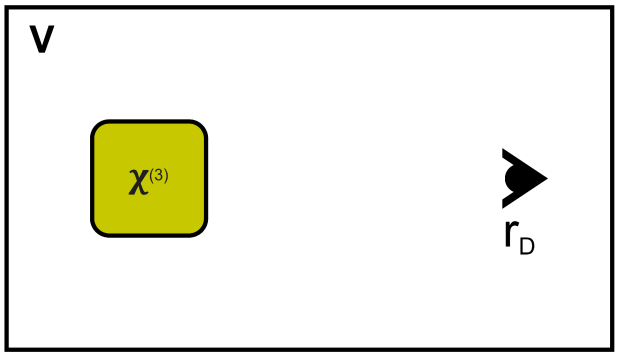

Figure 3.1: **The NLST Region**

simulations in detail.

3.1 The Problem Setup for NLST

Consider an arbitrarily shaped, non-magnetic nanostructure with a known nonlinear susceptibility $\chi^{(3)}$, described by

$$\vec{P}(\vec{r},3\omega) = \epsilon_0 \overleftrightarrow{\chi}^{(3)}(\vec{r},\omega)\,\vec{E}(\vec{r},\omega)\,\vec{E}(\vec{r},\omega)\,\vec{E}(\vec{r},\omega)\,. \tag{3.3}$$

This nanostructure is enclosed within a volume of space, V, that also contains a detector point labeled as $\vec{r}_D$. This region is pictured in Figure 3.1. Specifically, we are interested in the nonlinear scattered signal this structure will generate under a certain driving field, when detected at the detector point $\vec{r}_D$.

The Forward Simulation

Consider a pump source at a frequency ω_0 incident on the nanostructure from the left as visualized in Figure 3.2. This is the first simulation for Nonlinear Scattering Theory calculations, and is where we begin to define our first set of fields.

This driving signal simulation I call the "Forward" simulation, and it is used to define our first set of fields $\vec{E}_1$ and $\vec{J}_1$. When this driving signal passes through the nanostructure, it produces a full material response that includes the linear and nonlinear parts $\vec{P}_{Lin}$ and $\vec{P}_{NL}$. This response, can be represented as a polarization density, or a current density depending on the model being used, that is,

$$\vec{P}_{Tot}(\vec{r},\omega) = \vec{P}_{Lin}(\vec{r},\omega) + \vec{P}_{NL}(\vec{r},\omega)\,, \tag{3.4}$$

or

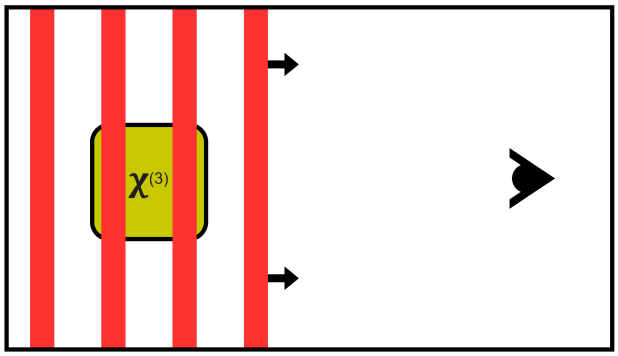

Figure 3.2: **The Driving Field for NLST**

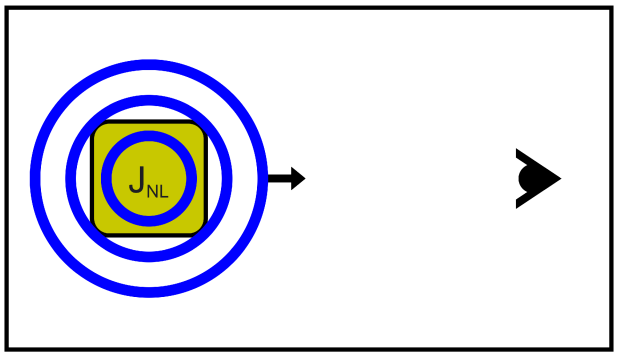

Figure 3.3: **The Nonlinear Generation Propagates Toward the Detector Field** The nonlinear response of the material generates an electromagnetic field which propagates uniformly outward toward the detector point.

$$\vec{J}_{Tot}\left(\vec{r},\omega\right) = -i\omega\vec{P}_{Lin}\left(\vec{r},\omega\right) - i\omega\vec{P}_{NL}\left(\vec{r},\omega\right). \tag{3.5}$$

Ultimately, the polarization and current densities are related to each other via a time derivative, or in the frequency domain, a factor of $-i\omega$ given the definitions of the Fourier transform given in Equations 2.1 and 2.2. The nonlinear current is the source current for the nonlinear generation. If this were a direct nonlinear simulation, $\vec{J}_1$ would produce an electric field $\vec{E}_1$ that propagates within the volume toward the detector, as pictured in Figure 3.3. However, $\vec{E}_1$ itself is not calculated directly within NLST linear simulations. Rather, its value at the detector point will be inferred, as we will see.

To perform NLST, we make use of the *undepleted pump approximation*, where the nonlinear polarization is a function of the pump fields, but the pump remains unaffected by the nonlinear optical process. This approximation is typically a safe one in nonlinear nanophotonics as the nonlinearities in many media are quite small. This allows us write, for third harmonic generation,

$$J_{1,i}\left(\vec{r},\omega=3\omega_0\right)=-i\omega\epsilon_0\chi^{(3)}_{ijkl}\int_{-\infty}^{\infty}\int_{-\infty}^{\infty}E_j\left(\vec{r},\omega'\right)E_k\left(\vec{r},\omega''\right)E_l\left(\vec{r},\omega-\omega'-\omega''\right)d\omega' d\omega'' \quad (3.6)$$

$$\approx -i\omega\epsilon_0\chi^{(3)}_{ijkl}\int_{-\infty}^{\infty}\int_{-\infty}^{\infty}E_{Lin,j}\left(\vec{r},\omega'\right)E_{Lin,k}\left(\vec{r},\omega''\right)E_{Lin,l}\left(\vec{r},\omega-\omega'-\omega''\right)d\omega' d\omega'', \quad (3.7)$$

Where $\vec{E}$ and $\vec{E}_{Lin}$ represent the total and linear electric fields, respectively. Given the typically many orders of magnitudes difference between the strength of linear and nonlinear responses, this is often a safe assumption to make. This undepleted pump approximation allows us to perform a linear forward simulation, and calculate the source current for the nonlinear generation.

The linear field, $\vec{E}_{Lin}$, for sake of clarity, is the electric field profile near the fundamental frequency induced within the nonlinear structure, as excited by an external source centered at the fundamental frequency, drawn in Figure 3.2 as a plane wave; all nonlinear processes that affect the fundamental frequency are ignored. $\vec{E}_{Lin}$ is found from a linear simulation, using the linear ϵ, and is then inserted into equation 3.7 to find the induced nonlinear current $\vec{J}_1$. The field we seek is the one that would be generated by $\vec{J}_1$ – this is $\vec{E}_1$, and we seek it in the far field. As $\vec{J}_1$ has been defined as the source current for nonlinear generation, our field electric field $\vec{E}_1$ is consequently defined as the nonlinear signal over the volume V. We now use the Lorentz Reciprocity theorem to find $\vec{E}_1$ in the far field (at the detector point), by cleverly choosing $\vec{J}_2$, and performing a second linear simulation.

The Backward Simulation

Now I introduce the second simulation, which I refer to as the "backward" simulation, and is a linear simulation centered at the nonlinear frequency. This simulation uses a source current from a fictitious current density source located in the same domain as the forward simulation, but emanating from the detector point $\vec{r}_D$, as illustrated in Figure 3.4. There are two goals to this step: to estimate the generated field at the detector point, and to account for the physical effects the generated third harmonic will experience including scattering from and losses within the nanostructure. We thus use a broadband source centered at the third harmonic, which we take to be a delta function in space.

Looking at the left-hand side of the Lorentz Reciprocity relations in both the frequency and time domain (Equations 3.1 and 3.2, respectively), we see that the electric field we seek at the detector point sits within a volume integral. By selecting a fictitious $\vec{J}_2$ that exists *only* at the detector point (e.g. an oscillating electric dipole), the nonlinear signal field $\vec{E}_1$

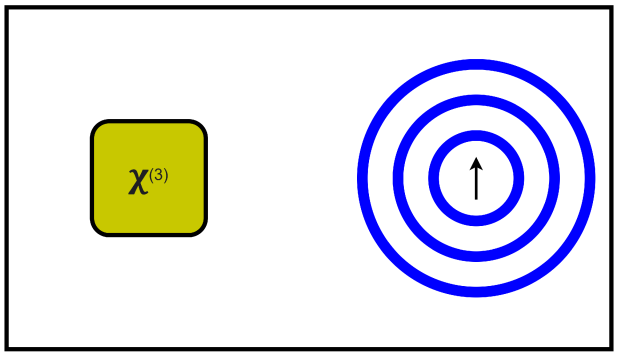

Figure 3.4: **A Fictitious Current Source at the Detector**
A fictitious dipole source is located at the detector point, generating an electric field which propagates toward our nanostructure.

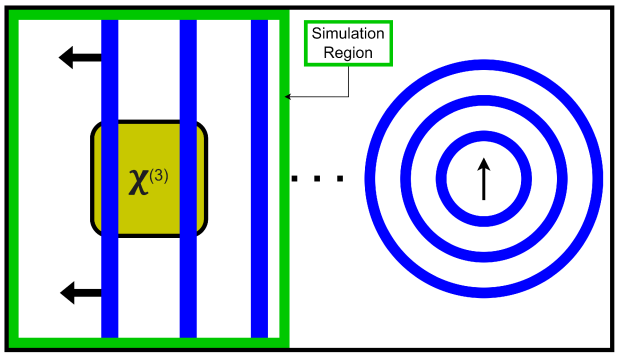

Figure 3.5: **Plane Wave Approximation of the Fictitious Current Source**
The fictitious source is placed far from the structure so a plane wave approximation can be made.

precisely at that desired detector point will be pulled out of the volume integral. Thus, we set the source of our backward simulation to be an oscillating dipole located at the detector point, as pictured in Figure 3.4.

As we are interested in the nonlinear generation in the far field, a second simplification can be made. Provided the desired detector location is sufficiently far from the nonlinear structure, we can approximate the spherical wavefront of the fictitious source as plane-like by the time it reaches the nanostructure.

This is a simplification used in this project, so that the simulation domain can be decreased and therewith the computational resources required. The backward simulation is thus a plane wave source coming from the direction of the detector point, to which we then apply scaling factors discussed in Section 3.3.1 to obtain quantitative results. This simplification is visualized in Figure 3.5.

Since our forward simulation current source, $\vec{J}_1$, is the nonlinear response of the struc-

ture, it is confined entirely to the volume of the nonlinear structure. The backward simulation instead monitors the linear fields inside the nonlinear structure centered at the nonlinear frequency (third harmonic) that is caused by our fictitious source. We choose the fictitious source to be broadband and centered at the third harmonic. This way, the physical effects which the nonlinear generation will experience (e.g. losses, scattering, propagation) becomes encapsulated within $\vec{E}_2$. Once $\vec{E}_2$ and $\vec{J}_1$ within the nanostructure are known, we then apply the Lorentz reciprocity theorem in Equation 3.1 to obtain $\vec{E}_1$ at the detector point. The details of this are discussed later in Section 3.3.

3.2 Extending NLST into the Time Domain

Nonlinear scattering theory as it was previously developed in the literature [57, 58], and outlined in Section 3.1, was a frequency domain method. In this section, I will derive a comparable theory for the time domain, making clear along the way all the required assumptions. To demonstrate that the set of linear equations required for NLST can be given in the time domain, we examine the forward simulation. As the driving signal passes through the enclosed system as shown in Figure 3.2, the displacement field within the volume, under the assumption of a separable linear and nonlinear response, can be written as

$$\vec{D}\left(\vec{r},t\right) = \epsilon_0 \vec{E}\left(\vec{r},t\right) + \vec{P}_{Lin}\left(\vec{r},t\right) + \vec{P}_{NL}\left(\vec{r},t\right), \tag{3.8}$$

where $\vec{E}$ is the total electric field, and $\vec{P}_{Lin}$, $\vec{P}_{NL}$ are the linear and nonlinear polarization densities, respectively. In this scenario, it does not matter that nonlinear orders themselves are separable, only that the linear and nonlinear ones are.

There are two electric fields present in the physical system: (1) the driving signal that is passing through the system, $\vec{E}_0$, and (2) the nonlinear fields which are generated by the nonlinear response, $\vec{E}_{NL}$. Thus, the displacement field can be written as

$$\vec{D}\left(\vec{r},t\right) = \epsilon_0 \vec{E}_0\left(\vec{r},t\right) + \epsilon_0 \vec{E}_{NL}\left(\vec{r},t\right) + \vec{P}_{Lin}\left(\vec{r},t\right) + \vec{P}_{NL}\left(\vec{r},t\right). \tag{3.9}$$

As $\vec{P}_{Lin}$ is a polarization density that is (by definition) only dependent on the total electric field, $\vec{E}_{Tot} = \vec{E}_0 + \vec{E}_{NL}$, it can also be expanded into two parts: the linear response to the original pump field, $\vec{P}_{Lin,0}$, and the linear response to the nonlinear generated fields, $\vec{P}_{Lin,NL}$. This allows us to rewrite Equation 3.9 as

$$\vec{D}\left(\vec{r},t\right) = \epsilon_0 \vec{E}_0\left(\vec{r},t\right) + \vec{P}_{Lin,0}\left(\vec{r},t\right) + \epsilon_0 \vec{E}_{NL}\left(\vec{r},t\right) + \vec{P}_{Lin,NL}\left(\vec{r},t\right) + \vec{P}_{NL}\left(\vec{r},t\right). \tag{3.10}$$

From left to right, the first two terms on the right-hand side of Equation 3.10 are dependent only on $\vec{E}_0$, the linear fields from the pump simulation as described in Section 3.1. The third and fourth terms are dependent on only $\vec{E}_{NL}$, the nonlinear generated field that we are interested in determining. Only the final term, $\vec{P}_{NL}$, is dependent on both $\vec{E}_0$ and $\vec{E}_{NL}$ in an inseparable way, as it is a nonlinear equation. Thus, we again operate under *the undepleted pump approximation*, and assume that the nonlinear current, $\vec{P}_{NL}$, is not dependent on the total fields, and instead is a function of just the linear pump field $\vec{E}_0$. Since $\vec{P}_{NL}$ is the source for $\vec{E}_{NL}$, and does not affect the pump fields under the approximation being used, we rewrite the displacement field in two parts: the displacement field resulting

from the response to the pump,

$$\vec{D}_0\left(\vec{r},t\right)=\epsilon_0\vec{E}_0\left(\vec{r},t\right)+\vec{P}_{Lin,0}\left(\vec{r},t\right), \tag{3.11}$$

and the displacement field resulting from the linear response of the nonlinear generated fields

$$\vec{D}_{Lin,NL}\left(\vec{r},t\right)=\epsilon_0\vec{E}_{NL}\left(\vec{r},t\right)+\vec{P}_{Lin,NL}\left(\vec{r},t\right), \tag{3.12}$$

giving us a simplified for Equation 3.10,

$$\vec{D}\left(\vec{r},t\right)=\vec{D}_0\left(\vec{r},t\right)+\vec{D}_{Lin,NL}\left(\vec{r},t\right)+\vec{P}_{NL}\left(\vec{r},t\right). \tag{3.13}$$

Just as there are two electric fields, $\vec{E}_0$ and $\vec{E}_{NL}$, there are also two magnetic fields, given by

$$\vec{H}\left(\vec{r},t\right)=\vec{H}_0\left(\vec{r},t\right)+\vec{H}_{NL}\left(\vec{r},t\right). \tag{3.14}$$

We substitute Equations 3.13 and 3.14 into Maxwell's curl equation for the magnetic fields in the time domain as given in Equation 2.32 to obtain

$$\vec{\nabla}\times\vec{H}_0\left(\vec{r},t\right)+\vec{\nabla}\times\vec{H}_{NL}\left(\vec{r},t\right)=\frac{\partial\vec{D}_0\left(\vec{r},t\right)}{\partial t}+\frac{\partial\vec{D}_{Lin,NL}\left(\vec{r},t\right)}{\partial t}+\frac{\partial\vec{P}_{NL}\left(\vec{r},t\right)}{\partial t} \tag{3.15}$$

$$=\frac{\partial\vec{D}_0\left(\vec{r},t\right)}{\partial t}+\frac{\partial\vec{D}_{Lin,NL}\left(\vec{r},t\right)}{\partial t}+\vec{J}_{NL}\left(\vec{r},t\right) \tag{3.16}$$

When examining our newly expanded full curl equation, we note the fact that the fields subscripted "0" are independent of those that are not, and thus can be separated into their own curl equation,

$$\vec{\nabla}\times\vec{H}_0\left(t\right)=\frac{\partial\vec{D}_0\left(t\right)}{\partial t}, \tag{3.17}$$

where there is no source current present as the source in this case (the pump) comes from outside the volume of interest. This leaves the remaining terms in another curl equation,

$$\vec{\nabla}\times\vec{H}_{NL}\left(t\right)=\vec{J}_{NL}\left(t\right)+\frac{\partial\vec{D}_{Lin,NL}\left(t\right)}{\partial t}, \tag{3.18}$$

which is an entirely linear equation for the nonlinear fields, where the source current is nonlinearly dependent on $\vec{D}_0$ and $\vec{H}_0$, which are known independently from Equation 3.18.

Lorentz reciprocity theorem uses one set of fields for a given source to reveal a second

set of fields for a second current source. Its usability is dictated by whether or not the linear equation presented in Equation 3.18 is true for the system, which at a glance makes it seem the Lorentz reciprocity is completely incompatible with nonlinear nanophotonics. What this derivation shows is that the linear equation can be constructed in the time domain using the undepleted pump approximation, demonstrating that NLST is applicable in the time domain as well.

Using the linear forward simulation as described in Section 3.1 and visualized in Figure 3.2, we monitor the linear fields in the nonlinear nanostructure, $\vec{E}_0(\vec{r}, t)$, and calculate a corresponding nonlinear source current, $\vec{J}_{NL}$, in time using an instantaneous perturbative nonlinear response model like the one given in Equation 2.11. The backward simulation is then performed to provide us the necessary second set of fields that Lorentz reciprocity theorem requires, allowing for NLST to be performed, the accuracy of which is ultimately limited by the approximations made in this section (undepleted pump) and in Section 2.2.2 (i.e. finite fields in time which decay to zero by the boundary of the volume of interest, and a convolutional linear response).

Using Equation 3.18 as one of the two starting equations in the derivation found in Section 2.2.2, all steps will follow through similarly, yielding once again Lorentz reciprocity in the time domain that can be used under the constraint of a convolutional linear response in time to estimate the nonlinear signal from an arbitrarily shaped, non-magnetic structure, with a known formula for the dependence of the nonlinear current on the fields determined by the linear pump simulation in Equation 3.17.

It is worth noting here that there no assumptions being made regarding the form of the nonlinear current, $\vec{J}_1$. Provided that the linear response is separable from the nonlinear, and the linear responses can be written as a convolution (assumed in the time domain derivation of Lorentz Reciprocity in Section 2.2.2), then the nonlinear response can be much more complicated, and even a non-convolutional model such as those being theorized for high-order harmonic generation[59], can be used.

3.3 Numerical Recipes for NLST

3.3.1 Numerical Recipe for NLST in the Frequency Domain

In this section, we will transform the formula for frequency domain Lorentz Reciprocity into a numerical recipe for use in computational nanophotonics. Beginning with our formula for Lorentz Reciprocity in the frequency domain (Equation 3.1), we start by noting that the use of a delta function in space was discussed for the secondary source in order to isolate the scattered field at some detector point. We will use a separation of variable dependence for this secondary current, and represent it as

$$\vec{J}_2\left(\vec{r},\omega\right) = \vec{J}_{20}\left(\omega\right)\delta\left(\vec{r}-\vec{r}_D\right), \tag{3.19}$$

where $\vec{J}_{20}(\omega)$ is the separated frequency profile of $\vec{J}_2\left(\vec{r},\omega\right)$.

In computation, a delta function in space is not possible as the volume V is discretized. For this reason, this numerical recipe must instead approach the isolation at the detector position differently. We adjust our definition of $\vec{J}_2$ to instead be a sphere of uniform current density, and choose the radius of the sphere, r_0, such that the volume of the sphere equals the volume of a computational grid cell, with dimensions along the x, y, and z Cartesian axes given by Δx, Δy, and Δz. Then the radius of the equivalent volume sphere source is given by

$$r_0 = \sqrt[3]{\frac{3}{4\pi}\Delta x\Delta y\Delta z}. \tag{3.20}$$

We then place the current far from the structure, as we would like our detection point to be in the far field. It is unrealistic to make the simulation volume large enough to include this detector point. Rather, we assume it is so far away that the wave emanating from it will be approximately a plane wave by the time it reaches the nanostructure. However, *what is the amplitude of the plane wave?* It is important to have a known amplitude to obtain quantitative estimates. In Appendix B, we derive analytically the far field emanating from a spherical current source with radius r_0, and find it to be

$$\vec{E}\left(\vec{r},\omega\right) = -\frac{i\omega\mu_0 r_0^3}{2r}\left(1-\frac{i}{kr}\right)e^{ikr}J\left(\omega\right)\hat{j} \tag{3.21}$$

Next we consider the field $\vec{E}_1$ at the detector point. As the current source $\vec{J}_2$ was over a sphere, we must also consider that our detection of $\vec{E}_1$ also occurs over the same sphere. To do this, we obtain the far field value of $\vec{E}_1$ at the sphere, and assume it is uniform over the sphere's extent. Thus, the volume integral over $\vec{J}_2$ and $\vec{E}_1$ becomes

$$\int_V \vec{J}_2(\vec{r},\omega)\cdot\vec{E}_1(\vec{r},\omega)\,dV \approx \vec{J}_{20}(\omega)\cdot\vec{E}_1(\vec{r}_D,\omega)\,\Delta x\Delta y\Delta z.$$

We now look to the volume integration over the nonlinear nanostructure. For this, a standard Riemann-style integration gives

$$\int_V \vec{J}_1(\vec{r},\omega)\cdot\vec{E}_2(\vec{r},\omega)\,dV \approx \sum_p \vec{J}_1(\vec{r}_p,\omega)\cdot\vec{E}_2(\vec{r}_p,\omega)\,\Delta x\Delta y\Delta z,$$

where $\vec{r}_p$ refers to the discretized locations within the nanostructure, enumerated by the index p. We are left with

$$\vec{J}_{20}(\vec{r}_D,\omega)\cdot\vec{E}_1(\vec{r}_D,\omega) = \sum_p \vec{J}_1(\vec{r}_p,\omega)\cdot\vec{E}_2(\vec{r}_p,\omega). \tag{3.22}$$

If we assume a linearly polarized $\vec{J}_2$ in the plane transverse to the propagation direction, then the resulting scattered field we solve for will be the component with this polarization. With an isotropic $\chi^{(3)}$, this will be the only resulting nonlinear scattered field. However, in a non-isotropic case, multiple simulations with orthogonal backward source currents are required to determine the total magnitude of the scattered nonlinear electric field, $\vec{E}_1$. Generally speaking, the dot product can be rewritten as the sum of the products of the i^{th} component of the fields $\vec{J}_1$ and $\vec{E}_2$,

$$J_{20,j}(\vec{r}_D,\omega)\,\vec{E}_{1,j}(\vec{r}_D,\omega) = \sum_{pi} \vec{J}_{1,i}(\vec{r}_p,\omega)\cdot\vec{E}_{2,i}(\vec{r}_p,\omega)$$

$$\Rightarrow \boxed{\vec{E}_{1,j}(\vec{r}_D,\omega) = \frac{1}{J_{20,j}(\vec{r}_D,\omega)}\sum_{pi} \vec{J}_{1,i}(\vec{r}_p,\omega)\cdot\vec{E}_{2,i}(\vec{r}_D,\omega)} \tag{3.23}$$

In this project, solely the z-component is considered as it contains the majority of the nonlinear generation due to our chosen setup.

3.3.2 Numerical Recipe for NLST in the Time Domain

Previously in literature[57, 58], Nonlinear Scattering Theory was developed as a frequency domain method. In Section 3.2, I showed that a similar method can be derived in the time domain, which is a novel method for performing NLST.

In this section, we will transform the formula for time domain Lorentz Reciprocity (Equation 3.2) into a numerical recipe for time-domain NLST.

Similarly to the frequency domain case, we consider $\vec{J}_2$ to exist over a small sphere of

volume $V = \Delta x \Delta y \Delta z$, and apply Riemann style integration to the volume integrals. These steps will not be shown as they are very similar to the previous section, with the exception of explicit dependence on time instead of frequency. We then obtain

$$\int_{-\infty}^{\infty} \vec{J}_{20}(t) \cdot \vec{E}_1(\vec{r}_D, \tau - t)\, dt = \sum_p \int_{-\infty}^{\infty} \vec{J}_1(\vec{r}_p, \tau - t) \cdot \vec{E}_2(\vec{r}_p, t)\, dt. \tag{3.24}$$

Next we look to the infinite bounds in the time integration. Before discretizing, we must define finite bounds. We start by noting that the currents and resulting fields are nonexistent prior to some time t_s, and for the simulation to be physical, must have decayed to nothing by the end of the simulation at time t_e. This solidifies that the integrands will vanish for any values of t beyond these bounds. We further simplify by denoting that the start time $t_s = 0$, defining $t \in [0, t_e]$.

Furthermore, the presence of $\tau - t$ enforces that $\tau - t \in [0, t_e]$. Since t will remain positive within its entire range, we need only consider when $t > \tau$ causing the difference to become negative and the integrand to again vanish. Thus, the true bounds of the integral are 0 and τ. The right-hand side of Equation 3.24 becomes

$$\sum_p \int_{-\infty}^{\infty} \vec{J}_1(\vec{r}_p, \tau - t) \cdot \vec{E}_2(\vec{r}_p, t)\, dt = \sum_p \int_0^{\tau} \vec{J}_1(\vec{r}_p, \tau - t) \cdot \vec{E}_2(\vec{r}_p, t)\, dt.$$

When replacing the time integration with something discrete, such as a Riemann style integral, it is important to define the number of times being summed over as it is different for each value of τ. If we define that there are N time steps between $t = 0$ and t_e, then the time step would be

$$\Delta t = \frac{t_e}{N}.$$

This would mean, for the range of time values from $t = 0$ to τ, there number of values to be summed over are

$$\frac{\tau - 0}{\Delta t} = N \frac{\tau}{t_e}.$$

Thus, with n as a placeholder index for time, the bounds for the discrete sum are $n \in \left[0, N\frac{\tau}{t_e}\right]$, with a constraint being that values of τ must be chosen on an equivalent gridding to the discrete time t_n to ensure that the upper bound of the sum remains an integer. Replacing our integral with this summation gives

$$\sum_p \int_0^\tau \vec{J}_1\left(\vec{r}_p, \tau - t\right) \cdot \vec{E}_2\left(\vec{r}_p, t\right) dt = \sum_{n=0}^{N\frac{\tau}{t_e}} \sum_p \vec{J}_1\left(\vec{r}_p, \tau - t_n\right) \cdot \vec{E}_2\left(\vec{r}_p, t_n\right) \Delta t.$$

For the left-hand side of Equation 3.24, there are several options available, utilizing both time and frequency domain methods. For the purposes of this project, the convolution on the left is avoided by moving to the frequency domain at this step, as we are primarily comparing the calculation speed, resulting spectra, and noise floor being achieved. Thus, the final step in this project continues to use the frequency domain secondary current, $\vec{J}_{20}(\omega)$, with the same uniform sphere formalism leading to Equation 3.21, solving for the nonlinear scattered spectra. Finally, we obtain

$$\vec{E}_1\left(\vec{r}_D, \omega\right) = \frac{1}{\vec{J}_{20}(\omega)} \mathcal{F}\left\{ \sum_{n=0}^{N\frac{\tau}{t_e}} \sum_p \vec{J}_1\left(\vec{r}_p, \tau - t_n\right) \cdot \vec{E}_2\left(\vec{r}_p, t_n\right) \Delta t \right\},$$

where $\mathcal{F}$ denotes a discrete Fourier transform. It is worth noting that it may be possible to avoid frequency domain altogether in this step if a sufficiently short (broadband) fictitious current source is used. Under these circumstances, the convolution could instead be approximated to give some scaled value of the field at time τ, similar to a delta function.

3.4 Different Approaches for the Nonlinear Current

There are three approaches that were developed, implemented, and tested in this project for Nonlinear Scattering Theory, which will be outlined in this section. Two of these approaches will make use of Lorentz Reciprocity in the frequency domain, whilst the remaining one will be the fully time domain approach. Ultimately, the goal is to find situations where certain approaches may break or become unstable, leading the user to favour another, as will be investigated in Chapter 4.

3.4.1 Frequency Method

This approach, dubbed the "frequency method" in this project, utilizes only our formulas that are in the frequency domain. Thus, the calculations only make use of frequency domain fields, and applies the double convolution formula shown in Equation 2.13 to calculate the nonlinear polarization.

After calculating this quantity as efficiently as possible for a given structure, it is transformed into the nonlinear current via multiplication by $-i\omega$ for use in NLST. The

other quantities $\vec{J}_2$ and $\vec{E}_2$ are directly used in the frequency domain for this calculation.

$$\vec{J}_1 = -i\omega\vec{P}_1$$

This method began as the sole comparison to the previously existing NLST, however, due to noise issues discovered and outlined in Section 4.1, there was a need for a more stable method to compare the novel time domain approach to the existing approach which utilises Lorentz Reciprocity in the frequency domain. For this reason, the Hybrid Method was introduced in the duration of the project.

3.4.2 Hybrid Method

This approach, dubbed the "Hybrid method" in this project, utilizes the formula for Lorentz Reciprocity in the frequency domain, however, monitors the linear driving field in the time domain. Upon discovering that the frequency method could occasionally give misleading results (covered in Section 4.1), this method was introduced as a replacement for the full frequency method. Since it still uses the Lorentz Reciprocity integration in the frequency domain, it becomes the method to compare time-domain NLST to the previously existing frequency domain version. It allows for a simpler calculation to determine the nonlinear polarization for our non-monochromatic source, avoiding the problematic double convolution in the frequency method. We consider for the polarization Equation 2.11 which considers an instantaneous local perturbative nonlinear third order response.

The linear field is monitored via time domain monitors in the simulation, which are then used in the formula to obtain the polarization as a function of time. From that point, the time domain polarization is moved into the frequency domain by means of a discrete Fourier transform (or DFT). Once in the frequency domain, the nonlinear polarization is transformed into the nonlinear current via multiplication by $-i\omega$. As with the frequency method, the other quantities $\vec{J}_2$ and $\vec{E}_2$ are directly used in the frequency domain for this calculation.

3.4.3 Time Method

This approach, dubbed the "time method" in this project, utilizes the formula for Lorentz Reciprocity in the time domain and the novel time domain approach to NLST. In this approach, the nonlinear polarization is calculated in the time domain using the same formula as is applied in the Hybrid method, given by Equation 2.11. From here, rather than using the frequency domain to perform the derivative, it is done so using finite differences, so the current is in the time domain for use in the time domain recipe, via

$$J_i\left(\vec{r},t\right) \approx \frac{P_i\left(\vec{r},t+\delta t\right) - P_i\left(\vec{r},t-\delta t\right)}{2\delta t}.$$

Chapter 4

Results and Discussion

In this section, I will apply the newly formulated time-domain NLST to a variety of test cases. The geometries will remain simple (thin films and nanospheres) while varying in size and material. A non-dispersive example will be silica glass, whereas for a dispersive example gold will be used. Ultimately, I will demonstrate the strong quantitative performance of NLST.

Simulation Methods

There are two approaches to generating the simulated dataset. The first approach uses a custom one-dimensional Finite-Difference Time-Domain (FDTD) solver written in Python by me, specifically for this project. This solver was created for the purpose of testing the performance of NLST using the existing frequency domain method, as well as the newly formulated time domain method. Since it was created specially for this project, it has the instantaneous $\chi^{(3)}$ nonlinear model as described in Section 2.1.2 implemented self-consistently in the solver. The second approach uses 3D FDTD simulations, where a thin gold film and a gold nanosphere are considered. For the thin film case, we utilise periodic boundary conditions to attempt to replicate and expand upon the 1D FDTD setup. For the nanosphere case, absorbing boundary conditions are used everywhere. The 3D FDTD solver that was used is our research group's comprehensive in-house electrodynamic solver. It is a general FDTD solver, and includes nonlinear optical responses written by others. I did, however, write pre- and post-processing scripts to use the 3D simulation results for NLST. Since both the 1D and 3D codes contain nonlinear optical responses self consistently, they can be used for validation of NLST by determining if or when the undepleted pump approximation may begin to fail.

The details on the one-dimensional solver being used for this portion of the project are provided in Appendix A, which includes a review of the update equations formulated for fully nonlinear simulations used for validating the results, as well as fully linear simulations

used to calculate the nonlinear generation via NLST.

The NLST spectra were determined in both reflection and transmission throughout the test cases. As explained in Section 3.1 and through Figure 3.4, the backward simulation source is placed at the detector point, and thus, if we move this backward simulation source, we also move the detection point. Figures 3.1-3.4 illustrate the case where we are measuring the spectra in transmission. Whereas, in order to determine the reflected spectra, the backward simulation source, and thus detector, is placed on the same side as the incident pump source.

To obtain the nonlinear scattered spectra from the direct nonlinear simulations, a separate, solely linear simulation was performed in the same simulation domain. The fields from the linear simulation were then subtracted from that of the nonlinear simulation at the detector point, isolating the effect of the nonlinear processes. In all figures in this chapter, the flat-lining present in the validation spectra is due to the noise floor of the simulated results.

Defining Success for NLST

Since we would ultimately like to apply NLST in obtaining initial optimizations for inverse design problems, the level of agreement which is sought after has room for some error. Since early optimization steps often have very large variations in the overall function being minimized/maximized for each step, a good level of agreement in magnitude would be considered less than 10%, with approximately 5% or less being exceptional. The phase agreement of NLST results had yet to be explored before this project, despite the theory indicating it should be possible. Phase is not of notable importance for the example case of third harmonic generation, thus reasonable agreement would be defined within a broader range of within $\pi/2$ or approximately 1.57 radians, with values closer to zero being preferable.

4.1 1D FDTD for a Thin Film of Fused Silica

The first test cases covered are for a non-dispersive dielectric with the parameters for silica glass, using the 1D FDTD code written by me for the required linear forward and backward simulations for NLST, as well as the corresponding self-consistent nonlinear simulations for validation. A thin slab of fused silica was simulated with a fixed value for the linear and nonlinear susceptibilities using parameters outlined below in Table 4.1. The first order linear susceptibility for silica glass at 1064nm (the pump center wavelength) was taken from reference [73], and the corresponding third order nonlinear susceptibility was taken from reference [23].

Parameter	Value(s)
Silica $\chi^{(1)}$	1.1609
Silica $\chi^{(3)}$	$2.5 \times 10^{-22} \frac{m^2}{V^2}$
Domain Cell Size $(\Delta x, \Delta y, \Delta z)$	1nm
Simulation Time Step (Δt)	$\frac{\Delta y}{c_0}$
Pump Wavelength	1064nm
Pump Duration (FWHM)	25fs, 100fs
Film Thickness	25nm, 355nm

Table 4.1: **1D FDTD Simulation and Material Parameters for THG in a Thin Silica Film**

Two sets of nonlinear scattered spectra were measured, one with the detector point r_D located on the opposite side as the source (we call this measuring the far field in transmission), and one with r_D located at the same side as the source (measuring in reflection).

Using both the time and frequency NLST methods outlined in Section 3.4, the resulting NLST spectra, as well as the validation spectra calculated by direct nonlinear simulations (also 1-dimensional), are shown in Figures 4.1 and 4.2.

In Figures 4.1 and 4.2 we plot the transmitted and reflected spectra, respectively, of this initial test case of a 25nm silica film illuminated by a 25fs pulse centered at 1064nm. On the left and right side of each figure, the dashed lines are the result of the NLST time and frequency methods, respectively. Alongside each of these are solid lines showing the resulting spectra for a direct nonlinear simulation for validation. The top row of each figure shows the real and imaginary parts of the spectra around the third harmonic, as calculated via NLST and a direct nonlinear simulation. The bottom row of each figure shows the absolute value of the NLST and validation spectra with $\log_{10}$ scaling, where the flat line in the validation spectra is the noise floor of the simulated validation spectra.

On the left-hand sides of Figures 4.1 and 4.2, we see that the agreement between the novel time-domain NLST results and the direct nonlinear simulation results is exceptional with relative deviation in magnitudes of 0.78% and 0.81% in reflection and transmission, respectively. This validates the ability of the NSLT approach to obtain quantitative results. On the right-hand sides of Figures 4.1 and 4.2, the same system is shown, but the frequency method NLST is used instead. Again, the NSLT results agree remarkably well with the direct nonlinear simulations with relative deviation in amplitudes being 0.61% and 1.36% in reflection and transmission respectively. Overall, strong quantitative results well below the earlier defined 5% ideal are demonstrated to be achievable.

The phase results in both methods demonstrate that the phase of the nonlinear signal determined through NLST agrees very well with that of validation spectra. For the time

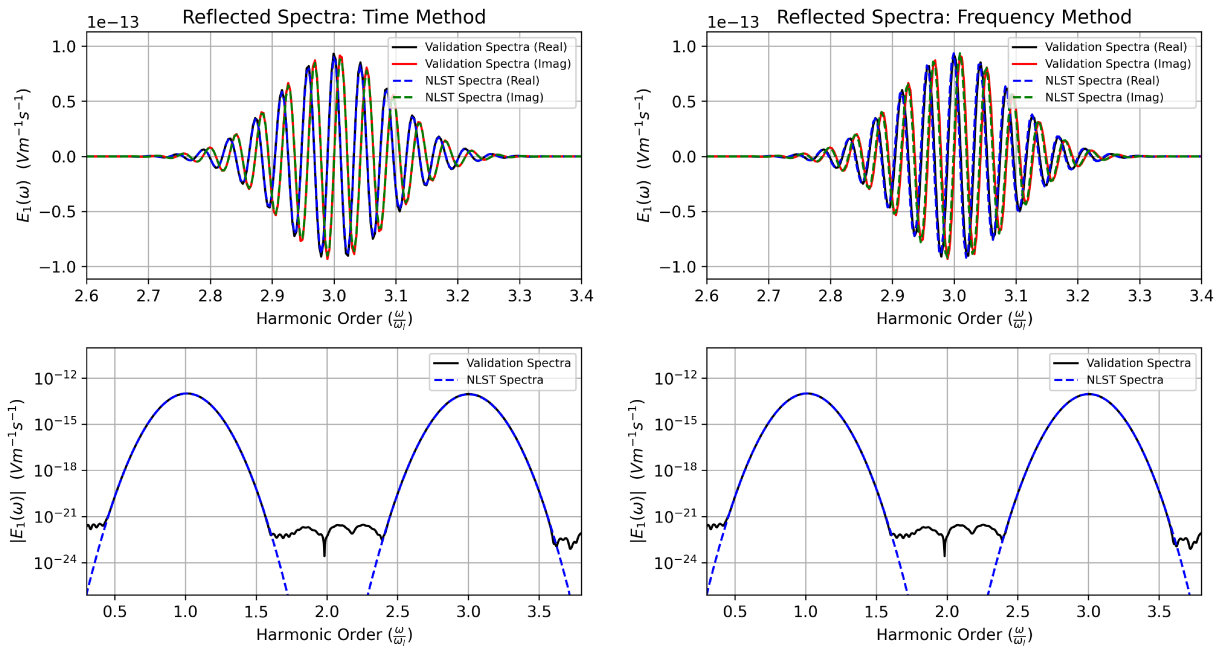

Figure 4.1: **NLST Reflected Spectra – 25nm Silica Film and 25fs Pulse**
(Left) Time and (Right) frequency method.
(Top) Real/Imaginary parts and (Bottom) absolute value.

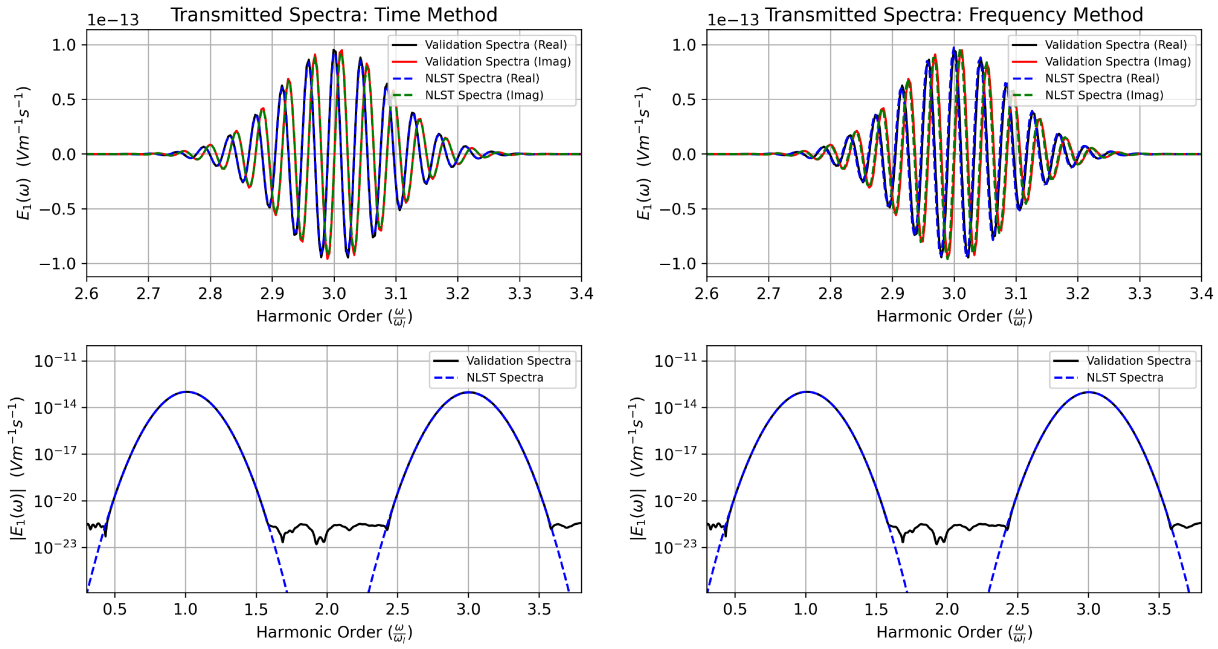

Figure 4.2: **NLST Transmitted Spectra – 25nm Silica Film and 25fs Pulse**
(Left) Time and (Right) frequency method.
(Top) Real/Imaginary parts and (Bottom) absolute value.

method, the difference in phase between the NLST and validation are below the frequency resolution of 0.06 radians, in both reflection and transmission. For the frequency domain approach, the variation is 0.39 radians in both transmission and reflection.

Not only do the results align well in value and phase between the NLST calculation and the validation simulation, but we also see expected results in regard to the overall spectral profile with equivalent magnitude in reflection and transmission. Since silica is a material without significant losses in the wavelength regime being considered, the third harmonic light is being generated at the same intensity across the whole film and propagating uniformly outward. Furthermore, the film is thin compared to the wavelength so both forward and backward third harmonic signals are phase matched. Thus, we would expect the reflected and transmitted spectra to be equal in magnitude, and this is indeed what we see when comparing Figures 4.1 and 4.2. This is seen in the NLST calculated results as well as the validation simulation.

This strength in agreement for both methods remains true as the film length increases. To illustrate this, the driving pulse was fixed at 25fs and the length of the film was increased to 355nm, where results for both the time and frequency method are shown in Figure 4.3 (reflection spectra) and Figure 4.4 (transmission spectra). The layout of the plots is identical the the example prior, with the results for time method NLST displayed on the left, and frequency method NLST on the right.

Similarly to the 25nm film, the NLST estimated spectra from a 355nm thin film illuminated by a 25fs driving source agrees very well with that of the self-consistent validation simulation. In reflection and transmission, the magnitudes vary by 0.94% and 0.85% respectively for the time method, whereas for the frequency approach we see slightly higher values at 2.51% and 1.77% respectively. In Figures 4.3 and 4.4, we see that for both the reflected and transmitted spectra, the results continue to be in phase for both the time and frequency method NLST. For the time method, we see a phase difference below the resolution of 0.06 radians in both reflection and transmission, whereas the frequency domain displays a slightly larger phase difference at 0.09 radians in both reflection and transmission.

For the 355nm thin film, very minor distortions on the low-frequency side of the third harmonic can be seen near the peak for both methods around the third harmonic frequency, due to thin film interference effects starting to be introduced, given that the film is the same length as third harmonic peak wavelength. These minor distortions are present in the NLST spectra for each method, demonstrating how NLST is capable of capturing these physical effects. Overall, the results remain almost equally strong while both the frequency and time domain method continue to be indistinguishable from each other.

While they both perform very strongly and well within our goal ranges for varying film

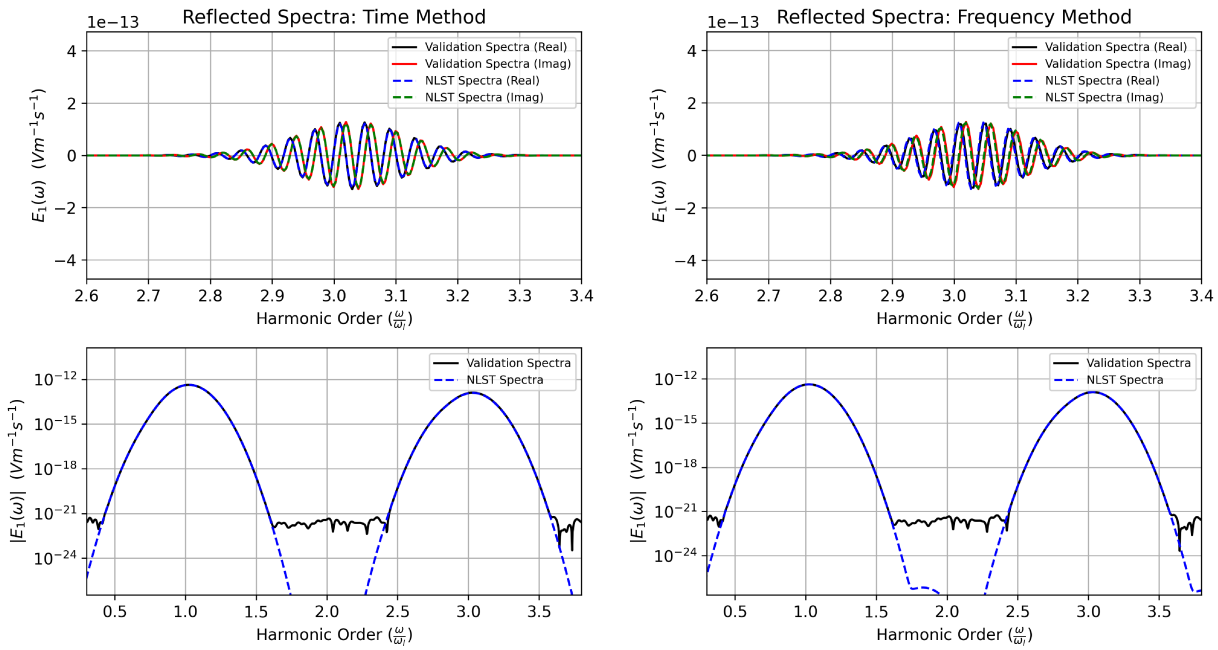

Figure 4.3: **NLST Reflected Spectra – 355nm Silica Film and 25fs Pulse**
(Left) Time and (Right) frequency method.
(Top) Real/Imaginary parts and (Bottom) absolute value.

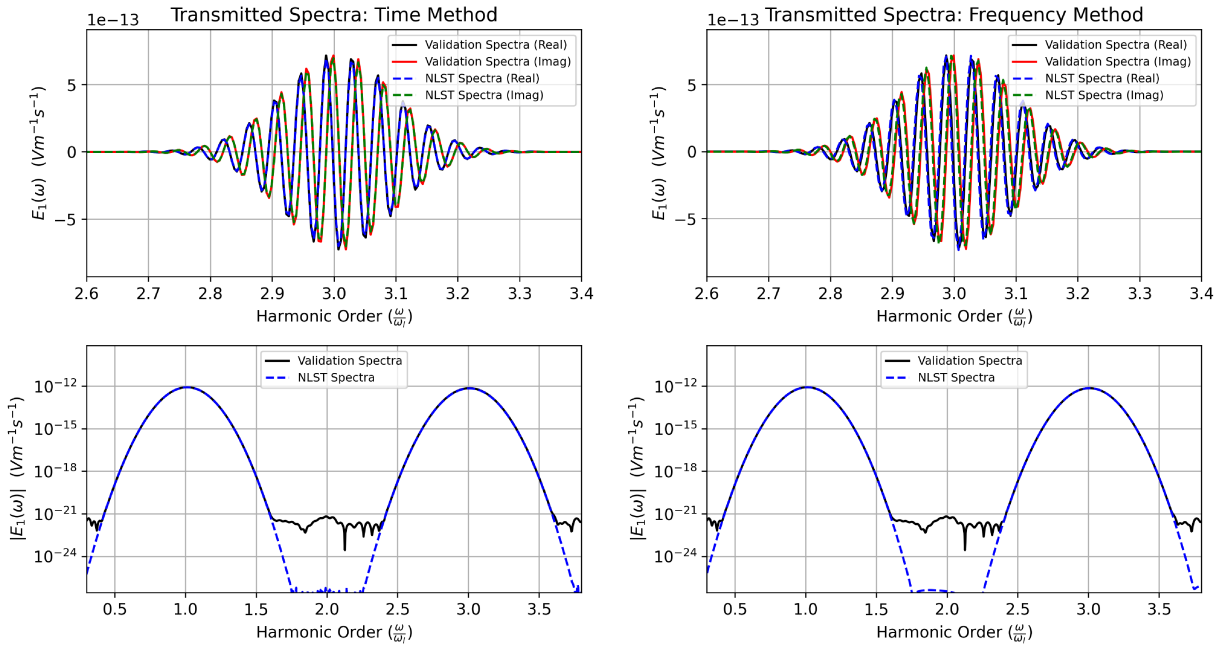

Figure 4.4: **NLST Transmitted Spectra – 355nm Silica Film and 25fs Pulse**
(Left) Time and (Right) frequency method.
(Top) Real/Imaginary parts and (Bottom) absolute value.

lengths, issues sometimes appear when the noise floor becomes more present in the total spectral picture as the pulse duration is extended. One documented example of this was when I simulated the 25nm film but extended the pulse duration to 100fs.

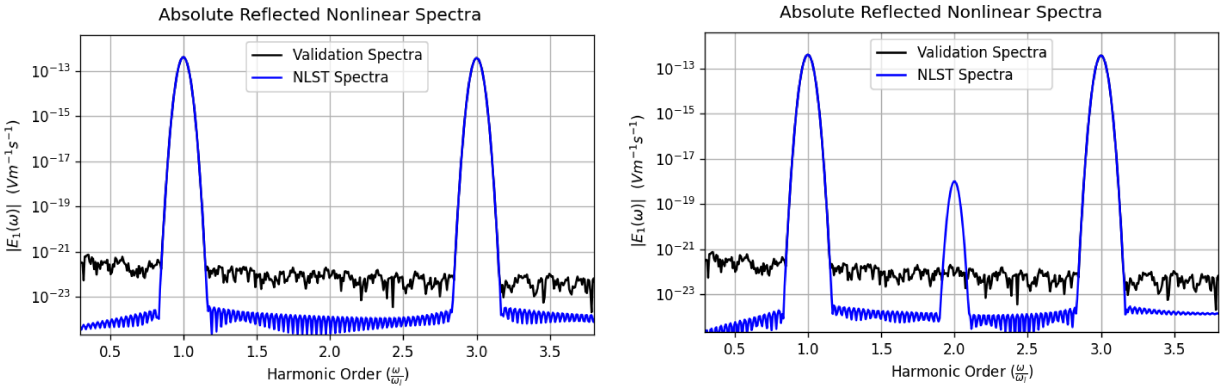

Figure 4.5: **NLST Reflected Spectra – 25nm Silica Film and 100fs Pulse**
(Left) Time method. (Right) Frequency method.

Figure 4.5 shows the reflected spectra for a 25nm thin film illuminated by a 100fs pulse centered at 1064nm. Though each method gives strongly similar results at the fundamental and third harmonic, there is a non-physical second harmonic component in the frequency method. This peak occurs because the frequency method requires us to perform a double convolution integral over frequency. Within this integral are terms where there is the field squared at peak value (near the first harmonic) which multiplies the field at minimum value, given by the noise floor near zero frequency. This causes the noise floor to be increased at the second harmonic. It is not a real signal. In fact, we know this second harmonic component is numerical in origin, as it is dependent on the noise floor, which can vary between simulations. This variation can lead to it sometimes appearing differently, or not appearing at all. The double convolution integration over the entire spectra ultimately includes the spectral noise floor, and when the spectral peaks come across any artifacts, they can sometimes amplify them, leading to the non-physical results. It is possible to avoid or remove these through extra processing, such as forcing down the magnitude of noise floor of the data, and/or smoothing it prior to the double convolution.

Figure 4.6 shows that the second harmonic signal was a numerical artifact resulting from noise. By taking an upper bound of the noise floor of the linear electric field, and multiplying against a much smaller number to shrink it considerably, the values that are created by the noise are forced down by many orders of magnitude. Here, we see that when this is done, the second harmonic artifact is also forced down in magnitude, as it is a result of the noise. This demonstrates both that the extra signal is related to this floor, as well as can

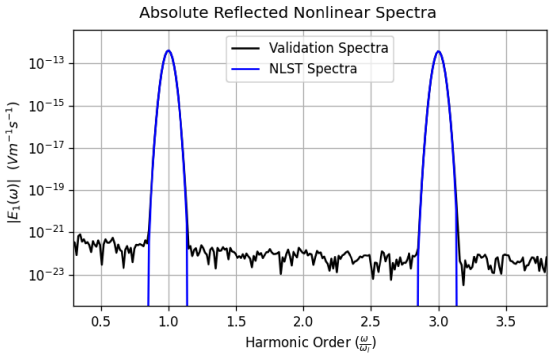

Figure 4.6: **Noise-Corrected Frequency Method NLST Reflected Spectra – 25nm Silica Film and 100fs Pulse**

be avoided through adjustments or filtering. This added manipulation is successfully giving better results, while creating an unnatural drop-off in the frequency profile, albeit many orders of magnitude below the peak. To avoid the need for extra processing in general, the frequency domain method is best suited to either (1) monochromatic sources where you avoid the convolution by applying Equation 2.14, or (2) broadband simulations where the spectral data does not include the noise floor.

Due to its problem with such artifacts, we no longer use the frequency method from this point on in this thesis. The material response is not required to be calculated in the frequency domain for use in the frequency domain Lorentz Reciprocity integration on which the existing NLST is based upon. Thus, we replace the frequency domain approach with the hybrid approach, which has many of the advantages of the frequency domain approach but avoids the double convolution. Figures 4.7 and 4.8 show the reflected and transmitted spectra, respectively, of a 25nm silica film illuminated by a 100fs pulse centered at 1064nm, using time and hybrid method NLST. The layout of the plots is similar to Figures 4.1/4.2 and Figures 4.3/4.4, with the results for time method NLST displayed on the left, and now the results for hybrid method NLST displayed on the right.

It can be seen in the absolute spectra of both Figures 4.7 and 4.8 that the hybrid method does not demonstrate the same issues regarding non-physical artifacts in the non-linear spectra. Overall, we see the same strong agreement between both NLST methods and the validation spectra with below 1% difference in magnitude, and less than 0.06 radian phase difference for both methods in either reflection or transmission.

Benchmarking the Runtime for NLST

For these early test cases, the difference in runtime for the linear simulations and the validation nonlinear simulation were closely measured during their runtime in Python. As

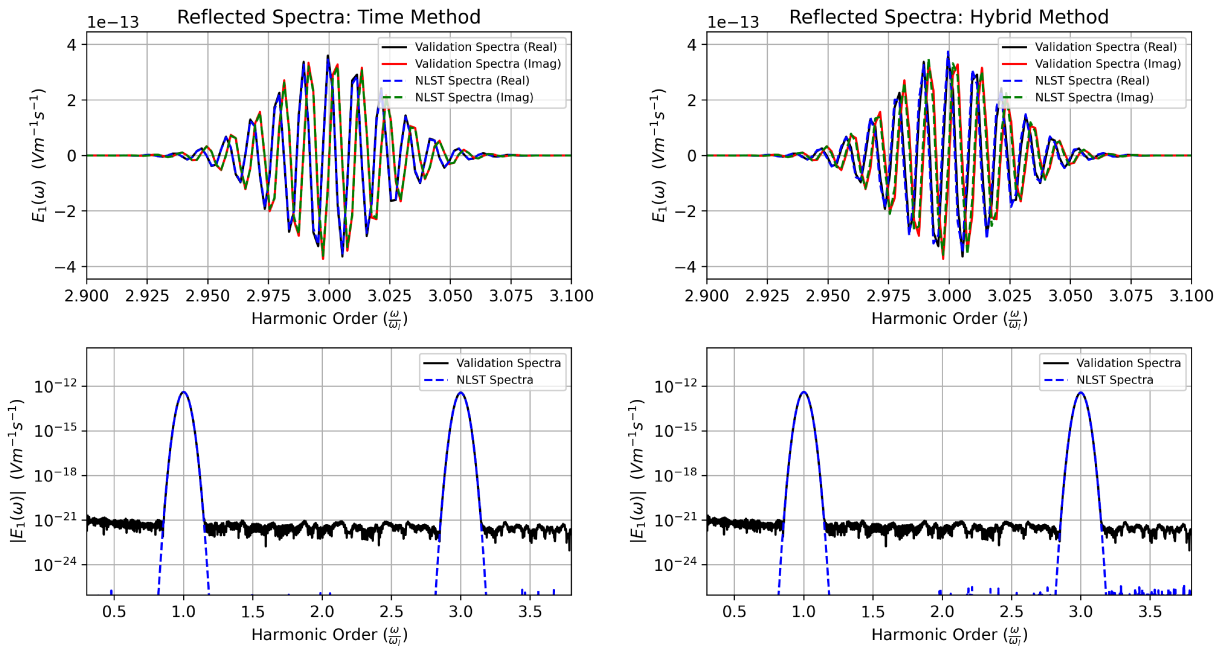

Figure 4.7: **NLST Reflected Spectra – 25nm Silica Film and 100fs Pulse**
(Left) Time and (Right) hybrid method.
(Top) Real/Imaginary parts and (Bottom) absolute value.

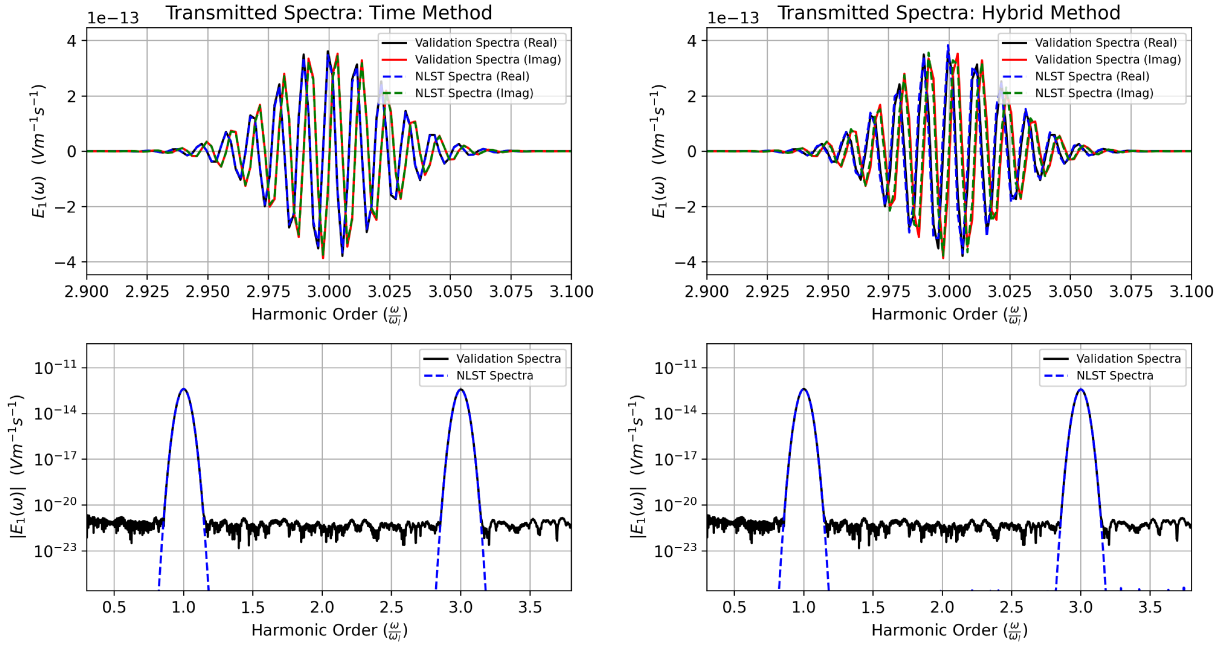

Figure 4.8: **NLST Transmitted Spectra – 25nm Silica Film and 100fs Pulse**
(Left) Time and (Right) hybrid method.
(Top) Real/Imaginary parts and (Bottom) absolute value.

expected, these linear simulations were significantly faster to perform than a single nonlinear simulation, lending strength to the applicability of NLST as a faster alternative to direct nonlinear simulations when viable.

For the silica glass test simulations, the nonlinear simulations took between 28 and 168 times longer to run than the two linear simulations required for NLST (with an average of about 99 times longer).

However, not included in these times above was the post-processing NLST calculation time, which can be significant. For the frequency method in particular, with the double convolution over the entire spectral range shown in Figures 4.1-4.8, the spectra took 2.4 times longer to determine than it would have through direct nonlinear simulation. The time and hybrid approaches, however, were more comparable, requiring approximately the same amount of time as the direct nonlinear simulation.

The NLST calculations were performed in Python, however, and not fully optimised leaving notable room for improvements in the speed of their computation. This suggests that in all cases, faster speeds should be achievable, and nonlinear results can be estimated faster through NLST and they could be obtained through direct nonlinear simulation.

4.2 1D FDTD for a Thin Film of Gold

To test, compare, and contrast the various NLST methods on a material with both losses and dispersion, a thin film with the parameters of gold was used. The gold film was simulated using a Drude-Lorentz model for the linear optical response, using the numerical steps outlined in Appendix A.3. The linear model parameters were obtained by fitting refractive index data for gold to a Drude-Lorentz model. The instantaneous $\chi^{(3)}$ tensor nonlinear response was taken from reference [23]. Though the value of $\chi^{(3)}$ being used was measured for a wavelength of 1064nm, the Drude-Lorentz model being implemented for validation requires wavelengths greater than this (above 550nm) to maintain an accurate linear response for gold at the third harmonic wavelength. For this reason, the pump wavelength was increased slightly to 1800nm, without any loss of applicability since the nonlinear response is still being simulated identically to how it is calculated in NLST. The simulation parameters are outlined in Table 4.2.

Parameter	Value(s)
Gold $\chi^{(3)}$	$7.599 \times 10^{-19} \frac{m^2}{V^2}$
Domain Cell Size $(\Delta x, \Delta y, \Delta z)$	1nm
Simulation Time Step (Δt)	$\frac{\Delta y}{2c_0}$
Pump Wavelength	1800nm
Pump Duration (FWHM)	25fs, 100fs
Film Thickness	50nm, 600nm

Table 4.2: **1D FDTD Simulation and Material Parameters for THG in a Thin Gold Film**

In Figures 4.9 and 4.10 we plot the reflected and transmitted spectra, respectively, of a 50nm gold film illuminated by a 25fs pulse centered at 1800nm. On the left- and right-hand side of each figure, the dashed lines continue to be the results of time and hybrid method NLST, respectively. Alongside each of these are solid lines showing the resulting spectra for a direct nonlinear simulation for validation. The top row of each figure shows the real and imaginary parts of the spectra around the third harmonic, as calculated via NLST and a direct nonlinear simulation.

The absolute spectra for both time and hybrid method NLST continue to agree very strongly in Figures 4.9 and 4.10. Quantitatively speaking, the time method has a relative deviation of 6% and 9% in reflection and transmission, respectively, both below the 10% goal threshold. The hybrid method exhibits a very similar deviation of 6% and 10% in reflection and transmission, respectively. Around the fundamental, there are very minor differences present, likely due to the nonlinear effect on the linear response in the direct nonlinear simulations. Further, the peak frequencies near the fundamental and third harmonic frequencies are slightly blueshifted, however, this effect is not very strong. The slightly differing peak frequencies between the spectra likely arises from a sensitivity of the model to the carrier envelope phase at such short pulse durations, as it is not present for longer pulses which were tested in the cases that follow.

The phase agreement around the third harmonic in reflection and transmission are shown in the top rows of Figures 4.9 and 4.10, and are are also very strong. Both methods are below the distinguishable limit of 0.06 radians with regard to phase difference in both reflection and transmission. This demonstrates that the signal can still be propagated quantitatively to the detector point for a lossy and dispersive material via time or hybrid method NLST.

When examining the linear scales on the top portion of Figures 4.9 and 4.10, it is also important to note that the reflected spectra is greater than the transmitted by a factor of approximately 2. This makes sense, as the majority of the nonlinear generation takes place

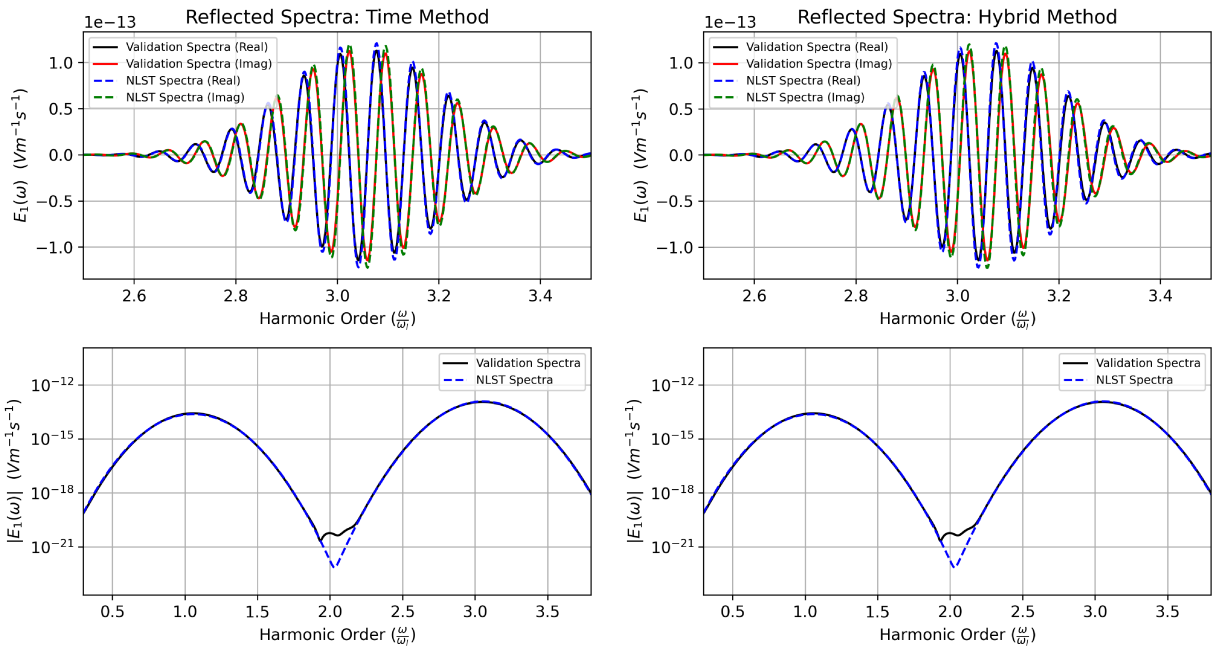

Figure 4.9: **NLST Reflected Spectra – 50nm Gold Film and 25fs Pulse**
(Left) Time and (Right) hybrid method.
(Top) Real/Imaginary parts and (Bottom) absolute value.

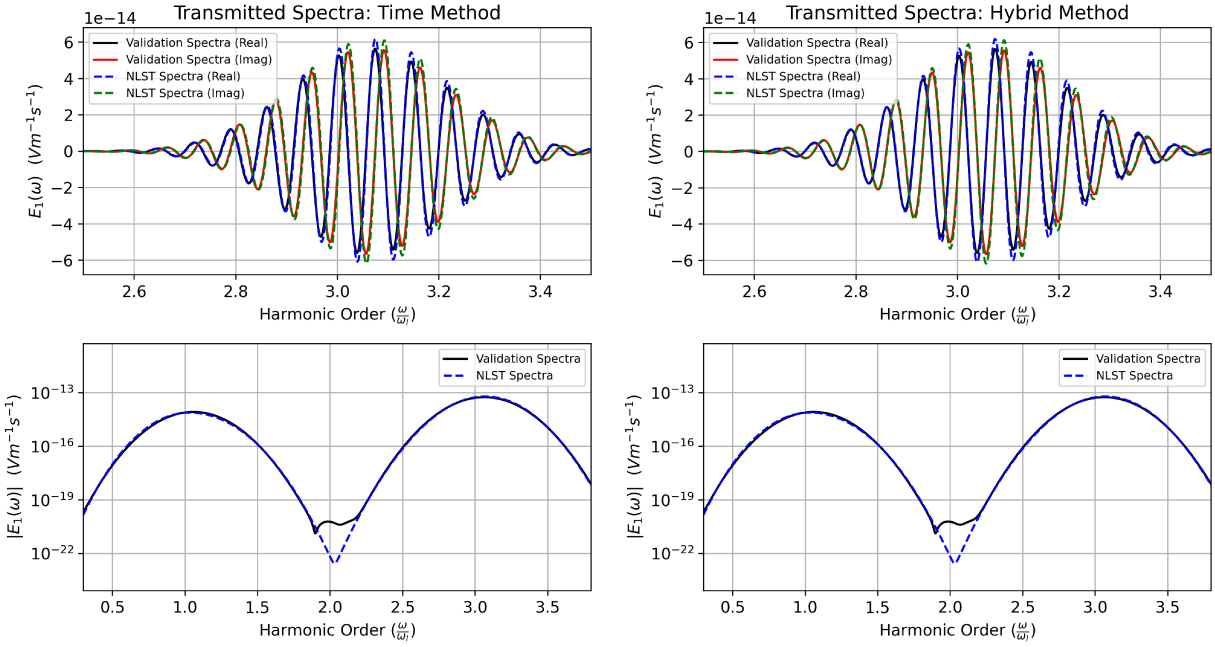

Figure 4.10: **NLST Transmitted Spectra – 50nm Gold Film and 25fs Pulse**
(Left) Time and (Right) hybrid method.
(Top) Real/Imaginary parts and (Bottom) absolute value.

at a very shallow depth in the thin film, and has significantly less distance to propagate to leave the gold film and make its way to the reflected detection point than to the transmission detection point. In order for light to reach the transmission detection point, it must propagate from the point it was generated, through the rest of the film, and leave the media. This extra propagation through the gold is allowing for more absorption to occur, resulting in spectra which is smaller in magnitude in transmission than in reflection.

When examining the transmitted spectra for a much thicker film, a scenario where NLST out-performs the direct nonlinear validation is found. In Figure 4.11, the transmitted spectra of a 355nm gold film illuminated by a 25fs pulse centered at 1800nm is shown. On the left and right hand side of the figure, the time method and hybrid method NLST spectra, respectively, are shown with dashed lines.

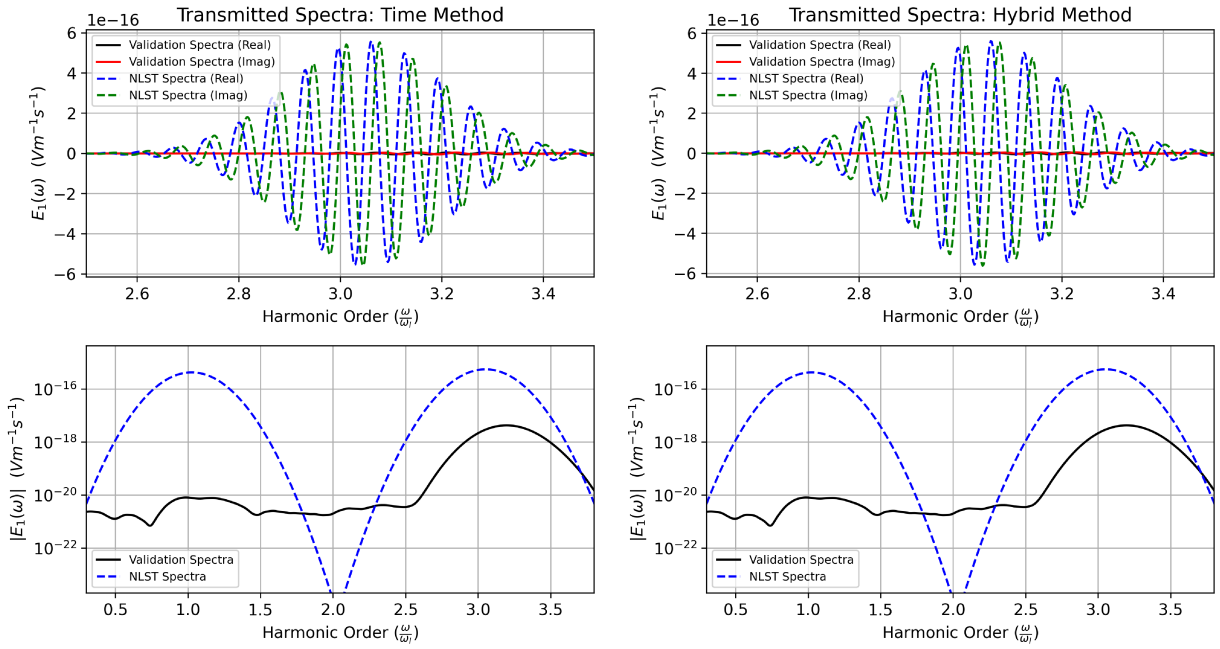

Figure 4.11: **NLST Transmitted Spectra – 355nm Gold Film and 25fs Pulse**
(Left) Time and (Right) hybrid method.
(Top) Real/Imaginary parts and (Bottom) absolute value.

In transmission from the 355nm gold film in Figure 4.11, it can be seen that the validation spectra differ immensely from the estimated spectra determined through both methods of NLST. In this case, I believe the fault lies in the validation simulation. It is likely that the validation simulation is beginning to fail because so much nonlinear signal is being lost as it propagates through the material. The nonlinear signal at the third harmonic is many orders of magnitude smaller than the linear signal, and becomes negligibly small after propagating through the lossy region. In FDTD, the time domain signal is kept and

propagated, this means that the nonlinear signal and linear signal are added together, and it can happen that the nonlinear signal is so small compared to the linear it is beyond the precision limit of the simulation. Ultimately, this causes the validation spectra to be wrong. What Figure 4.11 demonstrates, however, is that NLST (either the time or hybrid method) is capable of providing results in a situation in which direct nonlinear simulation can fail, like for very high-loss materials, or high noise floor simulations.

As the final example in this section, we return to the 50nm gold film and use a more narrow-band source with 100fs duration to examine the harmonic generation in reflection and transmission. Figures 4.12 and 4.13 show the reflected and transmitted spectra, respectively, of a 50nm gold film illuminated by a 100fs pulse centered at 1800nm, using time and hybrid method NLST. The layout of the plots is similar to other examples above, with the results for time method NLST displayed on the left, and the results for hybrid method NLST displayed on the right.

The absolute spectra shown at the bottom of Figures 4.9 and 4.10, have strong quantitative agreement with the self-consistent validation spectra shown by the solid line. Though not visible in the log scale, the linear scale of the upper half of the figure shows that NLST continues to account for losses in the gold as the transmitted spectra is less than the reflected by a factor of approximately two. In this test case, the relative deviation in magnitude is approximately 6% for each case, with identical non-resolvable phase differences as in the previous test case. Overall, the performance difference between the time and hybrid method NLST is not notable.

4.3 3D FDTD for a Thin Film of Gold

In the 1-dimensional FDTD tests, a specialized simulation script was created and used, where the nonlinear model in the validation simulation was identical to that chosen for calculating NLST. This allowed for a direct comparison between a perfectly equivalent nonlinear simulation. However, the instantaneous constant $\chi^{(3)}$ response captures only the third order response, and is not the only available way to model the nonlinear response of gold. In this section, we move to using an in-house 3-dimensional FDTD solver, that allows for comparison to multiple different validation simulations.

In the following test cases, two direct nonlinear simulations will be used: (i) one that implements the same instantaneous constant $\chi^{(3)}$ as is used for the NLST calculation, and (ii) another based on the hydrodynamic model described in Section 2.1.3. The instantaneous $\chi^{(3)}$ model is used to validate the NLST results, whereas the hydrodynamic simulations are a relative benchmark on the performance of the tensorial implementation. Being a peer

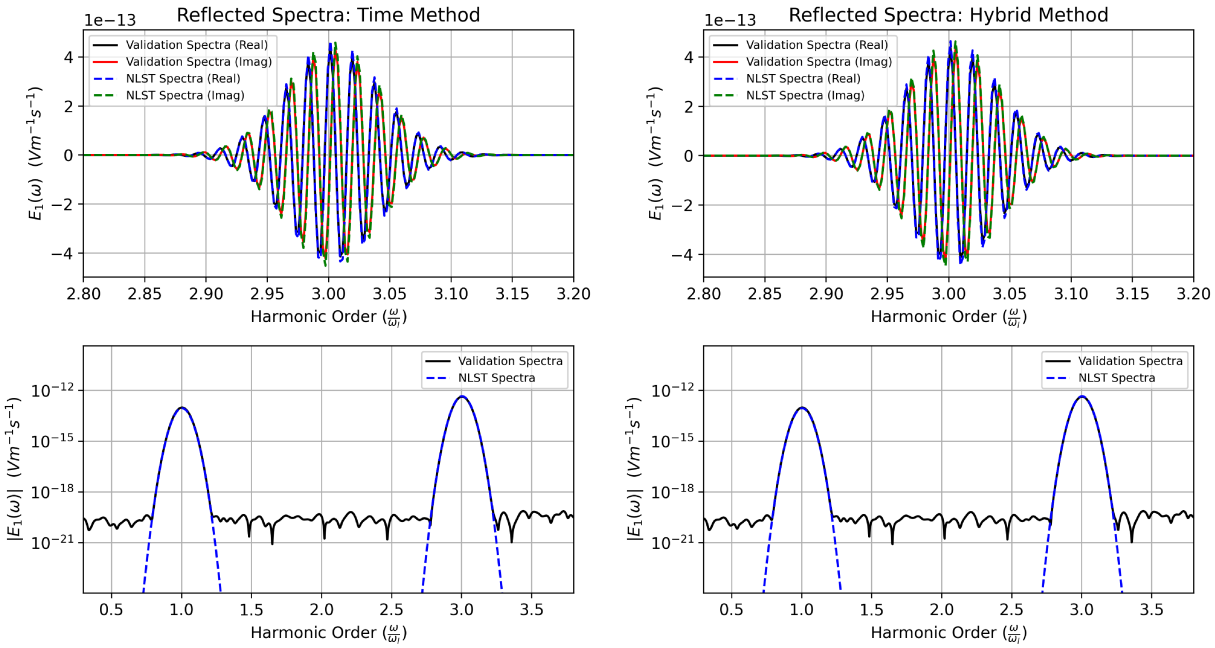

Figure 4.12: **NLST Reflected Spectra – 50nm Gold Film and 100fs Pulse**
(Left) Time and (Right) hybrid method.
(Top) Real/Imaginary parts and (Bottom) absolute value.

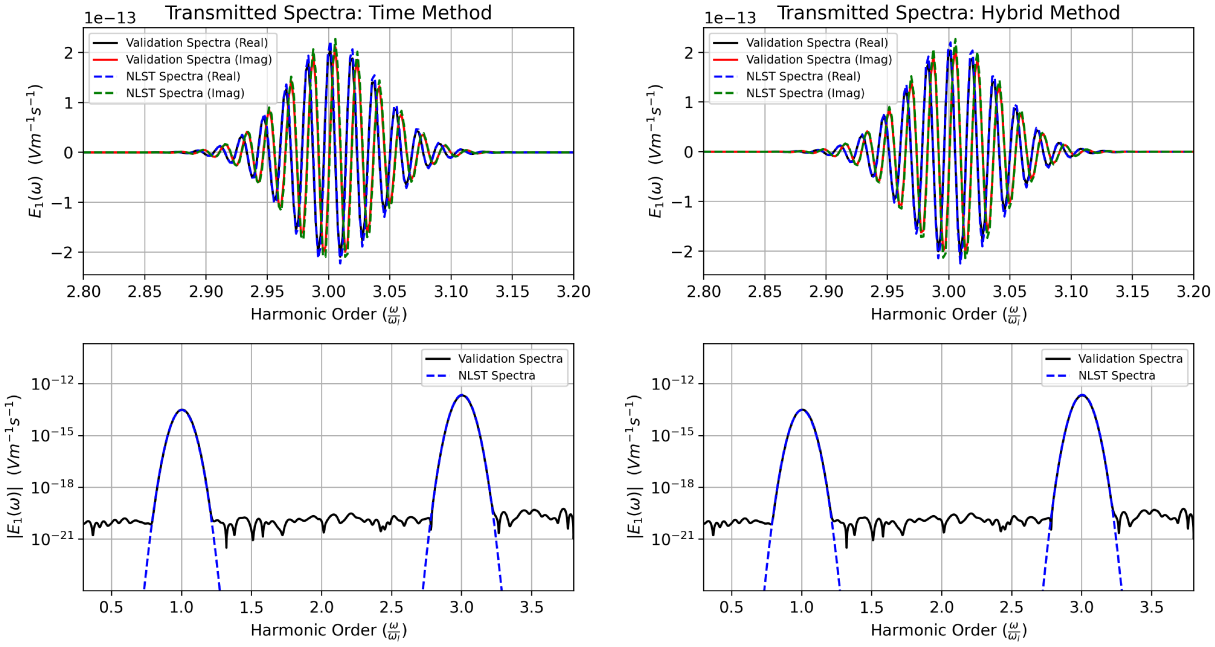

Figure 4.13: **NLST Transmitted Spectra – 50nm Gold Film and 100fs Pulse**
(Left) Time and (Right) hybrid method.
(Top) Real/Imaginary parts and (Bottom) absolute value.

reviewed and published model that is more robust, the hydrodynamic simulations can be used as an indicator of whether the nonlinear generation predicted by the instantaneous tensor model has a reasonable magnitude, or is not fully capturing enough physical mechanisms of the system. For the validation simulation using the third-order instantaneous response $\chi^{(3)}$, a preliminary implementation of a fully self-consistent tensor model was used that is currently in development by collaborators[74]. With the model still in development, a constant phase difference of π was needed to be added to the validation spectra in order to obtain agreement with the NLST method. This phase correction is fixed and unchanging for each test case. As we had achieved perfect agreement when exactly the same model was used in Sections 4.1 and 4.2, we attribute this phase factor to the details of the model implemented by our collaborator. The hydrodynamic model, unlike the third-order instantaneous $\chi^{(3)}$ response captures more than just the third order nonlinear processes, allowing it to display a more complete spectral profile that, as we will see, also includes second harmonic generation.

As the differing effects in reflection and transmission have been thoroughly demonstrated in Sections 4.1 and 4.2, this section will instead analyze only the reflected spectra. With absorption being strong in this wavelength regime, this allows us to obtain the strongest signals, well above the noise floors of the simulation.

The gold film in the 3D-FDTD was simulated using a Drude with 2 Critical Points model [63] for the linear response, which, unlike the previously used Drude-Lorentz model in Section 4.2, can successfully capture the dispersive behavior of gold in the wavelength regime that the value of $\chi^{(3)}$ was originally measured at 1064nm. Due to this, we will now return to a 1064nm driving signal. As well, a tensor form of the third order nonlinear susceptibility with symmetry class $m3m$ will be used in place of the previously used constant and singular value, both in the direct nonlinear simulation, as well as in the implementation of the NLST formulas. The full finite-difference time-domain simulation parameters used to generate the results in this section are tabulated in Table 4.3.

Parameter	**Value(s)**
Gold Model	Drude + 2 Critical Points
$\chi^{(3)}$ - Class $m3m$	$\chi^{(3)}_{xxxx} = 7.599 \times 10^{-19} \frac{m^2}{V^2}$
Domain Cell Size $(\Delta x, \Delta y, \Delta z)$	1nm
Simulation Time Step (Δt)	$\frac{\Delta y}{2c_0}$
Pump Wavelength	1064nm
Pump Duration (FWHM)	25fs, 100fs
Film Thickness	50nm, 355nm

Table 4.3: **3D FDTD Simulation and Material Parameters for THG in a Thin Gold Film**

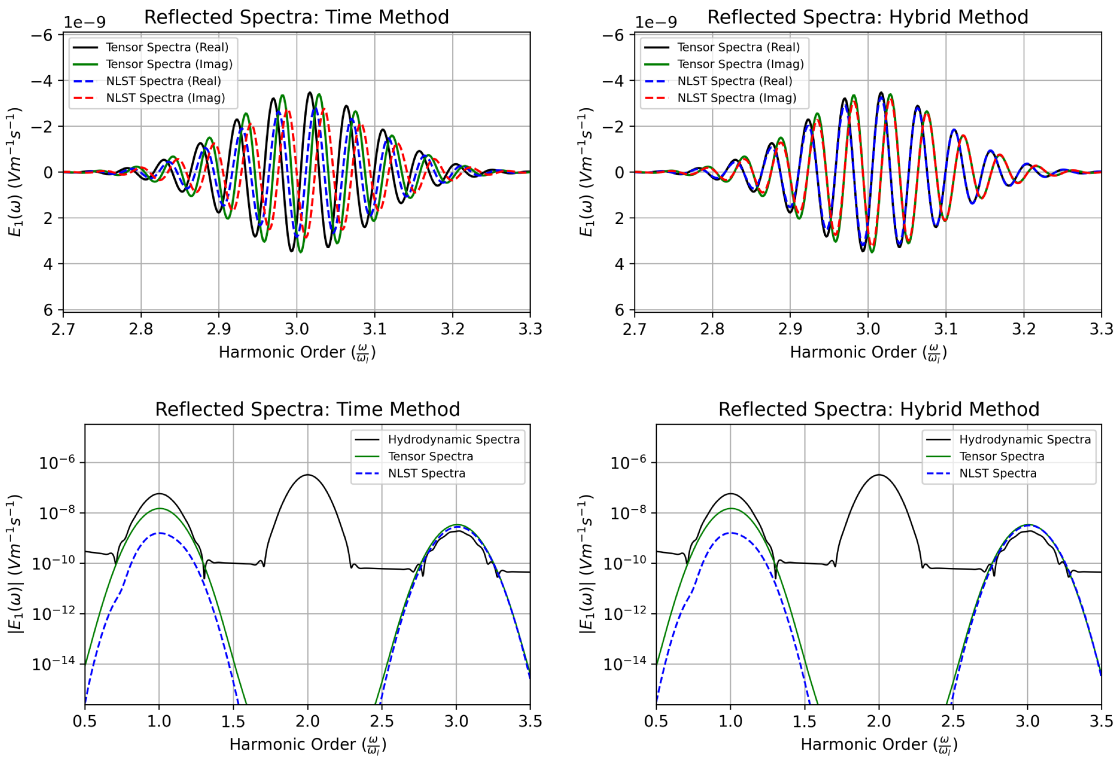

Figure 4.14: **NLST Reflected Spectra – 50nm Gold Film and 25fs Pulse**
(Left) Time and (Right) hybrid method spectra.
(Top) Tensor validation real/imaginary parts. (Bottom) Absolute fields.

In Figure 4.14, we plot the reflected spectra of a 50nm gold film illuminated by a 25fs pulse centered at 1064nm. On the left- and right-hand side of each figure, are the results of time and hybrid method NLST. The top row shows the real and imaginary parts of the spectra around the third harmonic, as calculated via NLST (dashed lines) for the tensorial model, in solid lines. The bottom row shows the absolute nonlinear spectra for NLST with a dashed line on a log scale, with solid lines showing the resulting spectra for two direct nonlinear simulation for validations: the hydrodynamic model (black), and instantaneous response $\chi^{(3)}$ (green).

First examining the absolute spectra on the bottom row of Figure 4.14, we note that the hydrodynamic validation results display second harmonic generation. Despite gold being centro-symmetric, which implies that it cannot generate even order harmonics within the bulk, second harmonic generation is still occurring as this symmetry is broken at the boundaries of the film. As mentioned above, the hydrodynamic model is capable of modeling this second harmonic generation enabling its appearance in the validation spectra. However, this second harmonic spectrum is not present in both the NLST spectra and direct tenso-

rial $\chi^{(3)}$ nonlinear validation spectra, as the instantaneous tensor $\chi^{(3)}$ model employed for both includes only third order nonlinear processes. Ultimately, this may act as a source of discrepancy between the two validation simulations, as the generation of light at the second harmonic will result in some depletion of the driving signal for the hydrodynamic model.

There are varying levels of strong agreement between the novel time domain NLST, hybrid method NLST, and the direct nonlinear simulation results, however, only at the third harmonic. At the third harmonic frequency, the peaks of the NLST and tensor spectra are slightly blue-shifted compared to the hydrodynamic validation, however, this effect is not very strong. Similar to the 1-dimensional thin film case, the slightly differing peak frequencies between the spectra likely arises from a sensitivity of the model to the carrier envelope phase at such short pulse duration, as it is not present for the more narrow-band pulses that were tested in the cases that follow. The difference in magnitude between the validation tensor model and NLST is at the third harmonic is 18% and 8% for the time and hybrid methods, respectively. Though the time-domain approach did not land within the goal range of magnitudes, its agreement for an estimative approach is still notable as it is within the same order of magnitude.

The difference between the spectra for the NLST and the two direct nonlinear simulations at the pump frequency is approximately one and two orders of magnitude for the tensorial and hydrodynamic simulations, respectively. This deviation can be attributed to differences in the linear response that arise due to the presence of the nonlinearity. Within the software, the nonlinear versions of materials are treated as an entirely different material response with a minor level of interconnectedness of the linear and nonlinear fields, meaning that an identical linear response is not quite possible to obtain. The spectra near the fundamental are the result of the difference between linear and nonlinear simulations, as the actual signal at the fundamental is many orders of magnitude larger, meaning that a change in reflectance at the pump frequency in the nonlinear material model is only 0.00005. Though this is very small, it has a large effect on the residual nonlinear spectrum at the fundamental due to the great magnitude of pump fields to obtain the nonlinear result.

Last, we compare the resulting phases in the top and middle rows of Figure 4.14 to reveal whether or not nonlinear scattering theory continues to propagate the signal to the detector point correctly. For the novel time method NLST on the left-hand side of Figure 4.14, the phase difference between the NLST calculated and tensor validation spectra is 1.01 radians, within our $\pi/2$ goal. The frequency domain approach has phase agreement below the resolution of 0.06 radians. Some of this difference in phase performance between the two methods can likely be attributed to the extra numerical steps that occur in this approach.

We now keep the same system with a 50nm thin film, and extend the duration of the

pump to 100fs, to see how well time and hybrid method NLST continue to perform when the source is more narrow-band, and the sensitivity to carrier-envelope phase is lessened. In Figure 4.15, the reflected spectra of a 50nm gold film illuminated by a 100fs pulse centered at 1064nm is plotted, following the same layout as the previous figures. These results show some improvements over the previous test case.

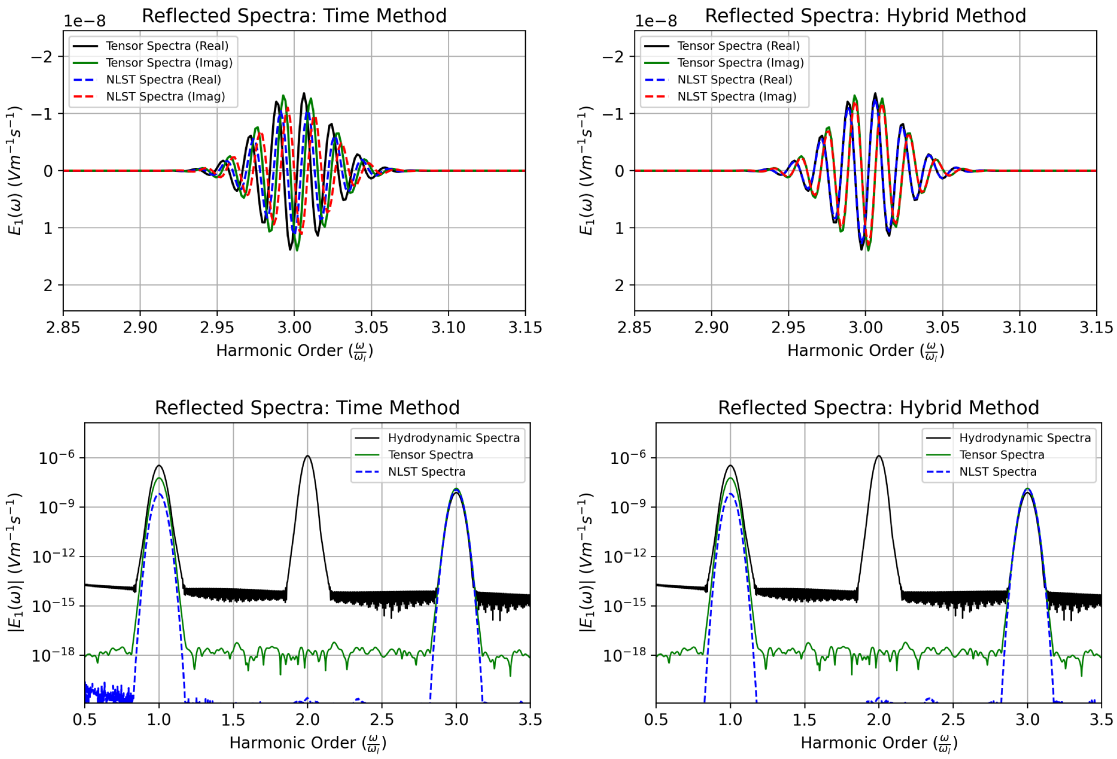

Figure 4.15: **NLST Reflected Spectra – 50nm Gold Film and 100fs Pulse**
(Left) Time and (Right) hybrid method spectra.
(Top) Tensor validation real/imaginary parts. (Bottom) Absolute fields.

The absolute detected fields in the bottom row of Figure 4.15 continue to agree fairly strongly at the third harmonic with relative differences of 18% and 7% for the time and hybrid methods, respectively, and relatively consistent with the relative deviations in the 25fs case. In this test case as well, the time-domain NLST method gives reasonable results for an estimation from only linear data, but lands outside the target 10% maximum. There are no visible differences in the peak frequencies of all three models at both the fundamental and third harmonic, lending support to the belief that the earlier shift in peak frequency was a result of the sensitivity to carrier envelope phase at the shorter pulse duration. Comparing the absolute spectra of the two approaches in this scenario reveals that the noise floor in the time domain approach is more erratic for larger wavelengths, up to two orders of magnitude

higher than that for the hybrid method, not continuing into smaller wavelengths. The source for the increased noise floor could be the extra numerical steps being performed only for this approach, such as the finite difference derivative being applied to the polarization prior to the convolution integral. Overall, the noise floor is still many orders of magnitude below those of the validation spectra, and thus is not affecting the quality of the estimated spectra.

With the prior phase results having minor variations between methods and models, we examine whether the increased pulse duration has an impact on the agreement in phase through the top two rows of Figure 4.15. The accuracy of the phase exhibits the same pattern as in the 25fs driving pulse case, with a more notable difference for the time method at 1.14 radians, and unresolvable for the hybrid method (below 0.06 radians). The final test case examines a narrow-band source on a thicker gold film.

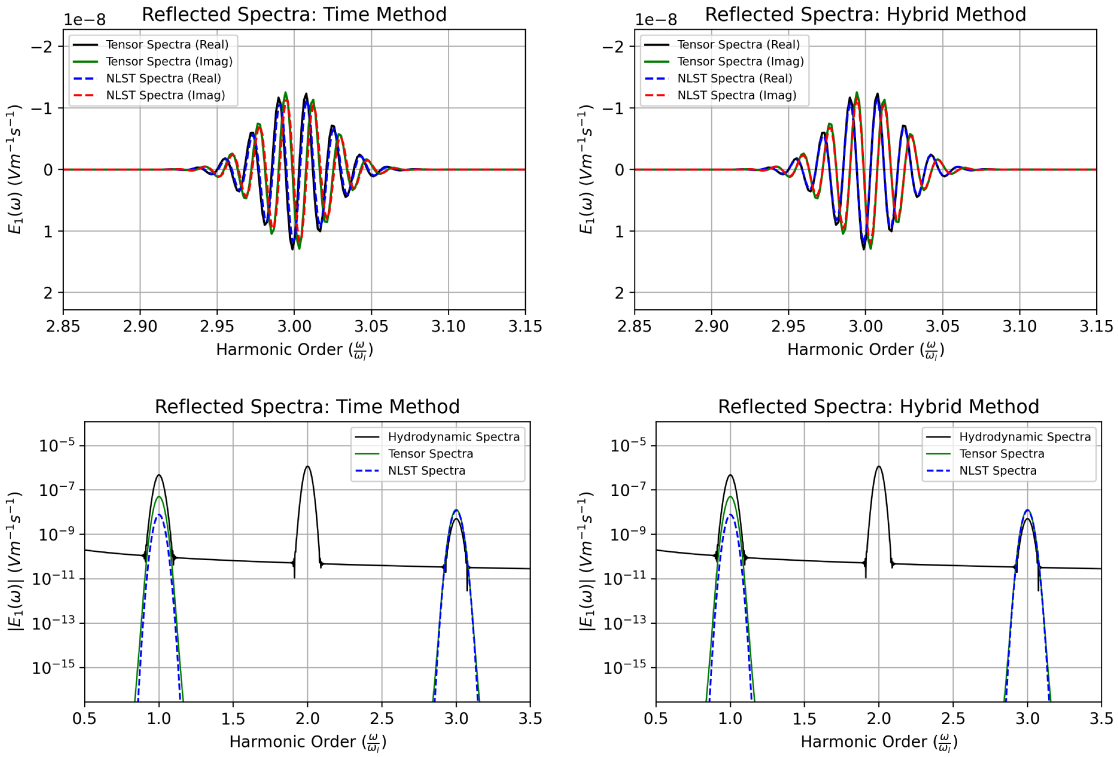

Figure 4.16: **NLST Reflected Spectra – 355nm Gold Film and 100fs Pulse**
(Left) Time and (Right) hybrid method spectra.
(Top) Tensor validation real/imaginary parts. (Bottom) Absolute fields.

The results for a thin gold film of 355nm thickness illuminated by a pump 100fs in duration are shown in Figure 4.16. The relative difference between the magnitude at the third harmonic for the tensor validation and NLST spectra is 9% and 7% for the time and hybrid methods, respectively. Most notably, however, not only does the peak value of the

time domain method improve to within the 10% goal range in this test case, but the phase for each method phase comparison agrees below the resolvable limit of the data.

In Figure 4.16, we see no notable change in the reflected spectra for frequency domain NLST and the validation constant $\chi^{(3)}$ tensor simulation when compared to the 50nm thin film illuminated by an equivalent pump in the previous test case (Figure 4.15), despite the improvements in the time-domain NLST case. Overall, the difference in the validation results is very minimal between this test case and that of the 50nm film in Figure 4.15. This makes sense, as the nonlinear generation will occur close to the surface of the film, due to the intensity of the driving signal quickly decreasing as it propagates through the film. Thus, the "extra" material beyond the surface will not contribute any notable harmonic generation in reflection, resulting in Figures 4.15 and 4.16 displaying very similar data.

4.4 3D FDTD for a Nanosphere of Gold

With many thin film cases investigated with strong results, we now examine a more complex system with a 3-dimensional gold nanosphere. In this case, we must take into account the decaying magnitude of scattered fields, adding a dependence on the distance between the detector point and the nanostructure. To scale the NLST spectra to the far field detector point, we apply Equation 3.21, developed for a sphere of uniform current and outlined in Appendix B. For these tests we will focus on a gold nanosphere of varying radii and determine whether the results continue to be successful.

A Gold Nanosphere

Using the same 3-dimensional electrodynamic solver along with the same tensor and hydrodynamic nonlinear validation models as in the previous thin film examples, we remove the periodic boundary conditions and instead use a nanosphere. The linear response of the gold continues to be a Drude with 2 Critical Points model [63], and the nonlinear instantaneous tensor $\chi^{(3)}$ is used from reference [23], with symmetry class $m3m$. The simulation parameters used for these tests are tabulated in Table 4.4. As the same preliminary nonlinear $\chi^{(3)}$ tensor model was used in this section as in Section 4.3, the same constant phase correction of π is also present in these test cases.

Parameter	Value(s)
Gold Model	Drude + 2 Critical Points
$\chi^{(3)}$ - Class $m3m$	$\chi^{(3)}_{xxxx} = 7.599 \times 10^{-19} \frac{m^2}{V^2}$
Domain Cell Size $(\Delta x, \Delta y, \Delta z)$	1nm
Simulation Time Step (Δt)	$\frac{\Delta y}{2c_0}$
Pump Wavelength	1064nm
Pump Duration (FWHM)	25fs, 100fs
Sphere Radius	25nm, 50nm

Table 4.4: **3D FDTD Simulation and Material Parameters for THG in a Gold Nanosphere**

Beginning with a broadband pulse of 25fs duration and a sphere of 25nm radius, we examine the scattered spectra in transmission at a distance of 5 microns from the surface of the gold nanosphere; the results are shown in Figure 4.17. The phase information is omitted from this figure due to both the comparison being difficult with the differing magnitude of the hydrodynamic validation data, as well as the sensitivity to carrier-envelope phase. Analysis of the phase will be performed in the following test case that uses a more narrow-band source.

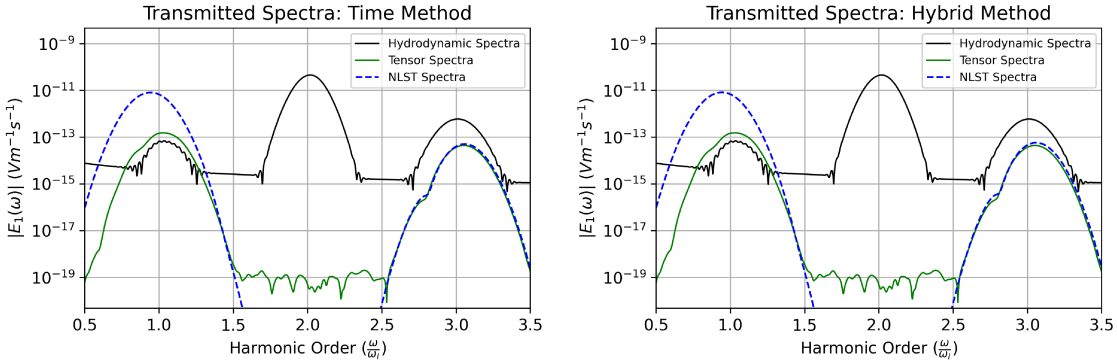

Figure 4.17: **NLST Transmitted Spectra – 25nm Radius Gold Nanosphere and 25fs Pulse**

(Left) Time method transmitted spectra. (Right) Hybrid method transmitted spectra.

Figure 4.17 shows the absolute transmitted spectra of a 25nm radius gold nanosphere illuminated by a 25fs pulse centered at 1064nm. On the left and right side of each figure, are the results of time and hybrid method NLST. The NLST results are plotted as a dashed line, with the solid lines showing the resulting spectra for two direct nonlinear simulation for validations: the hydrodynamic model (black), and instantaneous response $\chi^{(3)}$ (green).

As we compare the validation spectra in the resulting graphs, we see that the difference in the third harmonic between hydrodynamic and NLST is more prominent in this example than in many of the previous gold film test cases. Since the hydrodynamic model is used as an

indicator of how well the instantaneous response may be doing, this difference is investigated. To examine the greater difference seen in this test case, we look to a frequency domain field profiles at the third harmonic (in a plane cut through the center of the nanosphere) in Figure 4.18, alongside that for the 50nm thin film example with equivalent pump duration (corresponding to the simulations for Figure 4.14).

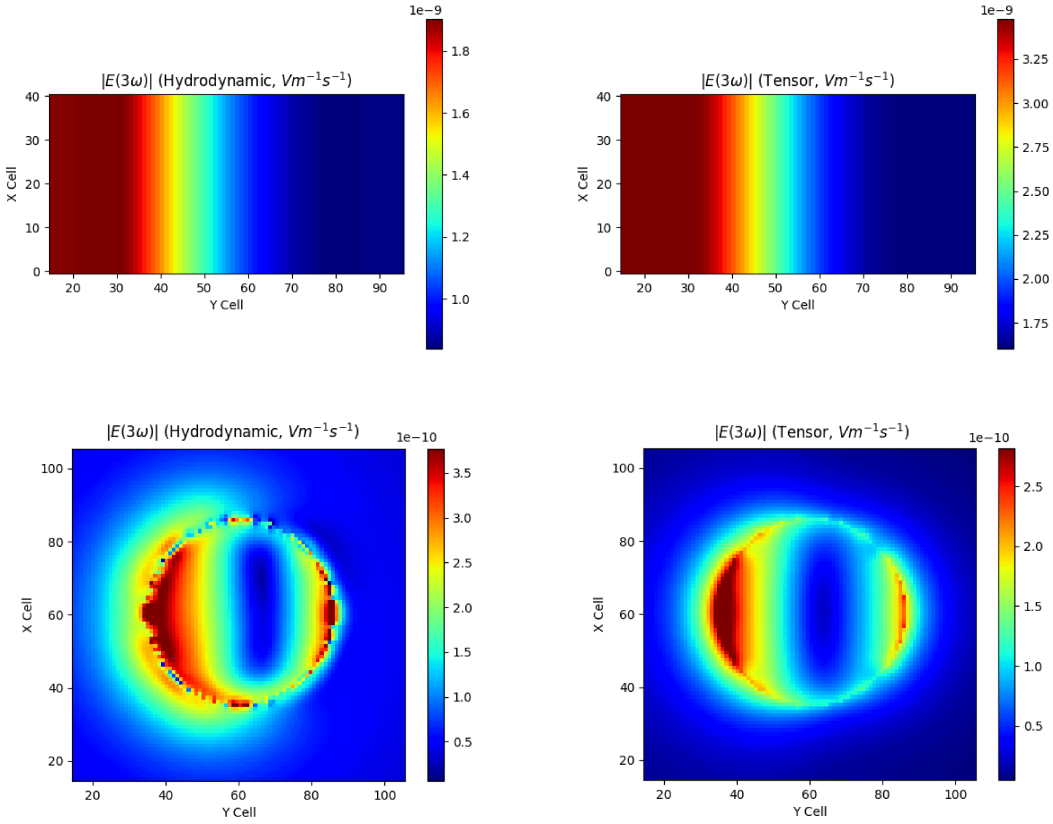

Figure 4.18: **Tensor and Hydrodynamic Third Harmonic Field Profiles for 25fs Pulse Incident Gold**

(Top) Thin film of 50nm thickness. (Bottom) Sphere of 25nm radius. (Left) Hydrodynamic Simulation. (Right) Tensor $\chi^{(3)}$ Simulation.

The field amplitude profiles at the third harmonic of four different simulations are shown in Figure 4.18, with the direction of propagation (the $+y$-direction) on the bottom axis. The two 50nm thin film cases are shown in the top row, and the two 25nm radius nanosphere cases are shown in the bottom row. Each of these are resulting from direct nonlinear simulations, where on the left-hand side the hydrodynamic model was used, and on the right-hand side the instantaneous tensor $\chi^{(3)}$ was used.

Immediately, a key difference in the thin film and nanosphere case is highlighted in Figure 4.18, which is a contributing source of the disparity. For the thin film case, which

has periodic boundary conditions and a smooth, straight edge for boundary of the nonlinear material, there is no drastic difference visible between the tensor $\chi^{(3)}$ and hydrodynamic approach. However, when a more complex geometry is introduced for the nanosphere, the hydrodynamic model's greater complexity leads to an increased sensitivity to the sharp corners that are a result of the spatial discretization of the nanosphere boundary, making it appear to be not converged with its poor symmetry and many hot-spots around the boundary. The sharp corners at the surface of the simulated sphere, seem to have a strong enhancement effect in the hydrodynamic simulation, which tends to be more sensitive due to it encapsulating more physical processes. This is resulting in greater field enhancements in and around those regions than are seen in the uniform tensor $\chi^{(3)}$ approach.

To examine whether these greater nonlinear spectra produced by the direct hydrodynamic nonlinear simulation was solely a result of the discretization, or instead something more physical, a simulation with the cell size decreased by a factor of four in each direction, resulting in a factor of 64 increase in the spatial resolution and 4x the temporal resolution, was performed. As well, it was repeated with the non-locality of the hydrodynamic model disabled to compare how these assist in the mitigation of this effect. The results can be seen in Figure 4.19.

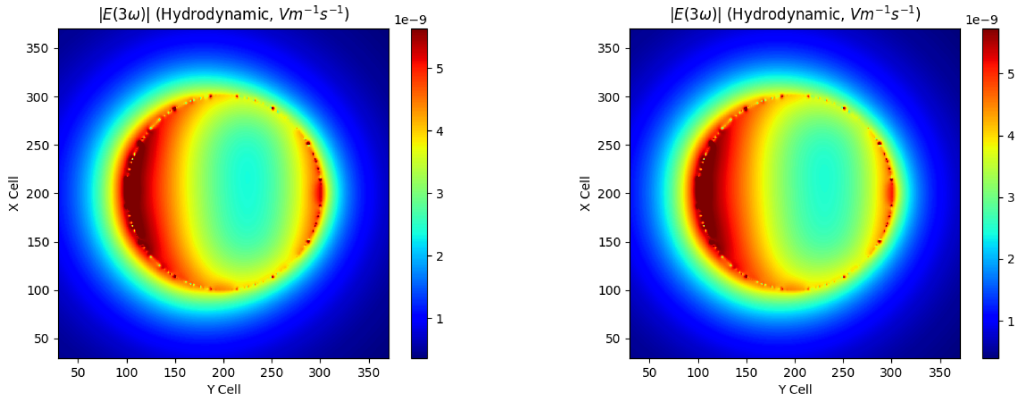

Figure 4.19: **High-Resolution Hydrodynamic Third Harmonic Field Profiles for 25fs Pulse Incident on a Gold Sphere with 25nm Radius**
(Left) Non-locality enabled. (Right) Non-locality disabled.

Figure 4.19 shows the field profile through the nanosphere center at the third harmonic from the two direct nonlinear hydrodynamic simulations of a nanosphere with 25nm radius illuminated by a 25fs pump centered at 1064nm. These nanospheres were simulated using a 0.25nm cell dimension, a factor of 4 increase in resolution for each direction. On the left and right sides of the figure, the non-local term in the hydrodynamic model has been enabled and disabled, respectively.

Immediately, the overall symmetry in Figure 4.19 is clearly much greater than that for the lower resolution hydrodynamic simulation performed for Figure 4.18, indicating that these results are more converged. This outlines that the discretization of the simulation is playing an important role in the quality of the hydrodynamic results. Interestingly, however, decreasing the cell size did not cause better agreement between the hydrodynamic and tensor nonlinear simulation results, despite the field profiles appearing to be better converged than the lower resolution simulation of Figure 4.18. This ultimately suggests that the numerical method itself has not failed in this case, but rather the underlying physics behind the model; the increased magnitude is connected to the difference in the models themselves, rather than being solely that the hydrodynamic is not fully resolved in the original example used to generation Figure 4.17.

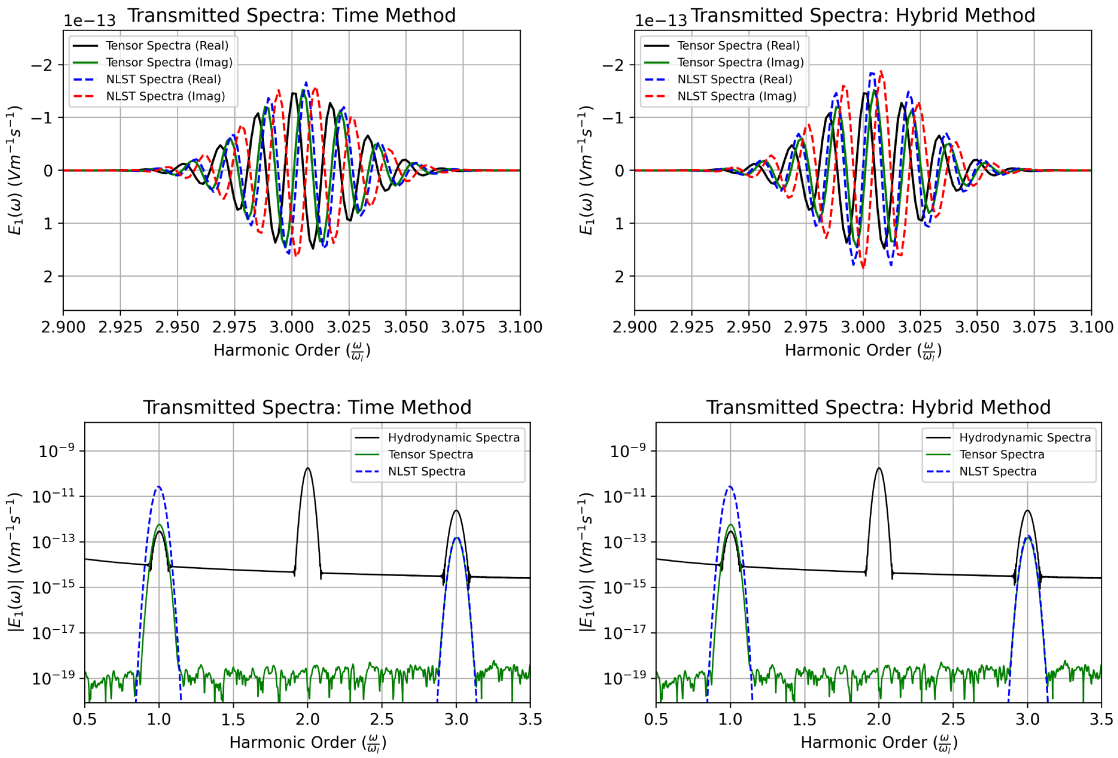

Figure 4.20: **NLST Transmitted Spectra From a 25nm Radius Gold Nanosphere Illuminated by a 100fs Pulse**

(Left) Time method transmitted spectra. (Right) Hybrid method transmitted spectra. (Top) Real/Imaginary parts with linear scaling with tensor validation. (Bottom) Absolute fields with log_{10} scaling.

Figure 4.20 shows the transmitted spectra of a 25nm radius gold nanosphere illuminated by a 100fs pulse centered at 1064nm. On the left and right side of each figure, are the results of time and hybrid method NLST. The top two rows show the real and imaginary parts of

the spectra around the third harmonic, as calculated via NLST (dashed lines) and a direct instantaneous $\chi^{(3)}$ nonlinear validation simulation (solid lines). The bottom row shows the absolute nonlinear spectra for NLST with a dashed line on a log scale, with solid lines showing the resulting spectra for two direct nonlinear simulation for validations: the hydrodynamic model (black), and instantaneous response $\chi^{(3)}$ (green).

The agreement between the NLST and tensor approaches is again very good, but there is notably less agreement between the instantaneous response $\chi^{(3)}$ and the hydrodynamic simulation. The lack of improvement in the hydrodynamic agreement is not surprising, as the geometry of the system is unchanged from the previous case with a 25fs pump duration. Comparing the NLST spectra to the tensor validation simulation, the peaks are well resolved, and align very well, with no apparent red-shifting or blue-shifting.

The real and imaginary components of the resulting spectra in the top row of Figure 4.20 compare the tensor validation simulation to the NLST estimated spectra. On the right-hand side of this figure, for the hybrid method, we see that the previously near-perfect phase agreement that was continually being achieved has diminished by a factor of just under $\pi/4$. On the left side, the time method phase is off by nearly precisely $\pi/2$, more than that for the hybrid method. This lesser agreement for the time method is consistent with that seen in the previous test cases in Section 4.3.

As the implementation of this self-consistent nonlinear simulation is still under development, it is possible that there is a different baseline phase error in the tensor method of approximately $\pi/4$, rather than the π being used. Currently, a fixed phase factor of π has been inserted, as outlined at the beginning of this chapter, as it was found to be required in many of the initial tests for this model. It is possible that with the source of this phase difference being unknown, that the state of the implementation requires a different correction under these circumstances. Overall, the consistency in phase difference between the time and hybrid methods points toward the prior attribution to the increased numerical steps in the time method being the cause of the difference between the two methods.

For the final test case, the radius of the gold sphere is increased to 50nm with the incident pulse duration decreased back to the shorter 25fs pulse, still centered at 1064nm, the results for which are pictured in Figure 4.21. The phase relationships remain the same for this test case as the previous 25nm radius nanosphere, and thus are omitted.

Figure 4.21 shows the absolute transmitted spectra of a 50nm radius gold nanosphere illuminated by a 25fs pulse centered at 1064nm. On the left and right side of each figure, are the results of time and hybrid method NLST. Calculated results are plotted as a dashed line, with the solid lines showing the resulting spectra for two direct nonlinear simulation for validations: the hydrodynamic model (black), and and instantaneous response $\chi^{(3)}$ (green).

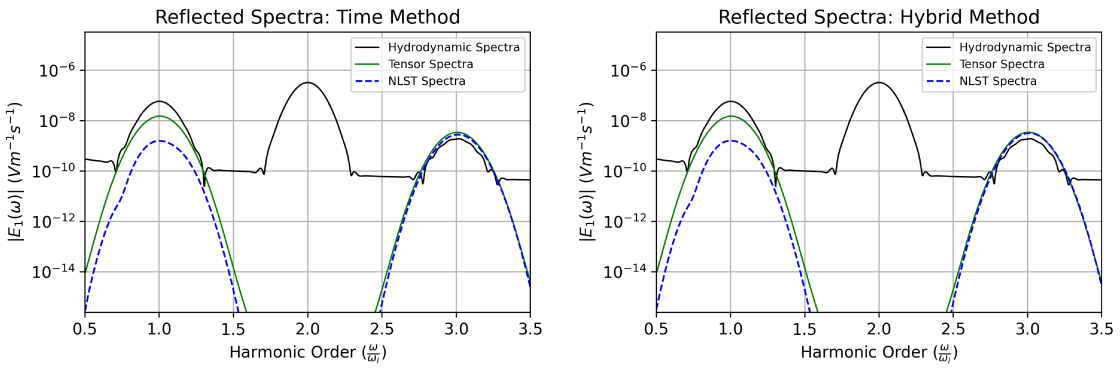

Figure 4.21: **NLST Transmitted Spectra From a 50nm Radius Gold Nanosphere Illuminated by a 25fs Pulse**

(Left) Time method transmitted spectra. (Right) Hybrid method transmitted spectra.

In Figure 4.21, not only is the strong agreement between the tensor $\chi^{(3)}$ validation simulation and NLST preserved at the third harmonic, but overall all three spectra agree remarkably well at the third harmonic, as they are each very similar in magnitude. Comparing the time and hybrid method in this figure, we see marginally better agreement between the hybrid method and the tensor $\chi^{(3)}$ spectra. To investigate the improved agreement between the two validation simulations in Figure 4.21, we again look to the corresponding field profiles at the third harmonic in Figure 4.22. On the left and right sides of the figure, the hydrodynamic model and tensor $\chi^{(3)}$ model results are shown, respectively.

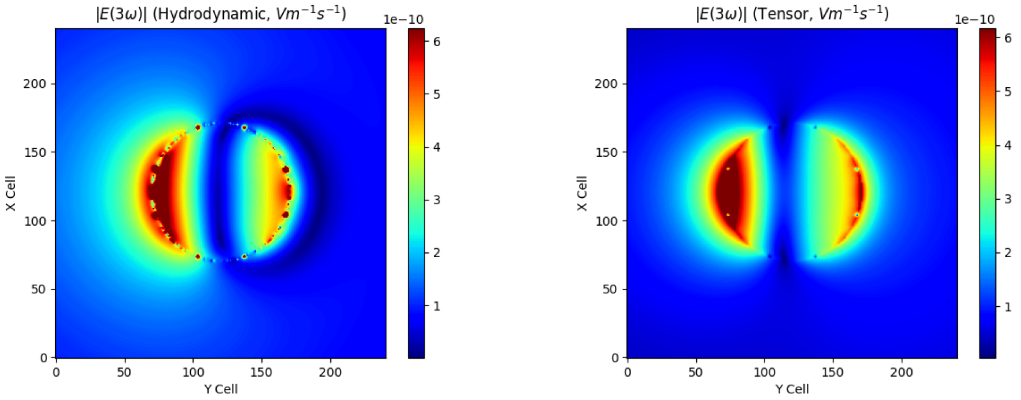

Figure 4.22: **Tensor and Hydrodynamic Third Harmonic Cross-Section for 25fs Pulse Incident Gold Nanosphere of 50nm Radius**

(Left) Hydrodynamic Simulation. (Right) Tensor $\chi^{(3)}$ Simulation.

The two cross sections shown in Figure 4.22 have several similarities and differences. Their differences, however, as exemplified by the strong results in Figure 4.21, are not sig-

nificant enough to cause notable dissimilarities in their resulting spectra. Regarding their similarities, they each exhibit very little third harmonic generation on the xz-plane running through the center region of the nanosphere (middle top to bottom in the plot). Given that the point of measurement is on the y-axis, it is possible that the relevance of the staircased "curvature" from the spatially discretized geometry is decreasing in this example.

In the 25nm radius test case of Figures 4.17 and 4.20, the nonlinear generation was notably emanating from the entire surface of the sphere (as can be seen in the bottom row of Figure 4.18). However, in the case of the 50nm radius sphere, the contribution from the top and bottom surfaces is greatly reduced. If one were to zoom vertically into the middle region of Figure 4.22 and examine only a handful of cells above and below the center y-axis, the field profile loses much of its variation in the xz-plane, and begins to appear as if it is only dependent on the y-position, a similar to trait to the thin film test cases. Thus, the effects of the curved surface are becoming less important, and the agreement begins to converge to levels seen in the thin film cases in Section 4.3, with agreements in the third harmonic being within less than an order of magnitude. Overall, the time and hybrid methods both give very strong results as they have with the previous examples, with only minor deviations between the two.

Chapter 5

Conclusions and Future Outlooks

Nonlinear scattering theory (NLST) has successfully demonstrated in this project a wide range of usability when used in the time domain, frequency domain, and a combination of the two. There existed several key goals in this project, including the development and testing of NLST in the time domain, as well performing a full comparison and contrast of the different approaches for NLST to assess the viability and use cases of each. The resulting knowledge gained through the development and testing within this thesis is to be applied in collaboration with partners at the Leibniz Universität Hannover in Germany for an upcoming manuscript on comparing quantitative methods in computational nonlinear nanophotonics. Given the successful performance of the time domain NSLT, I will also discuss future extensions of this project, in which investigations and preliminary work are already underway.

5.1 Effectiveness of the Novel Time Domain Approach

The performance of the fully time domain method was tested in a wide variety of cases in 1D and 3D using a dispersionless dielectric and a lossy metal. It proved to be quite strong as it exhibited relative deviations from direct nonlinear simulations (used as a validation) of as low as 0.1% in some cases, which is notable for a solely estimative method. Most of the tested cases fell within the goal bounds of 10% deviation in magnitude and $\pi/2$ deviation in the resulting phase. There were no scenarios found where the time method was unable to perform comparably to the frequency domain NLST approaches, when given the computational resources it required.

With more numerical steps involved, however, there were often more minor deviations from the validation simulation present in the time method than in the hybrid. As well, it was discovered in the work leading to this thesis that the time method exhibited greater sensitivity to the sampling of the simulation, for example, the time steps between frames

saved, or too-early truncation of the simulation. In the varying tests performed, there was no scenario where the effectiveness of the time method was clearly greater than that of the existing NLST in the frequency domain.

Ultimately, this approach still has great potential, as it could be possible to obtain a time domain scattered signal directly through its formulas. If a short enough impulse current is chosen, the convolution of the scattered signal with the fictitious source current could be set up in a way to obtain a scaled or averaged signal over some sub-cycle time period, yielding a result similar to a delta function. This would lead to a time domain nonlinear scattered field on the left side of Equation 2.44, meaning that the time domain signal could be estimated directly rather than through its spectra.

Though it was not achieved in the duration of this project, this capability could very well distinguish itself over the others with this aspect fully realized. It further opens doors for more time domain optimizations that could be performed on the scattered signal directly, for shaping both the incident and generated light for various features such as conversion efficiency or carrier envelope phase at the detection point.

5.2 Limitations in Nonlinear Modeling

Nonlinear scattering theory clearly demonstrated that it can only perform (at its best) as well as the nonlinear model being used to generate the results. Its performance when compared to the tensor $\chi^{(3)}$ simulation validation data remained very strong in all tests, however, when the hydrodynamic model was exhibiting different physical effects, like in the 25nm radius nanosphere case, it was clearly unable to show the same physics. This is a demonstration of this limiting factor of NLST. Outside of the undepleted pump approximation, any other additional assumptions inherent in the nonlinear model becomes automatically present in the NLST calculation. Thus, if the physics is missing from the nonlinear model being used, it remains missing in the estimated spectra.

It is important when selecting a nonlinear model for the NLST calculation that physical factors that are relevant to the system are properly present. Nonlinear scattering theory is not inherently incompatible with nonlinear models that include more complex physical processes, such as non-locality or a delayed response, it is limited only by the ability for the nonlinear parts of the response to be separable from the linear.

Ultimately, this demonstrates the need for enough nonlinear models to be available that can properly describe materials in the wavelength regimes being studied. In the case where there is no existing nonlinear model that well describes the response of a material, then NLST cannot be used effectively. This theory is solely for the purpose of estimating

what the detected nonlinear signal would be for a known nonlinear material response, and cannot be extended beyond this.

5.3 A Review of Use Cases and Viability for NLST

Each of the three approaches introduced and tested in this project have varying strengths, which make them more preferable in certain setups. There are several parameters to consider when deciding which method should be used, including source duration, source wavelength, structure size, and spatial resolution. Each of these factors affect the computational resource requirements of both the simulation, which requires monitoring, as well as the post-processing NLST calculation itself.

In the tests performed in this project, there was ready access to significant resources to perform the linear simulations and obtain the time and frequency domain datasets which were required. This is not always the case as many groups in academia and industry make use of commercial software running on machines with more limited resources, outlining that even when the test could be performed within this project, it may not be feasible for most.

Before discussing individual strengths and drawbacks of each method, there is one feature that each approach demonstrated consistently very well in most cases, which is the ability to achieve a result that is properly or reasonably in phase with the expected validation signal from a direct simulation that uses the same nonlinear model. Though there were some situations where phase differences were present, particularly for the 3-dimensional nanosphere, further improvements to the simulation method could eliminate them. Often, the phase variations presented themselves as minor, and possibly numerical in origin, meaning they could be better adjusted for with more particular setups. Thus, this far-field propagation feature is a strength for NLST as a whole.

Frequency Method

The frequency method has the advantage of a decreased dataset required to perform the necessary post-processing NLST calculation. When working with narrow-band sources, there are a limited number of relevant frequencies that require monitoring, even when the chosen material model requires a full double convolution over all frequencies. This is because the frequencies outside the bandwidth could be considered to contribute nothing to the polarization calculation saving a great deal of time and monitor data that needs to be tracked and saved.

When moving to more broadband simulations, which in this example case required the more detailed double convolution calculation, there still exists a situation in which an

argument can be made for this approach. There are certain sampling criteria required to capture a given frequency, and thus there can still be significantly less frequencies to monitor than time frames saved in the simulation in order to capture the spectra of the linear fields properly. As well, for very large structures or ones with fine spatial resolution resulting in a significant number of cells to monitor, the frequency method could still be the only viable approach due to computational resource limitations. Ultimately, this approach can have the greatest noise floor and post-processing NLST calculation run time requirements, but is notably the most memory efficient.

Hybrid Method

It was clear in this project – done with time domain simulations and a polarization model best represented in the time domain – that the hybrid method was the most reliable. Compared to the frequency method, the memory requirements of this approach are much greater as the fields need to be sampled sufficiently across the whole structure throughout the simulation. However, in the situation where the model is better represented in the time domain, the post-processing NLST calculation run time is significantly less than the frequency or time methods. For this method it is ideal to use broadband sources and smaller, coarser structures resolved with less cells to reduce the size of the dataset and simulation time required for the calculation.

Even though this method performs best in broadband simulations, with sufficient resources or a small enough structure, it remains fast and reliable for narrowband simulations as well. When the resources are available, this approach could be very strong for inverse design since the calculations can be performed quicker even in a less-optimal program such as Python, as demonstrated in the benchmarking done at the end of Section 4.1, allowing for more rapid rough results for initial optimization steps prior to fine tuning.

Time Method

The novel time domain approach performed very strongly, however did not give consistently better results when compared to both of the other methods in any of these specific test cases. The time domain Lorentz reciprocity convolution is faster than the tested double-convolution frequency domain material response calculation for broadband simulations. However, for narrowband simulations the reduced number of frequencies of interest allow the frequency domain method to overtake the time method in this aspect. Similar to the hybrid method, this approach performed consistently very well across all of the test cases, not experiencing the same numerical artifacts in the spectra at the second harmonic frequency as the frequency

method, as well as performing slightly better than the hybrid method in some of the 3-dimensional simulations.

With the development of a setup that is capable of completing the calculation in the time domain to obtain a scattered signal, this approach will establish itself as one with a much clearer use-case for time domain operations. For simulations where the goal is to obtain a scattered spectra instead, the other methods are likely more applicable and resource effective.

5.4 Future Extensions to High Harmonic Generation

Looking to harmonic generation in higher orders, the applicable nonlinear models are no longer perturbative, and become much more complex as they begin to capture subcycle dynamics of the media[59, 60]. Currently, with the strong interest in solid-state high harmonic generation (HHG) there is a broad search for structures and designs that combat the longstanding problems in efficiency, for example, see reference [42]. For this, inverse design is the most powerful method currently available to achieve the structures that exhibit the functional properties being sought after.

For simulating processes like HHG, the nonlinear models are much more complex to implement in a direct nonlinear FDTD simulation and often require an immense number of resources as the fields need to be tracked over one or more pulse cycles to capture the full dynamics picture. To alleviate the time requirement in implementing and simulating these complex models in optimization processes, NLST is a possible solution for estimative results. Some precursor work on this has been done already during this project, by investigating a macroscopic polarization model presented in 2017 by Zhokhov and Zheltikov [59].

5.4.1 Preliminary HHG Investigations

The macroscopic polarization put forward by Zhokhov and Zheltikov in 2017 has performed reasonably well in a presently implemented 1-dimensional simulation script created in the duration of this project. Using the parameters in the original publication for ZnO, my calculations showed harmonic generation up to the 33rd order (most clearly) in the scattered spectra from a thin film of 10nm when illuminated by a 15fs pulse centered at $3.2\mu m$ as shown in Figure 5.1.

This model shows promise as calculations performed show a strong resonance at a Bloch ratio (ω_B/ω_l) of approximately 3.5, which is also described in the original experimental publication demonstrating solid state high harmonics from ZnO in 2011[41]. Since the linear response is also separable from the total polarization in this model, it is seemingly compatible

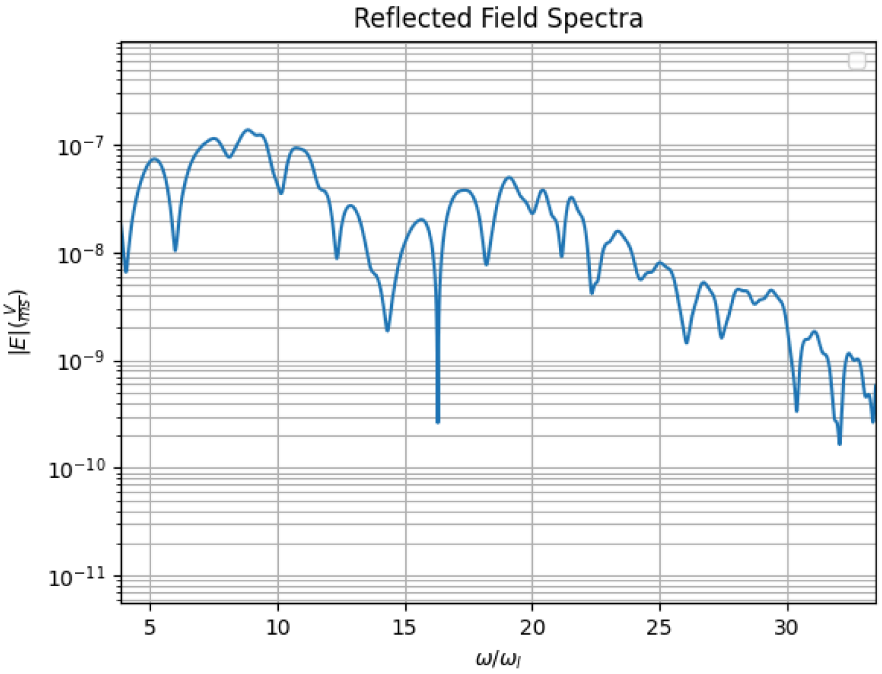

Figure 5.1: **Reflected HHG from a Thin Film of ZnO**

with nonlinear scattering theory.

Though it generates these harmonics to very high orders, the model is missing a damping factor in the time domain response function, causing the accuracy of the model to suffer, as well as increase the simulation cost as the polarization depends on all previous fields. Our research group is currently undergoing collaborative work to develop a new macroscopic polarization model that is more physically accurate and still compatible with NLST. This will also decrease the computational requirements by limiting the number of previous cycles which need to be tracked throughout the simulation.

In its current state, the complex relationship between the Bloch ratio, phase, and the output harmonics is being investigated at every step in the model to gain a physical understanding of the mechanisms.

Appendix A: Simulating Nonlinear Media Using FDTD Methods

In this section, I will outline the approach used for simulating nonlinear dielectrics and metals using Finite-Difference Time-Domain (FDTD) methods in 1D, as has been applied in the first part of this project.

A.1 Base Update Equations

Simulations using FDTD come directly from applying finite difference formulas to two of Maxwell's equations: the curl of the electric and magnetic fields,

$$\vec{\nabla} \times \vec{H} = \frac{\partial \vec{D}}{\partial t} + J_{src}, \tag{A.1}$$

and

$$\vec{\nabla} \times \vec{E} = \mu_0 \frac{\partial \vec{H}}{\partial t}. \tag{A.2}$$

This walkthrough will assume a one dimensional, linearly polarized source polarized in the $+\hat{x}$ direction, and propagating in the $+\hat{z}$ direction. It will also assume non-magnetic materials, and no free currents. Given the chosen polarization and direction of propagation for the electric fields chosen, the curl equations will be replaced with partial derivatives with respect to the Cartesian coordinate z, giving

$$-\frac{\partial H_y}{\partial z} = \frac{\partial D_x}{\partial t} + J_{src}, \tag{A.3}$$

and

$$\frac{\partial E_x}{\partial z} = -\mu_0 \frac{\partial H_y}{\partial t}. \tag{A.4}$$

We now apply finite differences to both the time and frequency partial derivatives, noting that the source will only be inserted in the source position and is thus omitted from the update for other positions. In this step, we apply the *Yee Cell* formalism, where the electric and magnetic fields are on an alternating grid in space and time, exactly one half step away from each other in each. This formalism assists in increasing the stability of the simulation by maintaining centralized derivatives and thus second order accuracy. The step in time and space will be denoted with δt and δz respectively. Equations A.3 and A.4 then become

$$-\frac{H_y\left(z+\delta z, t-\frac{\delta t}{2}\right)-H_y\left(z, t-\frac{\delta t}{2}\right)}{\delta z}=\frac{D_x\left(z+\frac{\delta z}{2}, t\right)-D_x\left(z+\frac{\delta z}{2}, t-\delta t\right)}{\delta t}, \tag{A.5}$$

$$\frac{E_x\left(z+\frac{\delta z}{2}, t\right)-E_x\left(z-\frac{\delta z}{2}, t\right)}{\delta z}=\mu_0 \frac{H_y\left(z, t+\frac{\delta t}{2}\right)-H_y\left(z, t-\frac{\delta t}{2}\right)}{\delta t}. \tag{A.6}$$

Rearranging, the FDTD update equations, including the injection of the source, are

$$D_x\left(z+\frac{\delta z}{2}, t\right)=D_x\left(z+\frac{\delta z}{2}, t-\delta t\right)-\frac{\delta t}{\delta z}\left[H_y\left(z+\delta z, t-\frac{\delta t}{2}\right)-H_y\left(z, t-\frac{\delta t}{2}\right)\right], \tag{A.7}$$

,

$$D_x\left(z_{src}, t\right)+=J_{src}\left(t\right), \tag{A.8}$$

$$H_y\left(z, t+\frac{\delta t}{2}\right)=H_y\left(z, t-\frac{\delta t}{2}\right)+\frac{\delta t}{\mu_0 \delta z}\left[E_x\left(z+\frac{\delta z}{2}, t\right)-E_x\left(z-\frac{\delta z}{2}, t\right)\right]. \tag{A.9}$$

To solve for the electric field E_x in between the update for the magnetic and displacement field, we make use of the definition of the displacement field,

$$\vec{D}=\epsilon \vec{E}=\epsilon_0 \vec{E}+\vec{P}. \tag{A.10}$$

Depending on the material, the methodology in calculating the electric field will vary. For the purposes of this project, two models were applied alongside a nonlinear instantaneous $\chi^{(3)}$. The first implemented approach was that for a dielectric with a constant linear susceptibility $\chi^{(1)}$, which was then followed by a linear susceptibility which was based off the Drude-Lorentz model.

A.2 Simulating a Dispersionless Nonlinear Material

For a dispersionless dielectric, the linear and nonlinear electric fields can be calculated exactly from the displacement field at each time step and position. As they are all at the same position and time (that is, within Yee-cell approach with leap-frogged space and time discretization), the time and space notation will be omitted to keep formulas more clear.

In our one dimensional FDTD simulation, the full nonlinear displacement field of a

dispersionless dielectric is

$$D_x = \epsilon_0 E_x + \epsilon_0 \chi^{(1)} E_x + \epsilon_0 \chi^{(3)} E_x^3. \tag{A.11}$$

In the case of a fully linear simulation, the value of $\chi^{(3)}$ can simply be set to equal 0, which will yield an easy direct calculation for the electric field that can be directly calculated prior to the update of the magnetic field:

$$E_x = \frac{1}{\epsilon_0 \left(1 + \chi^{(1)}\right)} D_x \tag{A.12}$$

For the same media with an added nonlinearity, we have a non-zero $\chi^{(3)}$. Including this in the formula, we can move all terms to one side to be left with a depressed cubic equation.

$$\epsilon_0 \chi^{(3)} E_x^3 + \epsilon_0 \left(1 + \chi^{(1)}\right) E_x - D_x = 0 \tag{A.13}$$

Cubic equations, particularly depressed cubics, are equations that have exact solutions for the roots which can often be determined using pre-optimized already-available methods in the scripting language being used. In this project, a pre-existing solver written in C was used, through Python's NumPy module[75].

Though a cubic equation could have multiple roots, under stable simulation conditions there is only one real root, and thus only one physical root for our time domain simulation. For simulation, the real root is the only root taken and used as the electric field in the update for the magnetic field.

A.3 Simulating a Dispersive Nonlinear Material

Dispersive materials require more work to simulate, both in preparation and computational resource. This is (1) due to their complex frequency domain relationships that must be translated into time domain update equations for the simulation, and (2) the need to track extra fields and perform extra calculations with their own stability requirements to take into account.

As all fields are at the same position in the simulation, the dependence on z will be excluded to keep formulas simple. Dispersive models, however, depend on values of fields at varying points in time, and thus time dependence will be explicit as necessary.

For this project, a Drude-Lorentz model was used to represent the linear dispersion of gold in the wavelength range between $600nm$ and $1800nm$. As the Drude-Lorentz model is simply a sum of each of their individual contributions, the full nonlinear displacement field is

$$D_x = \epsilon_0 E_x + P_D + P_L + \epsilon_0 \chi^{(3)} E_x^3. \tag{A.14}$$

Making use of fact that these are waves that can be tracked individually we apply the *Auxiliary Differential Equation* (ADE) method to separately track and update the Drude and Lorentz polarization densities, P_D and P_L respectively. This method allows us to translate their frequency domain formulas for the linear susceptibility into time domain relationships to determine their polarization at a given time step.

For the Drude and Lorentz models, their respective linear susceptibilities can be written in the frequency domain as

$$\chi_D^{(1)} = \frac{-\omega_{p,D}^2}{\omega^2 - 2\gamma_D i\omega}, \tag{A.15}$$

$$\chi_L^{(1)} = \frac{\omega_{p,L}^2}{\omega_{0,L}^2 - \omega^2 + 2\gamma_L i\omega}. \tag{A.16}$$

The ADE method will be demonstrated here in full for the Drude susceptibility only, as near identical steps are performed to create the time domain update for the Lorentz model. We begin by writing the Drude polarization in the frequency domain, then transforming the equation into the time domain to achieve a differential equation,

$$P_D = \epsilon_0 \frac{-\omega_{p,D}^2}{\omega^2 - 2\gamma_D i\omega} E_x, \tag{A.17}$$

$$\left((-i\omega)^2 + 2\gamma_D(-i\omega)\right) P_D = -\epsilon_0 \omega_{p,D}^2 E_x, \tag{A.18}$$

$$\frac{\partial^2 P_D}{\partial t^2} + 2\gamma_D \frac{\partial P_D}{\partial t} = -\epsilon_0 \omega_{p,D}^2 E_x. \tag{A.19}$$

We apply central differences to the last equation above, ensuring each finite difference is centered around time t, allowing us to use the electric field of the previous time step in a more numerically stable way. This gives

$$P_D\left(t + \delta t\right) = \left(\frac{2}{1 - \gamma_D \delta t}\right) P_D\left(t\right) - \left(\frac{1 + \gamma_D \delta t}{1 - \gamma_D \delta t}\right) P_D\left(t - \delta t\right) + \left(\frac{\epsilon_0 \omega_{p,D}^2 \delta t^2}{1 - \gamma_D \delta t}\right) E_x\left(t\right). \tag{A.20}$$

Going through the above steps for the Lorentz polarization term, we obtain

$$P_L\left(t+\delta t\right)=\left(\frac{2-\omega_{0,L}^2\delta t^2}{1-\gamma_L\delta t}\right)P_L\left(t\right)-\left(\frac{1+\gamma_L\delta t}{1-\gamma_L\delta t}\right)P_L\left(t-\delta t\right)+\left(\frac{\epsilon_0\omega_{p,L}^2\delta t^2}{1-\gamma_L\delta t}\right)E_x\left(t\right). \quad \text{(A.21)}$$

We thus track the Drude polarization fields and Lorentz polarization field (and as many other fields as necessary should the model be expanded) and include them in the displacement field prior to calculating the electric field at the new time step. With these two polarizations known, we again manipulate all the terms to achieve an equation which can be used to solve for the total electric field which includes the nonlinearity:

$$\epsilon_0\chi^{(3)}E_x^3+\epsilon_0E_x+\left(P_L+P_D-D_x\right)=0 \quad \text{(A.22)}$$

This equation is again a depressed cubic equation with one real root under stable conditions, and thus an exact value for the electric field is determined by solving this equation prior to the magnetic field update.

Appendix B: Far-Field Electric Field From a Sphere of Uniform Current

Consider a sphere of radius r_0, with uniform current density $\vec{J}$ pointing in the direction $\hat{u}$ which lies in the xy plane. We are interested in determining the electric field at a point $\vec{r} = r\hat{z}$, where $\vec{r} >> r_0$. To do this, we first define our current density using a Heaviside function, which limits it in space to the volume of the sphere, that is,

$$\vec{J}(\vec{r},\omega) = J_0(\omega)\, H(r_0 - |\vec{r}|)\, \hat{u}. \tag{B.1}$$

To solve for the far field electric field that arises from this define current density, we use the Helmholtz equation,

$$\nabla^2 \vec{E}(\vec{r},\omega) + k^2 \vec{E}(\vec{r},\omega) = -i\omega\mu_o \vec{J}, \tag{B.2}$$

and apply the well-known Green's function solution, given by (from reference [71])

$$G(\vec{r},\vec{\rho}) = \frac{e^{ik|\vec{r}-\vec{\rho}|}}{4\pi\,|\vec{r}-\vec{\rho}|}, \tag{B.3}$$

where the variable of integration is labeled ρ, to avoid possible confusion in prime notation.

Where the sign of the exponential is positive as we are solving for a field propagating outward from the point $\vec{r} = \vec{\rho}$. From here onward, we will choose to omit the vector notation of the fields themselves as they will all remain polarized in the $\hat{u}$ direction. The integral to then give us our electric field is

$$E(\vec{r},\omega) = -i\omega\mu_0 \int_V J(\vec{r},\omega)\, G(\vec{r},\vec{\rho})\, dV \tag{B.4}$$

$$= -i\omega\mu_0 J_0(\omega) \int_0^{2\pi}\int_0^{\pi}\int_0^{r_0} \frac{e^{ik|\vec{r}-\vec{\rho}|}}{4\pi\,|\vec{r}-\vec{\rho}|}\rho^2 sin\theta d\rho d\theta d\phi \tag{B.5}$$

First, we note the symmetry of our situation, paired with our interest in a sole point along the z-axis where θ is measured from. This tells us that each coordinate pairing of ρ and θ provides the same field contribution, independent of ϕ. Thus, this integration is fully separable, giving us:

$$E(\vec{r},\omega) = -\frac{i\omega\mu_0}{2} J_0(\omega) \int_0^{\pi}\int_0^{r_0} \frac{e^{ik|\vec{r}-\vec{\rho}|}}{|\vec{r}-\vec{\rho}|}\rho^2 sin\theta d\rho d\theta \tag{B.6}$$

Next, we expand our quantities $|\vec{r}-\vec{\rho}|$ and $\frac{1}{|\vec{r}-\vec{\rho}|}$. Applying the binomial approximation while noting that $\frac{\rho}{r} << 1$. Since we are making this approximation, we ignore contributions of the order $\left(\frac{\rho}{r}\right)^2$, giving us

$$|\vec{r}-\vec{\rho}| = \left[r^2+\rho^2-2r\rho cos\theta\right]^{\frac{1}{2}} \tag{B.7}$$

$$= r\left[1+\frac{\rho^2}{r^2}-2\frac{\rho}{r}cos\theta\right]^{\frac{1}{2}} \tag{B.8}$$

$$\approx r\left(1-\frac{\rho}{r}cos\theta\right). \tag{B.9}$$

It can be shown using very similar steps that the value $\frac{1}{|\vec{r}-\vec{\rho}|}$ can be approximated as

$$\frac{1}{|\vec{r}-\vec{\rho}|} \approx \frac{1}{r}\left(1+\frac{\rho}{r}cos\theta\right). \tag{B.10}$$

From here, we obtain

$$E\left(\vec{r},\omega\right) = -\frac{i\omega\mu_0}{2}J_0\left(\omega\right)\int_0^{\pi}\int_0^{r_0}\frac{e^{ikr-ik\rho\cos\theta}}{r}\left(1+\frac{\rho}{r}\cos\theta\right)\rho^2 sin\theta d\rho d\theta \tag{B.11}$$

$$= -\frac{i\omega\mu_0}{2}\frac{e^{ikr}}{r}J_0\left(\omega\right)\int_0^{\pi}\int_0^{r_0}e^{-ik\rho\cos\theta}\left(1+\frac{\rho}{r}\cos\theta\right)\rho^2 sin\theta d\rho d\theta \tag{B.12}$$

$$\rightarrow E\left(\vec{r},\omega\right) = \frac{2}{k^4 r}\left[\left(ik^2r_0^2+kr-3i\right)\sin\left(kr_0\right)+\left(3ikr_0-k^2r_0r\right)\cos\left(kr_o\right)\right] \tag{B.13}$$

At this step, we note that given the wavelengths of interest in the project, paired with the small cell sizes leading to a small r_0, the product $kr_0 << 1$, and thus we make use of the small angle approximations on both $\sin\left(kr_0\right)$ and $\cos\left(kr_0\right)$, defined as

$$\sin\left(kr_0\right) \approx kr_0, \tag{B.14}$$

$$\cos\left(kr_0\right) \approx 1-\frac{k^2r_0^2}{2}. \tag{B.15}$$

Using these approximations, finally obtain

$$\vec{E}\left(\vec{r},\omega\right) = -\frac{i\omega\mu_0 r_0^3}{2r}\left(1-\frac{i}{kr}\right)e^{ikr}J\left(\omega\right)\hat{u}. \tag{B.16}$$

After deciding on the spectral profile of the source, we can use this formula to determine

how the field will appear at this distance r away as it enters the simulation domain as an effective plane wave.

References

[1] D. J. BARBER and I. C. FREESTONE. An investigation of the origin of the colour of the lycurgus cup by analytical transmission electron microscopy. *Archaeometry*, 32(1):33–45, 1990.

[2] Alexander L. Davis, H. Frederik Nijhout, and Sönke Johnsen. Diverse nanostructures underlie thin ultra-black scales in butterflies. *Nature Communications*, 11(1):1294, Mar 2020.

[3] Carsten Rockstuhl, Stephen Luke, and Peter Vukusic. *Amorphous Nanophotonics in Nature*, pages 278–279. Springer.

[4] Hassan Raza. *Nanophotonics*, pages 71–72. Springer, 2019.

[5] Alexander E. Minovich, Andrey E. Miroshnichenko, Anton Y. Bykov, Tatiana V. Murzina, Dragomir N. Neshev, and Yuri S. Kivshar. Functional and nonlinear optical metasurfaces. *Laser and Photonics Reviews*, 9(2):195–213, March 2015.

[6] F. Hopkinson and David Rittenhouse. An optical problem, proposed by mr. hopkinson, and solved by mr. rittenhouse. *Transactions of the American Philosophical Society*, 2:201–206, 1786.

[7] Nikolay I. Zheludev and Yuri S. Kivshar. From metamaterials to metadevices. *Nature Materials*, 11(11):917–924, oct 2012.

[8] Nanfang Yu and Federico Capasso. Flat optics with designer metasurfaces. *Nature Materials*, 13(2):139–150, jan 2014.

[9] Patrice Genevet and Federico Capasso. Holographic optical metasurfaces: a review of current progress. *Reports on Progress in Physics*, 78(2):024401, jan 2015.

[10] Nina Meinzer, William L. Barnes, and Ian R. Hooper. Plasmonic meta-atoms and metasurfaces. *Nature Photonics*, 8(12):889–898, November 2014.

[11] C. Rockstuhl, C. Menzel, S. MÃŒhlig, J. Petschulat, C. Helgert, C. Etrich, A. Chipouline, T. Pertsch, and F. Lederer. Scattering properties of meta-atoms. *Physical Review B*, 83(24), jun 2011.

[12] D. R. Smith, Willie J. Padilla, D. C. Vier, S. C. Nemat-Nasser, and S. Schultz. Composite medium with simultaneously negative permeability and permittivity. *Physical Review Letters*, 84(18):4184–4187, may 2000.

[13] Zoran Jakšić, Slobodan Vuković, Jovan Matovic, and Dragan Tanasković. Negative refractive index metasurfaces for enhanced biosensing. *Materials*, 4(1):1–36, dec 2010.

[14] Hanzhe Liu, Cheng Guo, Giulio Vampa, Jingyuan Linda Zhang, Tomas Sarmiento, Meng Xiao, Philip H. Bucksbaum, Jelena Vuckovic, Shanhui Fan, and David A. Reis. Enhanced high-harmonic generation from an all-dielectric metasurface. *Nature Physics*, 14(10):1006–1010, aug 2018.

[15] Seyyed Ali Hassani Gangaraj and Francesco Monticone. Molding light with metasurfaces: from far-field to near-field interactions. *Nanophotonics*, 7(6):1025–1040, June 2018.

[16] Shuming Wang, Pin Chieh Wu, Vin-Cent Su, Yi-Chieh Lai, Mu-Ku Chen, Hsin Yu Kuo, Bo Han Chen, Yu Han Chen, Tzu-Ting Huang, Jung-Hsi Wang, Ray-Ming Lin, Chieh-Hsiung Kuan, Tao Li, Zhenlin Wang, Shining Zhu, and Din Ping Tsai. A broadband achromatic metalens in the visible. *Nature Nanotechnology*, 13(3):227–232, Mar 2018.

[17] Ren Jie Lin, Vin-Cent Su, Shuming Wang, Mu Ku Chen, Tsung Lin Chung, Yu Han Chen, Hsin Yu Kuo, Jia-Wern Chen, Ji Chen, Yi-Teng Huang, Jung-Hsi Wang, Cheng Hung Chu, Pin Chieh Wu, Tao Li, Zhenlin Wang, Shining Zhu, and Din Ping Tsai. Achromatic metalens array for full-colour light-field imaging. *Nature Nanotechnology*, 14(3):227–231, jan 2019.

[18] M. Khorasaninejad, W. T. Chen, J. Oh, and F. Capasso. Super-dispersive off-axis metalenses for compact high resolution spectroscopy. *Nano Letters*, 16(6):3732–3737, may 2016.

[19] Xianzhong Chen, Yan Zhang, Lingling Huang, and Shuang Zhang. Ultrathin metasurface laser beam shaper. *Advanced Optical Materials*, 2(10):978–982, 2014.

[20] Brian A. Slovick, You Zhou, Zhi Gang Yu, Ivan I. Kravchenko, Dayrl P. Briggs, Parikshit Moitra, Srini Krishnamurthy, and Jason Valentine. Metasurface polarization splitter. *Philosophical Transactions of the Royal Society A: Mathematical, Physical and Engineering Sciences*, 375(2090):20160072, 2017.

[21] Wei Ting Chen, Kuang-Yu Yang, Chih-Ming Wang, Yao-Wei Huang, Greg Sun, I-Da Chiang, Chun Yen Liao, Wei-Lun Hsu, Hao Tsun Lin, Shulin Sun, Lei Zhou, Ai Qun Liu, and Din Ping Tsai. High-efficiency broadband meta-hologram with polarization-controlled dual images. *Nano Letters*, 14(1):225–230, December 2013.

[22] Guoxing Zheng, Holger Mühlenbernd, Mitchell Kenney, Guixin Li, Thomas Zentgraf, and Shuang Zhang. Metasurface holograms reaching 80% efficiency. *Nature Nanotechnology*, 10(4):308–312, February 2015.

[23] Robert W. Boyd. *Nonlinear Optics, Third Edition*. Academic Press, Inc., USA, 3rd edition, 2008.

[24] T. H. MAIMAN. Stimulated optical radiation in ruby. *Nature*, 187(4736):493–494, August 1960.

[25] P. A. Franken, A. E. Hill, C. W. Peters, and G. Weinreich. Generation of optical harmonics. *Physical Review Letters*, 7(4):118–119, August 1961.

[26] Patrick Stoller, Peter M. Celliers, Karen M. Reiser, and Alexander M. Rubenchik. Quantitative second-harmonic generation microscopy in collagen. *Applied Optics*, 42(25):5209, sep 2003.

[27] P.J. Campagnola and C.-Y. Dong. Second harmonic generation microscopy: principles and applications to disease diagnosis. *Laser and Photonics Reviews*, 5(1):13–26, dec 2010.

[28] Francesco S Pavone and Paul J Campagnola, editors. *Second harmonic generation imaging*. Series in Cellular and Clinical Imaging. CRC Press, Boca Raton, FL, June 2013.

[29] Heiko Linnenbank, Yevgen Grynko, Jens Forstner, and Stefan Linden. Second harmonic generation spectroscopy on hybrid plasmonic/dielectric nanoantennas. *Light: Science and Applications*, 5(1):e16013–e16013, jan 2016.

[30] Ying Wang, Jun Xiao, Sui Yang, Yuan Wang, and Xiang Zhang. Second harmonic generation spectroscopy on two-dimensional materials [invited]. *Optical Materials Express*, 9(3):1136, feb 2019.

[31] Adib Keikhosravi, Jeremy S. Bredfeldt, Abdul Kader Sagar, and Kevin W. Eliceiri. Second-harmonic generation imaging of cancer. In *Methods in Cell Biology*, pages 531–546. Elsevier, 2014.

[32] N. H. Burnett, H. A. Baldis, M. C. Richardson, and G. D. Enright. Harmonic generation in co2 laser target interaction. *Applied Physics Letters*, 31(3):172–174, aug 1977.

[33] M Ferray, A L'Huillier, X F Li, L A Lompre, G Mainfray, and C Manus. Multiple-harmonic conversion of 1064 nm radiation in rare gases. *Journal of Physics B: Atomic, Molecular and Optical Physics*, 21(3):L31–L35, February 1988.

[34] R. A. Ganeev. High-order harmonic generation in laser plasma: Recent achievements. *Laser Physics*, 22(7):1177–1188, June 2012.

[35] P. B. Corkum and Ferenc Krausz. Attosecond science. *Nature Physics*, 3(6):381–387, June 2007.

[36] Francesca Calegari, Giuseppe Sansone, Salvatore Stagira, Caterina Vozzi, and Mauro Nisoli. Advances in attosecond science. *Journal of Physics B: Atomic, Molecular and Optical Physics*, 49(6):062001, February 2016.

[37] Shambhu Ghimire and David A. Reis. High-harmonic generation from solids. *Nature Physics*, 15(1):10–16, Jan 2019.

[38] J. Itatani, J. Levesque, D. Zeidler, Hiromichi Niikura, H. Pépin, J. C. Kieffer, P. B. Corkum, and D. M. Villeneuve. Tomographic imaging of molecular orbitals. *Nature*, 432(7019):867–871, dec 2004.

[39] Elmar V. van der Zwan and Manfred Lein. Molecular imaging using high-order harmonic generation and above-threshold ionization. *Physical Review Letters*, 108(4), jan 2012.

[40] K Midorikawa. Ultrafast dynamic imaging. *Nature Photonics*, 5(11):640–641, 2011.

[41] Shambhu Ghimire, Anthony D. DiChiara, Emily Sistrunk, Pierre Agostini, Louis F. DiMauro, and David A. Reis. Observation of high-order harmonic generation in a bulk crystal. *Nature Physics*, 7(2):138–141, Feb 2011.

[42] Hanzhe Liu, Giulio Vampa, Jingyuan Linda Zhang, Yu Shi, Siddharth Buddhiraju, Shanhui Fan, Jelena Vuckovic, Philip H. Bucksbaum, and David A. Reis. Beating absorption in solid-state high harmonics. *Communications Physics*, 3(1):192, Oct 2020.

[43] Antonino Cala' Lesina, Pierre Berini, and Lora Ramunno. Vectorial control of nonlinear emission via chiral butterfly nanoantennas: generation of pure high order nonlinear vortex beams. *Optics Express*, 25(3):2569, February 2017.

[44] Guixin Li, Shuang Zhang, and Thomas Zentgraf. Nonlinear photonic metasurfaces. *Nature Reviews Materials*, 2(5), March 2017.

[45] Alexander Krasnok, Mykhailo Tymchenko, and Andrea Alù. Nonlinear metasurfaces: a paradigm shift in nonlinear optics. *Materials Today*, 21(1):8–21, jan 2018.

[46] V. K. Valev, A. V. Silhanek, N. Verellen, W. Gillijns, P. Van Dorpe, O. A. Aktsipetrov, G. A. E. Vandenbosch, V. V. Moshchalkov, and T. Verbiest. Asymmetric optical second-harmonic generation from chiral g-shaped gold nanostructures. *Physical Review Letters*, 104(12), mar 2010.

[47] Pai-Yen Chen, Christos Argyropoulos, and Andrea Alù. Enhanced nonlinearities using plasmonic nanoantennas. *Nanophotonics*, 1(3-4):221–233, dec 2012.

[48] N C Panoiu, W E I Sha, D Y Lei, and G-C Li. Nonlinear optics in plasmonic nanostructures. *Journal of Optics*, 20(8):083001, June 2018.

[49] Shay Keren-Zur, Lior Michaeli, Haim Suchowski, and Tal Ellenbogen. Shaping light with nonlinear metasurfaces. *Advances in Optics and Photonics*, 10(1):309, March 2018.

[50] Shumei Chen, Guixin Li, Kok Wai Cheah, Thomas Zentgraf, and Shuang Zhang. Controlling the phase of optical nonlinearity with plasmonic metasurfaces. *Nanophotonics*, 7(6):1013–1024, June 2018.

[51] Sheng Liu, Michael B. Sinclair, Sina Saravi, Gordon A. Keeler, Yuanmu Yang, John Reno, Gregory M. Peake, Frank Setzpfandt, Isabelle Staude, Thomas Pertsch, and Igal Brener. Resonantly enhanced second-harmonic generation using III–v semiconductor all-dielectric metasurfaces. *Nano Letters*, 16(9):5426–5432, August 2016.

[52] G. Vampa, B. G. Ghamsari, S. Siadat Mousavi, T. J. Hammond, A. Olivieri, E. Lisicka-Skrek, A. Yu Naumov, D. M. Villeneuve, A. Staudte, P. Berini, and P. B. Corkum. Plasmon-enhanced high-harmonic generation from silicon. *Nature Physics*, 13(7):659–662, April 2017.

[53] Giancarlo C. Righini, Maurizio Ferrari, Antonio Cala Lesina, Pierre Berini, and Lora Ramunno. pages 111–134. Institution of Engineering and Technology, 2021.

[54] Ansys. Lumerical 3d fdtd.

[55] COMSOL AB. Comsol multiphysics.

[56] Ardavan F. Oskooi, David Roundy, Mihai Ibanescu, Peter Bermel, J.D. Joannopoulos, and Steven G. Johnson. Meep: A flexible free-software package for electromagnetic simulations by the FDTD method. *Computer Physics Communications*, 181(3):687–702, mar 2010.

[57] Sylvie Roke, Mischa Bonn, and Andrei V. Petukhov. Nonlinear optical scattering: The concept of effective susceptibility. *Physical Review B*, 70(11), sep 2004.

[58] Kevin O'Brien, Haim Suchowski, Junsuk Rho, Alessandro Salandrino, Boubacar Kante, Xiaobo Yin, and Xiang Zhang. Predicting nonlinear properties of metamaterials from the linear response. *Nature Materials*, 14(4):379–383, feb 2015.

[59] P A Zhokhov and A M Zheltikov. Depth-resolved subcycle dynamics of photoionization in solids. *Phys. Rev. A (Coll. Park.)*, 96(3), September 2017.

[60] Thomas Brabec. Private communication.

[61] P. Drude. Zur elektronentheorie der metalle. *Annalen der Physik*, 306(3):566–613, 1900.

[62] H. A. Lorentz. *The theory of electrons and its applications to the phenomena of light and Radiant Heat*. Leipzig : B.G. Teubner, 1909.

[63] P. G. Etchegoin, E. C. Le Ru, and M. Meyer. An analytic model for the optical properties of gold. *The Journal of Chemical Physics*, 125(16):164705, October 2006.

[64] Allen Taflove and Susan C. Hagness. *Computational electrodynamics: The finite-difference time-domain method*. Artech House, 2010.

[65] J.E. Houle and D.M. Sullivan. *Electromagnetic Simulation Using the FDTD Method with Python*. Wiley, 2020.

[66] Steven Johnson, Ardavan Oskooi, and Allen Taflove. *Advances in FDTD Computational Electrodynamics: Photonics and Nanotechnology*. 2013.

[67] Y R Shen. Principles of nonlinear optics. 1 1984.

[68] M. Scalora, M. A. Vincenti, D. de Ceglia, V. Roppo, M. Centini, N. Akozbek, and M. J. Bloemer. Second- and third-harmonic generation in metal-based structures. *Physical Review A*, 82(4), oct 2010.

[69] M. Saad Bin-Alam, Joshua Baxter, Kashif M. Awan, Antti Kiviniemi, Yaryna Mamchur, Antonio Calà Lesina, Kosmas L. Tsakmakidis, Mikko J. Huttunen, Lora Ramunno, and Ksenia Dolgaleva. Hyperpolarizability of plasmonic meta-atoms in metasurfaces. *Nano Letters*, 21(1):51–59, dec 2020.

[70] Joshua Baxter, Antonio Cala Lesina, and Lora Ramunno. Parallel FDTD modeling of nonlocality in plasmonics. *IEEE Transactions on Antennas and Propagation*, 69(7):3982–3994, jul 2021.

[71] L. Novotny and B. Hecht. *Principles of Nano-Optics*. Principles of Nano-optics. Cambridge University Press, 2012.

[72] James Stewart. *Calculus : early transcendentals*. Brooks/Cole, Cengage Learning, Belmont, Cal., 2012.

[73] I. H. Malitson. Interspecimen comparison of the refractive index of fused silica. *Journal of the Optical Society of America*, 55(10):1205, October 1965.

[74] Izzatjon Allayarov and Antonio Cala Lesina. Private code collaborations.

[75] Charles R. Harris, K. Jarrod Millman, Stéfan J. van der Walt, Ralf Gommers, Pauli Virtanen, David Cournapeau, Eric Wieser, Julian Taylor, Sebastian Berg, Nathaniel J. Smith, Robert Kern, Matti Picus, Stephan Hoyer, Marten H. van Kerkwijk, Matthew Brett, Allan Haldane, Jaime Fernández del Río, Mark Wiebe, Pearu Peterson, Pierre Gérard-Marchant, Kevin Sheppard, Tyler Reddy, Warren Weckesser, Hameer Abbasi, Christoph Gohlke, and Travis E. Oliphant. Array programming with NumPy. *Nature*, 585(7825):357–362, September 2020.